**Fakultät Maschinenbau**
RUHR-UNIVERSITÄT BOCHUM

RUHR
UNIVERSITÄT
BOCHUM

**RU**B

# Phase identification and micromechanical characterization of an advanced high-strength low-alloy steel

**Dissertation**

zur

Erlangung des Grades

**Doktor-Ingenieur**

der

Fakultät für Maschinenbau

der Ruhr-Universität Bochum

von

**Robin Marc Jentner**

aus Wittlich

Bochum, 2023

ERKLÄRUNG

Ich versichere an Eides statt, dass ich meine Dissertation mit dem Titel

**Phase identification and micromechanical characterization of an advanced high strength low alloy steel**

selbständig ohne unerlaubte Hilfe ausgeführt und verfasst habe und dass ich sie nicht in dieser oder in ähnlicher Form früher bei dieser oder einer anderen in- oder ausländischen Hochschule als Dissertation eingereicht habe. Die "Leitlinien guter wissenschaftlicher Praxis" der Ruhr-Universität Bochum in der neuesten Fassung habe ich eingehalten. Die zur Anfertigung der Dissertation verwendeten Quellen und Hilfsmittel habe ich vollständig angegeben. Vorveröffentlichungen von Teilen der Dissertation sind in den Quellenangaben vollständig enthalten.

Die zur Anfertigung der Dissertation verwendeten Quellen und Hilfsmittel habe ich vollständig angegeben. Veröffentlichungen von Teilen der Dissertation sind in den Quellenangaben vollständig enthalten.

Digitale Abbildungen enthalten nur die originalen Daten oder eine eindeutige Dokumentation von Art und Umfang der inhaltsverändernden Bildbearbeitung.

Eine kommerzielle Vermittlung oder Beratung wurde nicht in Anspruch genommen.

Rehlingen-Siersburg, den 17.04.2023

_____
Ort, Datum

_____
Unterschrift

ERKLÄRUNG

Ich bin darüber in Kenntnis gesetzt worden, dass meine Prüfungsarbeiten (Dissertation) zum Abschluss meines Promotionsverfahrens fünf Jahre im Dekanat dieser Fakultät aufbewahrt werden. Die Aufbewahrungsfrist beginnt jeweils nach Ablauf des Kalenderjahres, in dem die Akte geschlossen worden ist. Auf Antrag kann ich diese Arbeiten innerhalb von vier Wochen nach Ablauf der Frist im Dekanat abholen, ansonsten werden sie vernichtet.

Rehlingen-Siersburg, den 17.04.2023

_____
Ort, Datum

_____
Unterschrift

# Acknowledgements

Finally, I am deeply grateful to my parents, who made all this possible for me and always believed in me. Furthermore, this thanks also goes to my companion Jana Klein. She had enough endurance to keep our alliance upright with ups and downs throughout.

# Nomenclature

| | |
|---|---|
| **BCC** | Body centered cubic |
| **CI** | Confidence index |
| **CRSS** | Critical resolved shear stress |
| **DP** | Dual phase |
| **EBSD** | Electron backscatter diffraction |
| **ECCI** | Electron channeling contrast imaging |
| **E$_r$** | Reduced Young's modulus |
| **FIB** | Focused ion beam |
| **Ga$^+$** | Gallium ion |
| **GND** | Geometrical necessary dislocation |
| **H** | Hardness |
| **HAGB** | High angle grain boundaries |
| **HSLA** | High-strength low-alloyed |
| **IPF** | Inverse pole figure |
| **IQ** | Image quality |
| **ISE** | Indentation size effect |
| **KAM** | Kernel average misorientation |
| **LAGB** | Low angle grain boundaries |
| **LOM** | Light optical microscopy |
| **MA** | Martensite-austenite |
| **Nb** | Niobium |
| **ND** | Normal direction |
| **RD** | Rolling direction |
| **SE** | Secondary electron |
| **SEM** | Scanning electron microscopy |
| **SSE** | Sum squared error |
| **TEM** | Transmission electron microscopy |
| **Ti** | Titanium |
| **ToF-SIMS** | Time of flight secondary ion mass spectroscopy |
| **UTS** | Ultimate tensile strength |
| **V** | Vanadium |
| **YS** | Yield strength |

# Abstract

The aim of the present work was to achieve a distinct phase identification and quantification system beside characterizing the micromechanical properties of polygonal ferrite and granular bainite grains contained in a HSLA steel. The two investigated HSLA steel samples were industrially manufactured by a continuous cooling process utilizing a cooling rate below 50 K/s; the cooling rate between both samples differed by approx. 30%.

The first approach for phase identification and quantification was to test grid-nanoindentation coupled with K-means clustering analyses. However, K-means was not able to differentiate polygonal ferrite and granular bainite due to their similar mechanical properties, the impact on the measured hardness located close to grain boundaries and the granular bainite substructure size. Subsequently, an EBSD-KAM based approach was tested and validated by nanoindentation and ECCI investigations on selected grains. A 3° threshold was used to differentiate between both constituents which means that all grains containing data points above 3° were classified as granular bainite, otherwise the grain is counted as polygonal ferrite. The correlative ECCI and nanoindentation tests confirmed the classification results by using a grain tolerance angle of 5°. Moreover, it is shown that the microstructure can be subdivided into two main groups and four sub clusters. The two main groups contained polygonal ferrite and granular bainite grains, whereas the four sub categories showed an increasing nanohardness and different orientation gradients or substructure sizes. Consequently, EBSD-KAM based phase classification system was able to identify and quantify the two constituents after verifying the system with correlative measurements.

The constituents of two samples with the same chemical composition produced by the different cooling rates were micromechanically characterized by performing micropillar compression tests. Further ECCI and EBSD measurements were conducted to clarify the strengthening mechanism. It is shown that a higher cooling rate led to an increased CRSS of both constituents due to a higher dislocation density. This inhibited annihilation and cross-slip of dislocations and remained more obstacles for mobile or immobile dislocations inside the constituents. Moreover, the higher cooling rate did not influence the polygonal ferrite grain size but generated a smaller granular bainite substructure size. Since only one to three granular bainite sub-grains were included inside the pillar volume, the dislocation density significantly caused the different strength. Finally, the impact of different cooling rates on the microscopic strength was determined and the contributing strengthening mechanism were identified.

# Zusammenfassung

Im Rahmen der vorliegenden Dissertation wurde der Einfluss von zwei unterschiedlichen Abkühlraten untersucht, die zur Herstellung eines hochfesten niedriglegierten (HSLA) Stahls dienten. Hierbei lag der Fokus auf der Gefügecharakterisierung, -quantifizierung und der Ermittlung der mikromechanischen Eigenschaften von polygonalem Ferrit und granularem Bainit. Die Abkühlrate während dem kontinuierlichem Abkühlprozess in der industriellen Fertigung variierte um 30% und war in beiden Fällen unterhalb von 50 K/s.

In einem ersten Ansatz zur Phasencharakterisierung und -quantifizierung wurden über einen definierten Probenbereich rasterförmig Nanoindentationsversuche durchgeführt. Im Anschluss dienten die Härte und das reduzierte Elastizitätsmodul als Eingangsgrößen für die Datenanalyse mittels K-means. Die Korrelation der Daten mit Rückstreuelektronenbeugung (EBSD) Messungen ergab, dass K-means nicht in der Lage war, polygonalen Ferrit und granularen Bainit zu trennen. Zurückzuführen ist dies auf ähnliche mechanische Eigenschaften der beiden Phasen, sowie den Einfluss von Korngrenzen und unterschiedliche Substrukturgrößen des granularen Bainits auf die Härte und das reduzierte Elastizitätsmodul. Daraufhin wurde ein auf EBSD Messungen basierender Ansatz getestet, der auf Grundlage der kristallographischen Missorientierung einzelner Pixel zueinander die Körner den beiden Phasen zuordnet. Zur Validierung der erzielten Phasencharakterisierung dienten korrelative Untersuchungen mittels Elektronenbeugungskontrast Abbildungen und Nanoindentationsversuchen. Zur Separierung der beiden Phasen diente ein Orientierungsschwellwert von 3°. Demnach klassifizierte das automatische System Körner mit Pixelwerten größer 3° als granularen Bainit. Beinhaltete das Korninnere keine Werte, die den definierten Grenzwert überschritten, erkannte das System diese Körner als polygonalen Ferrit. Die korrelativen Untersuchungen bestätigten die Phasencharakterisierung unter Anwendung eines Korntoleranzwinkels von 5°. Darüber hinaus ergaben die Untersuchungen, dass das Gefüge in zwei Hauptgruppen und vier Untergruppen unterteilt werden kann. Die beiden Hauptgruppen gliederten sich in die beiden Phasenbestandteile polygonaler Ferrit und granularer Bainit auf. Die daraus resultierenden vier Unterkategorien wiesen eine zunehmende Nanohärte sowie unterschiedliche Orientierungsgradienten und Substrukturgrößen auf. Somit konnte anhand der korrelativen Untersuchungen gezeigt werden, dass die Separierung von polygonalem Ferrit und granularem Bainit unter Anwendung des Phasenklassifizierungssystems möglich ist.

Ein weiterer Bestandteil der Arbeit war die Bestimmung der mikromechanischen Eigenschaften unter Einflussnahme von zwei unterschiedlichen Abkühlgeschwindigkeiten. Zur Ermittlung der mikromechanischen Eigenschaften von polygonalem Ferrit und granularem Bainit dienten Mikrodruckversuche. Der Einfluss von festigkeitssteigernden Mechanismen hinsichtlich der einzelnen Gefügebestandteile wurde mit weiteren ECCI und EBSD Messungen charakterisiert und diskutiert. Es zeigt sich, dass eine höhere Abkühlungsrate aufgrund einer höheren Versetzungsdichte zu einer

erhöhten kritischen Schubspannung beider Phasenbestandteile führte. Die höhere Versetzungsdichte erzielte folglich eine höhere Anzahl an Hindernissen für das gleiten von aktivierten Versetzungen während der Verformung. Des Weiteren zeigten die Untersuchungen, dass die höhere Abkühlrate keinen Einfluss auf die Korngröße der polygonalen Ferritkörner hatte, aber eine kleinere Substruktur des granularen Bainits erzeugte. Aufgrund der Tatsache, dass nur ein bis drei Subkörner des granularen Bainits in dem getesteten Pillarvolumen enthalten waren, trug die Versetzungsdichte hauptsächlich zur Steigerung der kritischen Schubspannung bei. Es ist festzuhalten, dass die durchgeführten Untersuchungen den Einfluss der Abkühlrate auf die mikroskopische Festigkeit bestimmten sowie die festigkeitssteigernden Mechanismen identifizierten.

# Preface

The following publications are included in the present thesis:

**Publication 1:**

R.M. Jentner, K. Srivastava, S. Scholl, F.J. Gallardo-Basile, J.P. Best, C. Kirchlechner, G. Dehm, Unsupervised clustering of nanoindentation data for microstructural reconstruction: Challenges in phase discrimination, Materialia (Oxf). 28 (2023) 101750. https://doi.org/10.1016/j.mtla.2023.101750.

**Publication 2:**

R.M. Jentner, S.-P. Tsai, A. Welle, K. Srivastava, S. Scholl, J.P. Best, C. Kirchlechner, G. Dehm, Automated Classification of Granular Bainite and Polygonal Ferrite by Electron Backscatter Diffraction Verified through Local Structural and Mechanical Analyses, SSRN Electron. J. (2023). https://dx.doi.org/10.2139/ssrn.4324505.

**Publication 3:**

R.M. Jentner, S. Scholl, K. Srivastava, J.P. Best, C. Kirchlechner, G. Dehm, Local Strength of Bainitic and Ferritic HSLA Steel Constituents Understood Using Correlative Electron Microscopy and Micro-compression Testing, SSRN Electronic Journal. (2023). https://doi.org/10.2139/ssrn.4408322.


Author contribution following the CRediT system [1]:

**Publication 1:**

**R.M. Jentner:** conceptualization, methodology, validation, investigation, resources, writing – original draft, visualization, Project administration **K. Srivastava:** software, data analysis, data curation **S. Scholl:** writing – review & editing **J.P. Best:** writing – review & editing **C. Kirchlechner:** writing – review & editing, supervision, funding acquisition **G. Dehm:** writing – review & editing, supervision, funding acquisition

**Publication 2:**

**R.M. Jentner:** conceptualization, methodology, validation, investigation, resources, writing – original draft, visualization, Project administration **S.-P. Tsai:** software, data analysis, data curation **S. Scholl:** writing – review & editing **A. Welle:** investigation, writing – review & editing **K. Srivastava:** writing – review & editing **S. Scholl:** writing – review & editing **J.P. Best:** writing – review & editing **C. Kirchlechner:** writing – review & editing, supervision, funding acquisition **G. Dehm:** writing – review & editing, supervision, funding acquisition

**Publication 3:**

**R.M. Jentner:** conceptualization, methodology, validation, investigation, resources, writing – original draft, visualization, Project administration **S. Scholl:** writing – review & editing **K. Srivastava:** writing – review & editing **J.P. Best:** writing – review & editing **C. Kirchlechner:** analysis software, writing – review & editing, supervision, funding acquisition **G. Dehm:** writing – review & editing, supervision, funding acquisition

# Contents

# 1 Introduction

## 1.1 Motivation and Objectives

The progressing climate change promotes the awareness to push the expansion of renewable energy infrastructure [2]. In this context, successive weight reduction and improvement of the mechanical-technological properties of the materials used play an essential role. As a significant proportion of the steel produced worldwide consists of microalloyed or high-strength low-alloy (HSLA) steels, it is of particular importance to press ahead with further development. HSLA steels consist of different types of body centered cubic (BCC) structures deriving their mechanical-technological properties from the addition of microalloying elements (Niobium, Titanium and/or Vanadium), an accelerated cooling process and a low carbon content [3,4]. Through the accelerated cooling and the low-carbon level, a bainitic microstructure can be produced with the absence of interplate cementite precipitates resulting in an excellent combination between toughness, strength and weldability [5–8]. However, a detailed understanding how the thermomechanical manufacturing process affects the micromechanical properties of each constituent is mandatory to adjust the macroscopic behavior on the increasing requirements.

The thermomechanical processing has been continuously enhanced to manufacture low-carbon HSLA steels with versatile application possibilities [9]. As a result, bainitic microstructures are increasingly included in these products to achieve the desired mechanical-technological requirements; however, such bainitic microstructures are counted among the most complicated features produced in steels [5]. In general, bainite is a two-phase structure that transforms from the austenite phase within a temperature range between the pearlite and martensite reaction. Thus, a wide variety of different morphologies and phases between pearlite and martensite, with sizes in the range of a few nano- or micrometers can be observed. Subsequently, previous studies dedicated their work to the phase separation and quantification [5,10–14]. For instance, light optical microscopy (LOM) as well as scanning electron microscopy (SEM) [5,15–17], electron backscatter diffraction (EBSD) [18–21] or even transmission electron microscopy (TEM) [3,12,22] investigations were used to investigate the produced bainite morphologies. Thus, different occurrences of incomplete transformations were observed beside the well-known upper and lower bainite [5,23,24]. Through the addition of microalloying elements and the application of an accelerated cooling process after rolling, granular bainite and its differentiation from polygonal ferrite became more popular [3,23]. Polygonal ferrite is characterized by equiaxed grains with a low dislocation density. Granular bainite is composed of irregular ferrite (also sometimes referred as bainitic ferrite) beside carbon rich particles which are distributed between the irregular ferrite grains [5,23]. According to TEM investigations [12,25,26], irregular ferrite grains consist of ferrite sheaves which are subdivided by low angle grain boundaries (LAGB). However, both components appear almost identical under the LOM and SEM which impedes the phase separation and quantification [18].

Despite of the growing amount of using a direct cooling process after rolling to produce these complex microstructures in an energy-efficient way, a detailed understanding of the micromechanical properties of the individual phase is still missing. Therefore, it is imperative to improve phase separation and quantification techniques on industrially manufactured products as well as to link this to micromechanical characterization. This allows the strength-increasing mechanisms to be identified and assigned to the structural components.

Through technological progress, focused ion beam (FIB) microscopy facilitated the fabrication of nano- and microscale specimens to determine the mechanical properties of each constituent. The microscopic properties of the individual constituents determining the bulk behavior and will be affected by varying the chemical composition or the thermomechanical production process [27]. Micropillar compression tests are well established to describe the microscopic behavior to analyze the constituents strengthening mechanisms [28–31]. For instance, the constituents of dual phase (DP) steels, polygonal ferrite and martensite, were frequently characterized by performing pillar compression tests [32–35]. The critical resolved shear stress (CRSS) and the activated slip systems are two important values which can be obtained by micromechanical characterization. Knowledge of the mechanical properties of the individual phases helps to tailor bulk properties. Despite the wide range of applications of HSLA steels, polygonal ferrite and granular bainite have not been characterized with respect to the effect of cooling rate on their mechanical properties. Hence, FIB machined micropillar compression tests were performed on a HSLA steel which was continuously cooled by two different cooling rates during the industrial production process.

The present work performed detailed investigations to achieve a better understanding regarding polygonal ferrite and granular bainite phase identification and the impact on their mechanical properties by varying the cooling rate. Thus, the following questions were thoroughly answered for an enhanced understanding at the microscale:

- Can data driven approaches like K-Means clustering differentiate polygonal ferrite and granular bainite based on their mechanical properties obtained by nanoindentation without prior microstructure characterization? (Q1)
- Is it possible to automate the phase identification and quantification by an automated EBSD-KAM based classification system? (Q2)
- How affects the application of a different cooling rate the polygonal ferrite and granular bainite stress-strain behavior? (Q3)

## 1.2 Work procedure

In order to achieve a distinct and quantitative identification of polygonal ferrite and granular bainite, two different approaches were tested. The first approach was to perform grid-nanoindentation experiments to measure the nanohardness and reduced Young's modulus. Subsequently, an

unsupervised classification algorithm was tested whether polygonal ferrite can be separated from granular bainite by using the aforementioned parameters as input variables. Beside the HSLA steel, a DP steel sample was additionally studied as a reference sample. In order to further investigate the influence of grain boundaries on the clustering result, another sample of the HSLA steel was heat treated to consist only of polygonal ferrite grains. Several polygonal ferrite grain pairs were tested across the grain boundary and the nanoindentation data also clustered by the K-means algorithm. Since previous investigations [3,21,36,37] reported that polygonal ferrite and granular bainite contains a different orientation gradient inside the grain interior, a kernel average misorientation (KAM) threshold was defined within an automated EBSD phase separation and quantification system. The obtained results were validated by complemented electron channeling contrast imaging (ECCI) and nanoindentation investigations. Additionally, these investigations contained also time-of-flight secondary ion mass spectroscopy (ToF-SIMS) to test whether both phases are characterized by a different carbon concentration. Subsequently, micropillar compression tests were conducted on two HSLA samples which were industrial continuously cooled by using two different cooling rates. Beside the pillar compression tests, EBSD and ECCI investigations were carried out to obtain additional information regarding the phase fraction, dislocation density, substructure and grain size.

## 1.3 Structure of the thesis

The present thesis is outlined as follows: Chapter 2 gives a literature overview and background information about HSLA steels and micromechanical properties of BCC metals.

Chapter 3 contains all detailed information about the utilized sample preparation and experiments.

Chapter 4 focused on the phase separation by using grid-nanoindentation and K-means clustering to separate the constituents of the DP and HSLA steel. This work has been published by R.M. Jentner, K. Srivastava, S. Scholl, F.J. Gallardo-Basile, J.P. Best, C. Kirchlechner, G. Dehm, Unsupervised clustering of nanoindentation data for microstructural reconstruction: Challenges in phase discrimination, Materialia (Oxf). 28 (2023) 101750. https://doi.org/10.1016/j.mtla.2023.101750.

Chapter 5 is addressed to the automated polygonal ferrite and granular bainite separation by using an EBSD-KAM based threshold which was validated by complemented ECCI and nanoindentation experiments. The obtained results have been published by R.M. Jentner, S.-P. Tsai, A. Welle, K. Srivastava, S. Scholl, J.P. Best, C. Kirchlechner, G. Dehm, Automated Classification of Granular Bainite and Polygonal Ferrite by Electron Backscatter Diffraction Verified through Local Structural and Mechanical Analyses, SSRN Electron. J. (2023). https://dx.doi.org/10.2139/ssrn.4324505.

Chapter 6 presents the impact of varying the cooling rate on the micromechanical behavior as well as the phase fraction, dislocation density and grain and substructure size. Chapter 7 is submitted to R.M. Jentner, S. Scholl, K. Srivastava, J.P. Best, C. Kirchlechner, G. Dehm, Local Strength of Bainitic and

Ferritic HSLA Steel Constituents Understood Using Correlative Electron Microscopy and Micro-compression Testing, SSRN Electronic Journal. (2023). https://doi.org/10.2139/ssrn.4408322.

Lastly, Chapter 7 summarizes the achieved results and gives and gives an outlook on possible further investigations.

# 2 Literature review and fundamental background

## 2.1 HSLA steels

HSLA steel grades belong to the group of conventional steels and combine a high tensile strength and high total elongation as shown in Figure 1 [38]. Beiser [39] published first the distinct toughness increase by small additions of niobium (Nb) to a plain carbon steel. Due to the increase in welded joints and the growing demands on the mechanical-technological properties of steel structures, the carbon concentration was continuously decreased to avoid carbon or austenite precipitates and microalloying elements were added to accomplish the toughness requirements [9,40]. Thus, HSLA steels typically contain a carbon concentration less than 0.25 wt.% and additions of microalloying elements like Nb, Vanadium (V) and/or Titanium (Ti) below 0.1 wt.% as well as in total < 0.15 wt.% [40,41].
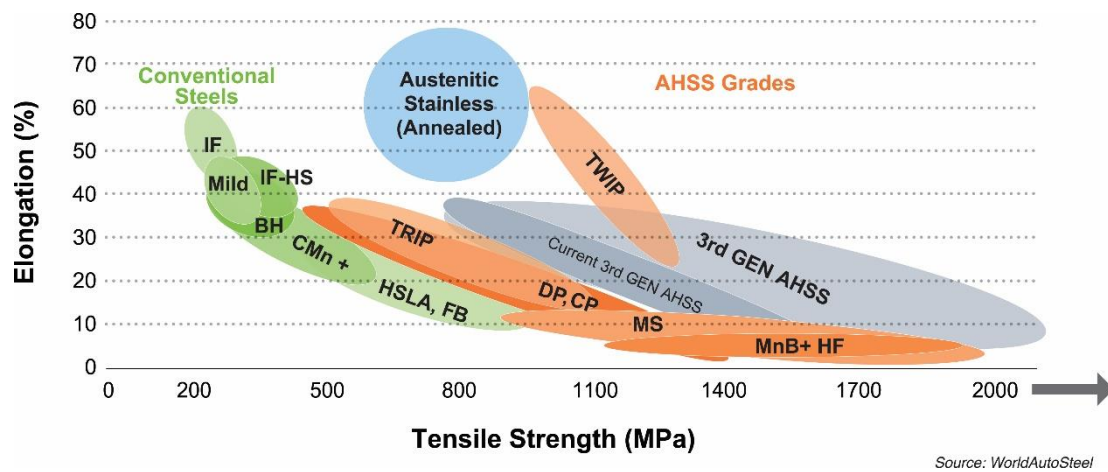


Figure 1: A comparison between currently used steel grades as a function of tensile strength vs. total elongation [38]. Mild: mild steel; BH: bake hardable; CP: complex phase; DP: dual phase; FB: Ferritic bainitic; HF: hot formed and quenched; HSLA: high-strength low-alloy; IF: interstitial free; MS: martensitic; TRIP: transformation induced plasticity; TWIP: twinning induced plasticity; AHSS: advanced high strength steels.

Through controlled rolling and a subsequent continuous cooling process, novel microstructures with a variety of complex morphologies, such as bainite, are generated [12,42]. Figure 2 schematically illustrates the production route for a controlled rolling process until the final product [4]. After the slabs have been austenitized at about 1100 – 1200 °C, the deformation process begins. Carbonitrides precipitates which are nucleated during continuous casting or strain induced precipitates inhibit the austenite grain growth at higher temperatures by the solute drag effect [43,44]. The first hot deformation steps are accompanied by a balanced process between work hardening and softening due to the recovery and recrystallization mechanism [9]. Subsequently, a refined equiaxed austenite structure will be formed which is also characterized by an increased amount of strain [43]. The final deformation step may take place before the ferrite/austenite transformation temperature is reached and, the recrystallization process cannot take place [4]. This will result in a deformed austenite structure with elongated grains along the rolling direction. It is now possible to cool the refined austenite microstructure or to proceed the deformation during ferrite formation, with the result that the final ferrite

grain size is further reduced [4]. Since the subsequent cooling process predominantly determines the austenite transformation product, the analysis of the mechanical properties of the individual constituents is of crucial importance [13].

However, the frequently used continuous cooling process leads to the formation of bainite morphologies with a wide variety which impedes a reliable phase separation and, thus the micromechanical characterization as well [5,13,24,45].
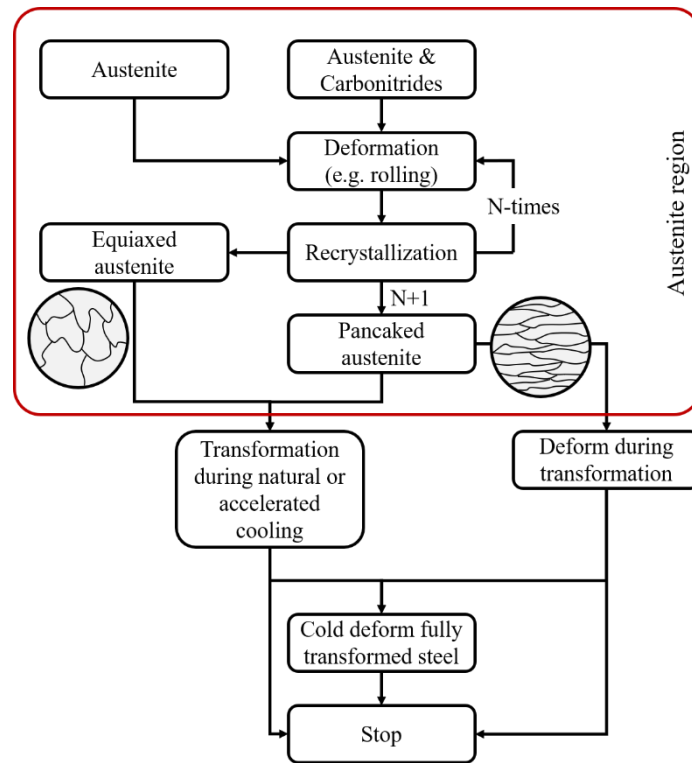


Figure 2: Schematic illustration of the possible thermomechanical production routes. The austenitized material will be mechanically deformed (e.g. rolled) and subsequently accelerated cooled down to a predefined temperature. Redrawn from [4].

### 2.1.1 HSLA steel microstructure

Industrially applied cooling rates during the continuous cooling process vary in a range where reconstructive and displacive phase transformation products can occur. Hence, constituents like polygonal ferrite, degenerated pearlite, bainite and residual martensite-austenite can be generated depending on the thermomechanical processing [5,7,46]. Specially, several complex bainite morphologies can be observed originating from the continuous cooling process. For instance, using a medium cooling rate of 5 to 60 K/s [7,45] has led to the formation of a microstructure that contains granular bainite beside polygonal ferrite. Both phases are difficult to by light optical microscopy (LOM) investigations, since both are polygonal shaped and similar in size [18,45].

During the 1950s, it was found that granular bainite consists of coarse irregular ferrite plates and islands of retained austenite and martensite after continuously cooling [12,25]. The carbon-rich retained austenite islands are partially transformed to martensite at room temperature and thus were classified

as martensite-austenite (MA) constituents representing the carbon rich second phase [19]. TEM investigations revealed that the coarse irregular ferrite grains are actually composed of ferrite sheaves, which can be separated by thin austenite or carbide films depending on the carbon concentration [23,37]. Since these steel grades typically contain a low-carbon concentration, the displacive bainite formation is predominantly associated by the absence of carbides, retained austenite or martensite layers between the ferrite substructure [45].

Figure 3 schematically illustrates the mixture of granular bainite and polygonal ferrite grains. High angle grain boundaries (HAGB) displayed as bold black lines in Figure 3 separate both constituents from each other whereas the irregular ferrite sub-grains are divided by LAGB [5,13]. The polygonal ferrite grains nucleate beside the parent austenite grain boundaries whereas the carbon-rich second phase precipitates between irregular and polygonal ferrite grains [27]. However, the parent austenite grain boundaries cannot be identified without using TEM investigations [7,45].

Since irregular ferrite sub-grains are actually sheaves in the tridimensional direction, their formation is classified as a displacive phase transformation [15,16,23,47]. The substructure formation is associated by the formation of shear stresses during continuous cooling and the subsequent relaxation of geometrical necessary dislocations (GNDs) leads to the formation of LAGB [48,49]. Carbon atoms are still able to defuse during the displacive transformation in contrast to a martensite transformation [4] and, thus the carbon rich second phase can precipitate. For instance, atom probe tomography measurements at a HSLA steel with a carbon concentration of 0.1 wt.% revealed that the irregular ferrite contained a carbon concentration of 50 to 750 ppm [22]. Consequently, carbon concentration is an important factor that significantly determines the microstructure morphology [13,27].
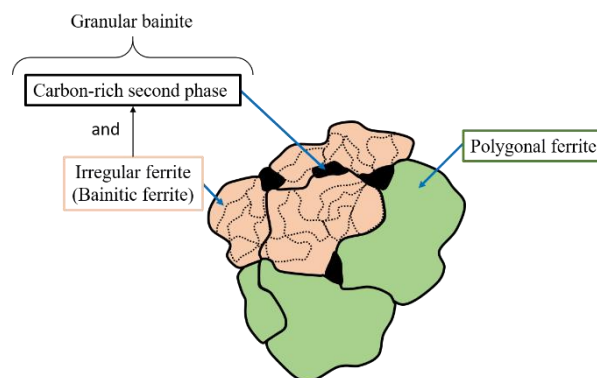


Figure 3: Schematically illustration of the complex microstructure containing granular bainite and polygonal ferrite (green) grains. Granular bainite is composed of bainitic ferrite (orange) plus a carbon rich second phase (black). High angle and low angle grain boundaries are displayed as black bold and dashed lines, respectively. The image was redrawn based on [5].

The applied cooling rate during the thermomechanical processing particularly determines the irregular ferrite substructure size. A previous investigation addressed the effects of different cooling rates on the size of the substructure and used high-resolution TEM studies for analysis [7]. It is shown by decreasing

the cooling rate from 60 to 5 K/s that the sheaf substructure disappeared and more equiaxed sub-grains were formed. The responsible mechanism for a varying substructure morphology has been described as follows [7]: after the last deformation step below the non-recrystallization temperature, the produced dislocations will pile-up and form a dislocation cell structure. These dislocation cell walls will be flattened by cross-slip of screw dislocations and climb of edge dislocations while the continuous cooling process passes through the high temperature range. Thus, the polygonization process is mainly responsible for the recovery process within the high temperature stage [50]. Subsequently, several featureless polygonal ferrite grains are formed and the undercooling of the residual austenite initiates the displacive bainite transformation. The irregular ferrite sub-grains start to nucleate at the prior austenite grain boundaries and, thus a certain coherent relationship between the parent and child phase exists [14]. Thus, the size of the substructure and the dislocation density depends significantly on the cooling rate and the associated time in the upper temperature range. However, TEM investigations on a deformed duplex stainless steel have shown that polygonal ferrite grains can be also subdivided by grain boundaries with a misorientation angle below 10° [50]. Thus, this further impedes the phase separation between bainitic ferrite and polygonal ferrite. An overview of the different characterization and classification attempts is given in the following section.

### 2.1.2    Microstructural characterization and identification

The first experiments were performed to characterize the different HSLA steel morphologies by using LOM and SEM investigations. Subsequently, EBSD and high resolution TEM experiments were performed for phase characterization regarding their orientation changes or substructure sizes. Each technique has their own benefits or limitations and, thus an overview of previous research results is provided. Initially, LOM investigations and a 2% Nital and LePera solution were used to differentiate between irregular ferrite from polygonal ferrite [14,46]. Both reported that after applying the 2% Nital solution, irregular ferrite grains exhibited a surface relief due to the displacive phase transformation, compared to polygonal ferrite grains. In addition, the LePera color etching solution colored the carbon rich second phase as white objects under the LOM. However, correlative SEM, EBSD and/or TEM investigations were later used more frequently to study the different morphologies than LOM because they offer a higher resolution.

For instance, Zajac et al. [5] used different cooling rates to simulate different bainite morphologies which were subsequently classified and quantified by SEM and associated EBSD analyses. In total, five different bainite morphologies were observed depending on the used cooling rate: granular bainite, degenerate upper bainite, upper bainite, degenerate lower bainite and lower bainite by increasing the cooling rate. Moreover, the precipitation of the carbon rich second phase was mainly influenced by the chemical composition. The associated EBSD measurements showed that granular bainite, upper and lower bainite are characterized by a different misorientation angle distribution. Upper and lower bainite showed a pronounced peak below 20° and above 50°, respectively, whereas granular bainite is

characterized by a broad misorientation angle distribution around 45°. In addition, the authors noted that the mechanical properties of the different bainite morphologies will be influenced by the amount of sub-boundaries [5].

Similar to the previous investigation, Müller et al. [51] gradually increased the cooling rate to generate samples containing a pearlite at the lowest cooling rate until full martensitic transformation. Textural information from SEM images were determined and implemented into a machine learning algorithm to distinguish the different constituents. The different morphologies were characterized with an accuracy of 91.80%. However, the large variety of different morphologies and their similarity to each other will be the main critical point to implement this technique for an industrial producer.

Beside morphological information based on SEM or LOM images, EBSD has been used to differentiate constituents according to their different orientation gradients. Phases formed by a displacive transformation are accompanied by the formation of GNDs and contain a higher orientation gradient [52,53]. Hence, constituents with a higher GND density result in pixels with a lower confidence index (CI) and image quality (IQ) [54,55]. For instance, it was shown that ferrite and martensite can be separated by using a multi-peak model of their IQ values [56]. It was required to assume that each phase has their own individual IQ distribution and the IQ peak decreases with lower transformation temperatures. Subsequently, Ryde [57] proposed the band contrast of the Kikuchi bands to differentiate bainite and ferrite. In this regard, Zaefferer et al. [52] stated that the influence of sample preparation, contamination and grain orientation will not allow an unambiguous phase differentiation. By comparing pixel- and grain-based EBSD parameters, it was concluded that only the pixel-based KAM gives a unique phase separation between bainite and ferrite [52].

EBSD measurements were also performed to study the crystallographic properties of bainite [21]. These investigations measured a higher orientation gradient inside bainite grains compared to ferrite due to plastic relaxation during the displacive phase transformation. The orientation gradient was measured by performing point-to-origin measurements inside individual grains. Subsequently, a threshold of 3° per 10 µm measurement distance was suggested to separate bainite and ferrite. Later on, further investigations confirmed this and postulated similar thresholds [3,36,37]. Most recently, the EBSD-KAM value was correlated with point-to-origin measurements to separate and quantify granular bainite and polygonal ferrite [18]. After determining the optimal kernel size for the investigated material, it was shown that the KAM classification system is consistent with the previously presented point-to-origin technique. This study [18] further concluded that tested grains exhibit an orientation gradient larger than 3° due to the defined kernel size which has to be comparable to the substructure size. Consequently, the threshold for the orientation gradient to separate the both phases was adjusted to be only 3° independent of the measurement distance.

Grid-nanoindentation tests were also conducted to achieve a unique phase separation and quantification system. Nanoindentation experiments on a ferrite-martensite DP steel showed the distinct nanohardness differences between both constituents [58–61]. In addition to DP steels, this technique has also been applied to HSLA steels, consisting of bainite and ferrite [62,63]. Both studies measured a distinct nanohardness due to the carbide or martensite-retained austenite precipitates between the bainitic ferrite subunits. Since this technique requires also the assumption that each constituent owns its individual distribution, analyzing microstructures with similar mechanical properties may limit this method. In recent years, machine learning algorithms have become increasingly relevant in big data analyses. Kumar et al. [64] used a deconvolution technique in conjunction with grid nanoindentation to enhance the phase separation of a thermal barrier coating. It is shown that the algorithm was able to deconvolute the different phases, including the smaller precipitates. All three detected phases had a unique hardness distribution which facilitates the phase identification and may blur the impact of grain or phase boundaries. An influenced hardness next to phase or grain boundaries was observed due to a higher GND density [65,66], impeded dislocation movement [67–69] or heterogeneous solute distribution [70]. Additional information related to phase characterization by using machine learning algorithms can be found elsewhere [71–73].

TEM experiments have been also applied to specially characterize the granular bainite substructure morphology [3,7,12,37,45,47]. Due to the limited sample volume and the extensive workload for sample preparation and analyses, a unique phase quantification has not been possible so far.

### 2.1.3 Strengthening mechanisms

The beneficial macroscopic HSLA steel properties arise from the combination of individual strengthening mechanisms [41]. Beside the yield strength of pure iron, four strengthening mechanism are considered to determine the toughness of HSLA steels: solid solution hardening, precipitation hardening, dislocation hardening, grain refinement (Hall-Petch) [9,41].

The purpose of **solid solution strengthening** is to inhibit the motion of mobile dislocations by pinning them to groups or individual solute atoms [74–76]. For instance, carbon and nitrogen atoms can be stored within the octahedron interstice of the ferritic crystal structure whereas larger atoms such as copper, silicon or manganese will substitute iron atoms of the BCC structure [4,77]. The generated strain field around the solute atoms leads to the interaction with dislocations and impedes their motion [78]. This was demonstrated, for example, by varying the silicon content of a high silicon steel, which resulted in a significant hardness increase of the ferritc matrix [79].

**Precipitation hardening** can be achieved by the formation of small dispersed coherent (soft) or incoherent (hard) obstacles to the activated dislocations [9,80]. It has been observed that additions of Nb, V and/or Ti form hard carbides, nitrides or carbonitrides within the HSLA steel matrix and predominantly caused dislocation bowing between the particles [9,77]. Previous investigations revealed

that precipitates in the nanometer range enhanced the strength of the bulk material depending on their volume fraction and nano-size [9,41,81,82]. In addition, the presence of precipitates retards grain growth in high temperature treatments and the recrystallization process of austenite during hot rolling [82]. Subsequently, the higher fraction of grain boundaries act as ferrite nucleation sites ensuring a finer ferrite structure after austenite has transformed to ferrite.

**Dislocation strengthening** arises from the interaction of mobile dislocation with other mobile or immobile dislocations existing in the deformed crystal [9]. The preexisting dislocations act as obstacles to moving dislocations on the activated slip planes and, thus increase the CRSS to move the dislocation through the crystal [66,81,83]. Preexisting dislocation are also described as forest dislocations. They can be generated by a deformation process or displacive phase transformation. For instance, a displacive transformation during the continuous cooling process leads to the formation of GNDs to accommodate the shape change from the parent to child phase [4]. On the other hand, a higher dislocation density will be also generated through the plastic deformation during rolling whereas dislocation recovery is inhibited [4,7]. Taylor [84] first revealed that the strength increases by the square root of the dislocation density. It has been found by correlating the yield stress with the dislocation density and lath thickness of a fully bainitic microstructure that dislocation strengthening mainly contributed to the yield stress if the lath thickness is below 1 µm [85].

The last well-known strengthening mechanism **"smaller is stronger"** is attributed to the work of Hall and Petch [86,87]. This strengthening mechanism is related to an increasing strength by reducing the effective grain size [4]. During plastic deformation, activated dislocations move towards the grain boundary on the activated slip plane. Grain boundaries acting as obstacles to the activated dislocations and, thus dislocations will pile-up at the interface [77]. Once further dislocations arrive at the grain boundary barrier, the interaction between the dislocations introduces a localized stress in the adjacent grain, which will activate a new dislocation source as soon as a critical stress was reached [4,77]. Thus, the deformation process is propagated from grain to grain and increases the required load to deform the bulk material [4]. Empirical investigations on a bainitic steel showed a relationship between the yield stress and the inverse lath size defined by a misorientation angle of $2 - 7°$ [88]. An increasing strength by reducing the bainitic substructure size was also observed by other investigations and highlights the importance to control the substructure size during thermomechanical processing [19,81,89].

A thorough understanding of the contributing strengthening mechanism is required to optimize the microstructure regarding the desired properties. However, the individual strengthening mechanism does not necessarily interact linearly and, thus the quantification of the contributing factors is challenging [9,81].

## 2.2 Micromechanical properties of BCC metals

### 2.2.1 The critical resolved shear stress and Schmid factor

The plastic deformation is associated with the motion of dislocations on activated slip planes. Dislocations are line defects and can be divided into edge, screw and mixed dislocations [90]. An edge dislocation is characterized by the Burgers vector which is normal to the dislocation line whereas the Burgers vector of screw dislocation is parallel to the dislocation line [83]. Most often, the Burgers vector varies between an angle of $> 0°$ and $< 90°$ and is thus characterized as a mixed dislocation [83,90]. While an external load is applied on a sample, the onset of plastic deformation is characterized by reaching the yield stress [91]. Subsequently, dislocations move forward if a force component acts parallel to the glide plane along the slip direction, the so-called shear stress [91]. The glide of dislocations is limited to certain surfaces which contain the dislocation line and Burgers vector [83]. These crystallographic planes are called glide planes and a consecutive motion of several dislocations on the same glide planes results in visible slip steps at the sample [83,92].

In general, slip preferentially occurs on close packed crystallographic planes and directions with the highest linear density of atoms due to the lower stress which is required to activate the atom layer [92]. Subsequently, all possible combinations of slip planes and slip directions for a certain crystallographic structure are called slip systems. The BCC structure compromises three close packed slip planes and one close packed direction. In total, 48 slip systems are possible by using all possible combinations [83,90]. The individual slip planes, slip directions and the resulting slip systems for a BCC crystal structure are listed in Table 1.

Table 1: Summary of all possible slip planes and directions within the BCC crystal structure.

| Slip planes | Slip direction | Number of slip systems |
|:---:|:---:|:---:|
| {110} | | $6 \times 2 = 12$ |
| {112} | ⟨111⟩ | $12 \times 1 = 12$ |
| {123} | | $24 \times 1 = 24$ |

Since most of the dislocations are activated on the slip plane where the highest stress is resolved, the resolved shear stress determines the plastic deformation process [91]. Schmid et al. [93] first correlated the resolved shear stress by Equation (1)

$$\tau_{RSS} = \cos(\lambda)\cos(\kappa) * \sigma = m * \sigma \qquad (1)$$

where $\kappa$ describes the angle between tensile direction and slip plane normal and $\lambda$ is the angle between tensile direction and slip direction as shown in Figure 4 [91]. Each slip system has its own characteristic Schmid factor $m$ depending on the relative orientation of the slip plane to the force direction.

Consequently, an applied force will cause dislocation motion on a slip plane where the resolved shear stress is above a critical value [83,91]. This CRSS is identical for all equivalent slip systems and depends on the tested material. Moreover, it has been shown that the CRSS is influenced by test temperature, strain rate, dislocation density and sample size [28,94,95].
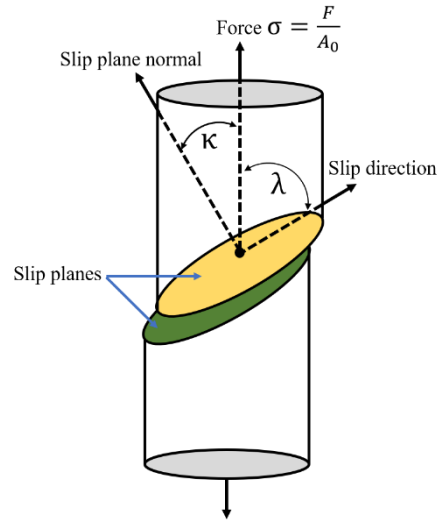


Figure 4: Schematic illustration of a deformed cylindrical sample to describe Schmid's law. The figure is redrawn from [91].

### 2.2.2 Controlled plasticity through dislocation motion

Slip in BCC crystal structures occurs along the close packed $\langle 111 \rangle$ direction along the shortest lattice vector $^a/_2 \langle 111 \rangle$ and also represents the Burgers vector of perfect slip dislocations [92,96]. The {110} slip planes contain the most widely spaced atoms compared to the {112} and {123} slip planes and, hence it is expected that the {110} slip plane will be preferentially activated during plastic deformation [90]. A three-dimensional view as well as the stacking sequence *ABABAB...* of the (110) plane along the [110] direction is schematically shown in Figure 5A and B, respectively. The atoms lying on the (110) plane are indicated as grey spheres and are displaced relative to the white spheres in the out-of-plane direction by $^a/_{\sqrt{2}}$, where $a$ represents the lattice constant [90].
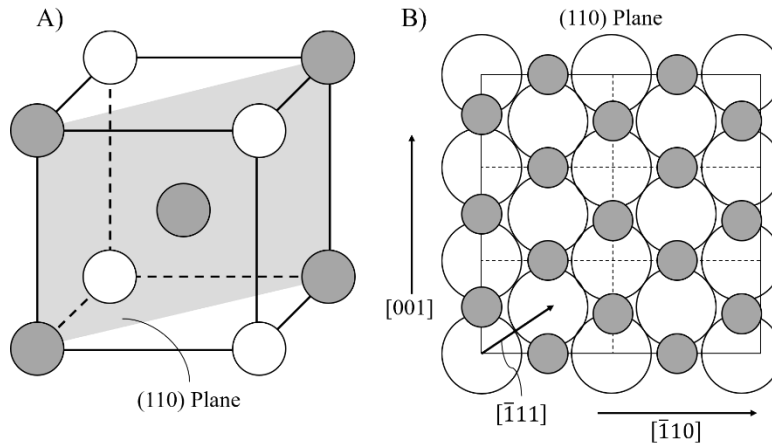
Figure 5: a) The hard sphere 3D-model illustrates the (110) plane within the BCC crystal structure. b) shows the stacking sequence *ABABAB…* of the (110) plane along the [110] direction. Redrawn from [90].

Previous TEM experiments [97–99] and computer simulations [100–102] revealed that screw dislocations primarily dominate the mechanical properties of BCC metals. Since all three slip planes contain the ⟨111⟩ slip direction and even some specific slip planes crossing along the same ⟨111⟩ direction, it is possible for screw dislocations to cross slip between different {110} planes and to activate slip on {112} and {123} planes as well [83]. This is related to the non-planar core structure of screw dislocations at higher temperatures and a three-fold symmetry along the ⟨111⟩ direction in a BCC crystal structure [83,90]. Subsequently, the core of a screw dislocation spreads into the planes of the ⟨111⟩ zone axis to reduce the elastic energy [103]. The non-planer core structure of a straight screw dislocation does not allow to move forward at finite temperatures, since it has to overcome a high energy barrier which is known as the Peierls potential [104–106]. Through the resolved shear stress and the thermal activation, screw dislocations partly bow over the Peierls barrier as shown in Figure 6 which is associated by the generation of two kink-pairs [105,106]. Once both kink-pairs exceed a critical size, the dislocation can expand into the next Peierls valley without requiring an external force [104]. The formed kink-pairs will move in the opposite direction under the action of an applied stress and, thus bring the dislocation into the adjacent Peierls valley [91].
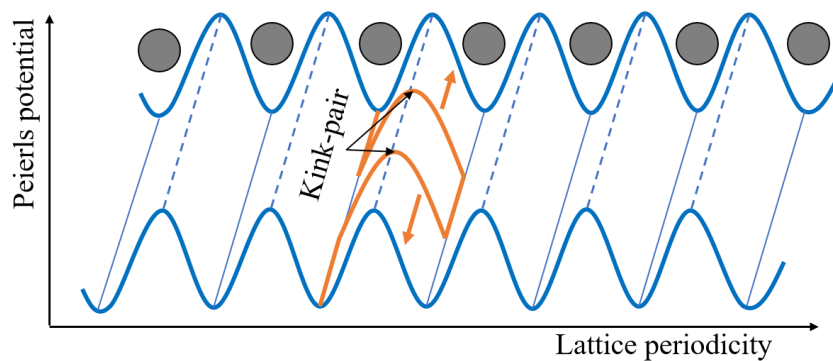


Figure 6: Illustration of the kink-pair formation mechanism by dislocation glide from one Peierls valley over the Peierls potential to the adjacent energy minimum, redrawn according to [104].

Consequently, the continuously increasing stress on a BCC metals leads to plastic deformation once the density and velocity of activated dislocations is proportional to the applied strain rate [83]. The BCC mechanical properties are directly correlated to the Peierls potential which depends on the periodic crystal lattice and the force-distance relationship between the single atoms of the slip plane [83]. Due to the significant influence of temperature on the kink-pair formation and the related mobility of screw dislocations, the BCC flow stress can be altered by varying the test temperature and strain rate [107,108].

### 2.2.3 Pillar compression tests

Pillar compression tests are an efficient method to quantify the mechanical properties at small length scales. Uchic et al. [109] started using pillar compression tests to investigate dislocation storage, multiplication, motion, pinning and nucleation during plastic deformation. Here, a FIB was used to manufacture small pillars in the range from 0.5 to 40 µm which were subsequently uniaxial compressed by a flat-punch tip. In general, the advantage of micro-pillar compression tests compared to nanoindentation is the opportunity to avoid the impact of complex stress conditions within the tested volume [31]. Previous investigations have proven that below an indentation depth of approx. 1 µm, the inhomogeneous stress conditions caused an increasing hardness by further decreasing the indentation depth [110–112]. This effect is also known as the indentation size effect (ISE).

Various processing techniques exist to separate micro-pillars from the bulk material with a round or rectangular cross-sectional area. Depending on the scientific question, in-house availability and time constraints, micro-sized sampled are frequently produced by chemical etching or FIB milling [113]. Since this work used positive charged gallium ($Ga^+$) ions as a FIB to mill round micro-pillars inside select grains, this chapter is related to the processing route of the present work. Figure 7A and B schematically shows the common annular milling procedure where the $Ga^+$ ions hitting perpendicular the polished sample surface and circles around the defined cylindrical form. This technique deflects the beam during micro-pillar processing and removes only the surrounded material [113]. Here it is advantageous that it is a fast technique to produce several micro-pillars within a short milling time which depends on the material. However, the produced pillar contains a different top and bottom diameter and, thus a taper angle between $2 – 5°$. Moreover, $Ga^+$ ions can infiltrate the micro-sample during the milling process and significantly influence the mechanical properties; specially by reducing the sample size [114]. Assuming a linear taper angle between the top and the bottom, the engineering stress value at the middle and bottom of a micro-pillar can diverge approx. 26% and 42% to the top diameter, respectively [29]. Furthermore, a pillar diameter/height ration is recommended to prevent bending during the compression test.
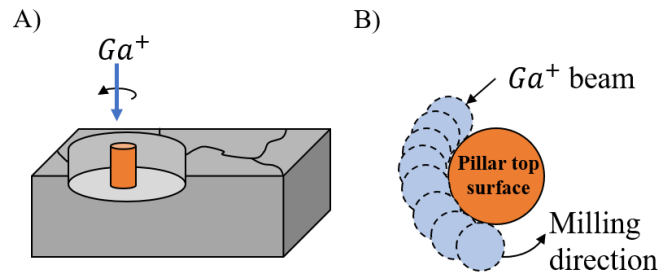
Figure 7: A) Schematic illustration of the micro-pillar preparation within a polycrystalline sample by using a focused $Ga^+$ ion beam which hits perpendicular the polished surface. B) The FIB circles around the round pillar shape to generate a free-standing sample.

Before the compression experiment can be initiated, the indenter needs to be located and aligned close over the micro-pillar surface. In total, two different approaches are known to achieve this [113]. The first approach uses the depth of field information of the SEM image; however, it is not recommended since it can change several micrometers by varying the accelerating voltage, aperture or current of the SEM. The second approach uses the secondary electron (SE) or InLense detector by shadowing the pillar top surface with the indenter. This allows an indenter and sample alignment with a distance below 100 nm. A precise alignment is essential to prevent unpredictable stress states inside the pillar volume and, thus a misinterpretation of the load and depth curve [31]. Based on the measured load and displacement, the engineering stress and strain curve is calculated by using the original height and diameter of the micro-pillar. Friction between the indenter and pillar top surface causes a multi-axial stress state as well as higher shear stresses at the upper sample area [115].

Nowadays, it is well known that micromechanical test results show a distinct increased yield strength linked with a significant variability between several samples of the same size [31,109,116]. A further detail of micromechanical experiments are displacement bursts or load drops during loading by a load or displacement-controlled experiment [31,116]. All these characteristic features were related to the limited number of dislocations within micro-sized samples [29,109,117,118]. Indeed, tensile tests revealed that dislocation-free copper whiskers reached strength values close to the theoretical strength due to a lower probability for including defects inside confined dimensions [119]. Through increasing the pillar diameter, it has been shown that the engineering stress decreases [109,118]. This phenomenon is attributed to the limited interaction of dislocations as well as geometrical constrictions of dislocation source size for smaller samples [119]. When loading small samples, dislocations will emerge and only new dislocation nucleation allows progressive plastic deformation [116]. However, samples containing a high dislocation density are characterized by a short distance between dislocations and their interactions results in an increasing work hardening [29,116]. In general, BCC metals show a weaker sample size dependence compared to face centered cubic metals which is attributed to the low mobility of screw dislocations or their pile-up behavior next to dislocation sources [120,121].

# 3 Experimental procedure

The following experimental procedure is based on previous publications[1-3].

## 3.1 Material and microstructural characterization

The present thesis investigated the effect of two different cooling rates which were used to fabricate a HSLA line pipe steel. These two samples are subsequently identified as S1 and S2 (S2 is also referred as M2 in Section 4) and had the same chemical composition as listed in Table 2. The cooling rate of was below 50 K/s for both samples, with the cooling rate of S1 being was about 30% lower than that of S2. S1 and S2 are composed of 26% / 74% and 44% / 56% polygonal ferrite and granular bainite (irregular ferrite plus a carbon rich second phase), respectively. The phase fraction of S1 and S2 was determined by EBSD measurements and is explained in detail in another study [122]. In addition, a DP steel sample was used as a reference for the nanoindentation and K-means clustering investigations; this sample is referred to as M1 and its chemical composition is listed in Table 2. M1 contained 92% of ferrite and 8% of martensite according to the LOM investigations. A third sample, from here-on be referred to as S3 (made from material S2), was heat-treated at 1150 °C for a first cycle of 72 hours and in a second cycle of 750 °C for 5 hours to produce large polygonal ferrite grains.

Table 2: Chemical composition of the dual phase steel (M1) and the HSLA steel (S1, S2/M2).

| Sample [wt.%] | C | Si | Mn | Cu | Ni | Nb+V+Ti | Fe |
|---|---|---|---|---|---|---|---|
| M1 | 0.05 | 0.17 | 1.65 | $\leq 0.5$ | $\leq 0.5$ | $\leq 0.15$ | Balance |
| S1 and S2/M2 | 0.04 | 0.32 | 1.45 | $\leq 0.5$ | $\leq 0.5$ | $\leq 0.15$ | Balance |

[1] R.M. Jentner, K. Srivastava, S. Scholl, F.J. Gallardo-Basile, J.P. Best, C. Kirchlechner, G. Dehm, Unsupervised clustering of nanoindentation data for microstructural reconstruction: Challenges in phase discrimination, Materialia (Oxf). 28 (2023) 101750. https://doi.org/10.1016/j.mtla.2023.101750.

[2] R.M. Jentner, S.-P. Tsai, A. Welle, K. Srivastava, S. Scholl, J.P. Best, C. Kirchlechner, G. Dehm, Automated Classification of Granular Bainite and Polygonal Ferrite by Electron Backscatter Diffraction Verified through Local Structural and Mechanical Analyses, SSRN Electron. J. (2023). https://doi.org/10.2139/ssrn.4324505.

[3] R.M. Jentner, S. Scholl, K. Srivastava, J.P. Best, C. Kirchlechner, G. Dehm, Local Strength of Bainitic and Ferritic HSLA Steel Constituents Understood Using Correlative Electron Microscopy and Micro-compression Testing, SSRN Electronic Journal. (2023). https://doi.org/10.2139/ssrn.4408322.

Each material was cut into pieces of $7 \times 5 \times 3$ mm, ground with SiC paper up to 2000 grit and mechanically polished by a suspension containing 30 nm alumina particles (OPA). The microstructure was revealed by using a 1% nital solution and light optical microscopy (LOM). A Zeiss Auriga® dual-beam FIB with a Ga⁺ ion source was used to mark selected areas for correlative investigations. Besides, electron channeling contrast imaging (ECCI) was conducted to reveal additional information on the HSLA steel substructure using a Zeiss Merlin® field emission microscope engaged with an acceleration voltage of 30 kV.

## 3.2 Nanoindentation

Materials were tested using a commercial nanoindentation system (Hysitron TriboIndenter 950). All nanoindentations tests were performed with a Bruker® diamond Berkovich indenter geometry with a tip radius of 200 nm. The tip area function was calibrated against a fused silica reference before testing each sample. Experiments were performed in load control, and the Oliver and Pharr method was applied to obtain the hardness $H$ and indentation modulus $E_r$ [123].

Grid-nanoindentation experiments on M1 and M2 were performed with a maximum load of 3 mN and a loading/hold/unloading time of 10/5/10s, respectively. This caused a lasting penetration depth of $115 - 198$ nm at the complex HSLA steel. Several matrices were tested on each sample with a total of approximately 1,700 indents and spacing between indents of 5 µm in both x- and y-directions. This results in a total tested area of 300x135 µm². The heat-treated sample S3 was tested at a maximum load of 0.75 mN which caused a maximum indentation depth of $70 - 100$ nm. The load was reduced to stay within the depth range for which the indenter tip was calibrated. Each grain pair was tested with nanoindentation lines oriented perpendicular to the HAGB with 5 rows and $30 - 40$ indents in total. The spacing between indents was 3 µm, and 4 µm between rows.

Additionally, individual grains of S1 were tested by utilizing nanoindentation with the same parameters as mentioned above. Here, only a maximum force of 4.5 mN was applied to capture the impact of different granular bainite substructure sizes.

## 3.3 K-means clustering of nanoindentation results

K-means is a nonhierarchical algorithm used to partition the data points into a user-defined number of clusters [124–126]. The iterative technique randomly defines the cluster centroids along the input variables and assigns the added data point to its nearest cluster centroid. After adding the next observation, the program assigns it again to the closest cluster centroid and recalculates the new cluster centroid. This also implies that the chosen number of clusters affects the clustering output [127]. The elbow method was first utilized to determine the optimal number of clusters for K-means clustering of the obtained datasets. The mechanical property parameters ($H$ and $E_r$) obtained from nanoindentation were processed to remove implausible data points before being used as input for clustering. The number

of clusters $k$ was varied between 1 to 10 and for each value the sum squared error (SSE) was calculated using the Euclidean distance as metric. As the results of K-means can depend on the initial values of the centroid, the best of five hundred different initializations was chosen. The SSE represents the sum of the average Euclidian distance of the individual datapoints from the corresponding cluster centroid. Therefore, the elbow method indicates the optimal number of clusters $k_{optimal}$ by a significant slope change measured by two different linear fits. After the inflection point, the SSE shows no significant change as the next cluster is comparable to the previous one. Following the application of the elbow method to both datasets, K-means clustering can be applied, as has been previously described [128,129].

## 3.4 Electron backscatter diffraction (EBSD) measurements

All EBSD measurements were performed along the sample transverse direction with a Zeiss Auriga dual-beam SEM. To quantify the phase fraction, two representative $80 \times 80 \, \mu m^2$ scan areas were considered at identical depth on the bulk samples' cross section. The measurements were conducted with an EDAX® Hikari detector; a step size of 50 nm and an acceleration voltage of 20 kV was chosen. The EDAX® software TSL OIM Analysis 8 and the Matlab® toolbox MTEX were utilized to analyze the exported *.ang*-files obtained from the EBSD measurement [130]. A grain dilation cleanup with a tolerance angle of 5° and a minimum grain size of 3 pixel was performed on all EBSD scans to reduce the impact of incorrectly indexed pixels; there were not more than 5% of the pixels changed.

### 3.4.1 Automated EBSD phase identification and quantification

The basis for the automated phase identification system is provided by the obtained EBSD data. The MTEX program calculates the KAM for the defined kernel size for each pixel and classifies each grain as granular bainite once the KAM is above 3°. Finally, MTEX creates a colormap of the used EBSD file and directly calculates the phase fraction. Investigations conducted to reveal a reliable automated phase classification included the following parameters:

- *Grain tolerance angle* defines the threshold until which angle neighboring pixels are grouped together to the same grain;
- *Kernel size* is calculated by the following equitation: (n-th nearest neighbor) × (step size) and takes all *n* neighbors into account;
- *KAM angle* defines the threshold until which neighbors are considered with a misorientation angle smaller than the selected *KAM angle* [130].

An orientation gradient of 3° was used as threshold to distinguish granular bainite and polygonal ferrite grains, based on Ref. [18]. Consequently, the developed program classifies grains as granular bainite once the calculated KAM of a pixel exceeds a misorientation of 3°, otherwise it will be classified as polygonal ferrite. Both constituents contain low angle grain boundaries (LAGBs) to accommodate the shape change during the controlled hot deformation process (polygonal ferrite) and the onset of displacive transformation (granular bainite) [18,50]. Thus, the *KAM angle* was set to 4.9° to reduce the

impact of low angle grain boundaries on the constituent classification. The impact of the grain tolerance angle and the kernel size was characterized by varying them in the range of 5° and 10° to distinguish sub and grain boundaries as well as using different kernel sizes ranging from 100 – 600 nm.

### 3.4.2 Point-to-origin measurements of misorientation

It has been shown by point-to-origin measurements that granular bainite and polygonal ferrite can be separated based on an in-grain misorientation angle. In case it is exceeding 3°, the constituent is classified as granular bainite. This is related to the displacive phase transformation of granular bainite [18,23]. Therefore, EBSD measurements were conducted to allocate the constituent to the selected grain before a pillar was milled by focused ion beam (FIB). The procedure which has been utilized to all tested grains is exemplarily illustrated at Grain-1 and Grain-2 in Figure 8A-C. It has been observed that the position and direction of the point-to-origin orientation measurement has an impact on the classification result and that more than one measurement is required for a unique classification [122]. Thus, three point-to-origin measurements in different directions and positions were conducted to reduce the impact of strain localizations in small grain regions (Figure 8A-B). In the case of Grain-1, all point-to-origin measurements are indicating a misorientation angle below 3°, whereas Grain-2 contains a misorientation angle above 3° (Figure 8C). Consequently, Grain-1 and Grain-2 were classified as polygonal ferrite and granular bainite, respectively. Care was taken that the misorientation gradient within each tested grain was not measured over sub-grain boundaries since it has been shown that ferrite grains in thermomechanical processed steels may be subdivided by sub-boundaries [50].
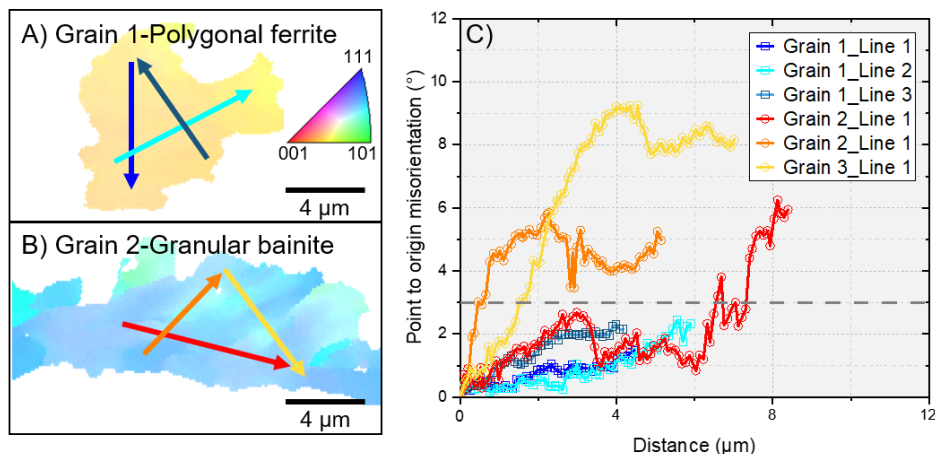


Figure 8: Grain 1 A) and grain 2 B) are two representative examples to illustrate the method how polygonal ferrite and granular bainite were distinguished. The misorientation obtained from the point-to-origin measurement within grain 1 and 2 are shown in C). Grain 1 was identified as polygonal ferrite and grain 2 as granular bainite according to the point-to-origin measurement.

## 3.5 Time of flight secondary ion mass spectroscopy (ToF-SIMS)

ToF-SIMS was performed on a TOF.SIMS5 instrument (ION-TOF GmbH, Münster, Germany) equipped with a Bi cluster primary ion source and a reflectron type time-of-flight analyzer. UHV base

pressure during analysis was $1\times10^{-10}$ mbar. Mass scale calibration was based on low molecular weight hydrocarbon signals. Before imaging the samples were cleaned in-vacuo by applying a 500 eV Cs beam up to a dose density of $6\times10^{15}$ ions/cm$^2$ under SIMS monitoring. For imaging the burst alignment mode was applied proving an un-bunched $Bi_3^+$, 25 keV, primary ion beam. In total 300 scans, cycle time 50 µs, with $512 \times 512$ pixel were recorded on a $100 \times 100$ µm$^2$ field of view showing easily the FIB markings on the sample for guidance. Due to the long recording time of 64 minutes thermal drifts in the spectrometer can cause shifts. These shifts, in the range of up to approx. 10 pixels were compensated by post-processing the data. Therefore, the strong O$^-$ images recorded were binned into pairs of two and referenced to the previous scans (ION-TOF SurfaceLab version 7.2.129059).

## 3.6 Pillar compression

### 3.6.1 Sample preparation and testing

Pillar compression tests were performed to characterize the CRSS of the activated slip system of polygonal ferrite and granular bainite grains. The retained martensite-austenite particles as well as the carbo-nitride precipitates were not tested by pillar compression experiments, since they were too small to be tested purposefully by this technique. Thus, to compare the constituent's CRSS, a constant pillar diameter of 2 µm was used for all experiments; all tested pillars had an aspect ratio (height/diameter) of 2 – 4 to prevent buckling instabilities during the experiment. The following criteria were relevant for using the selected diameter: (i) The selected diameter had to be smaller than the average grain size (S1: $(4.7 \pm 0.6)$ µm and S2: $(4.2 \pm 0.6)$ µm) to test the constituent without a grain boundary inside the pillar volume. (ii) The tested grain volume should be representative for the tested constituent and include strength determining features like the granular bainite substructure [3,88]. (iii) A pillar diameter below approx. 1 µm leads to an increased stochastic variation in yield stress which is related to the limited number and size of dislocations inside such small confined volumes ("size effect") [31,131]. The pillar manufacturing was done with a Zeiss Auriga® dual beam FIB with a $Ga^+$ ion source and a two-step milling procedure by using a current of 2nA and finally 600 pA. This procedure allowed to achieve the best milling result considering pillar-shape and milling time. The crystallographic orientation of the single crystalline polygonal ferrite and granular bainite pillar was obtained by EBSD measurements.

A Bruker Hysitron PI88 system was installed within a Zeiss Gemini 500® field emission SEM to perform the *in situ* compression tests. All pillars were compressed along the transverse direction by a diamond flat punch in a displacement-controlled mode and with a strain rate of $10^{-3}$ s$^{-1}$. The *in situ* and *post mortem* observations were done with a SE and in-Lense® detector using an acceleration voltage of 5 kV.

### 3.6.2 Pillar compression data analysis

The load and displacement data was converted to engineering stress and strain by utilizing a Mathematica® script. The calculation is based on the initial pillar height and the average pillar diameter (bottom – top pillar diameter/2). It was possible to identify the first activated slip system due to the *in situ* and *post mortem* analysis and thus to calculate the CRSS by applying $\tau_{CRSS} = m * \sigma_{2\%}$; where *m* represents the Schmid factor and $\sigma_{2\%}$ the engineering stress at an engineering strain of 2%. Using the 2% engineering strain criterion reduced the impact of dislocation-dislocation interaction occurring at higher plastic strain [132]. Once the first activated slip system was identified and its CRSS calculated, the *post mortem* images were superimposed with the four slip systems whose Schmid factor was the highest. The Mathematica® script considered all three slip plane families – {110}, {112} and {123} – and a pillar taper angle of 3°.

## 3.7 Bulk mechanical testing

The material supplier performed tensile tests for each HSLA steel at room temperature along the transverse direction. Rectangular specimens with a cross-section surface of $38.1 \times 30$ mm$^2$ and gauge length of 200 mm were tested.

# 4 Unsupervised clustering of nanoindentation data for microstructural reconstruction: Challenges in phase discrimination[1]

## 4.1 Introduction

Due to the progress and increasingly frequent use of machine learning algorithms in materials science, high-throughput methods for microstructural characterization, along with big data acquisition, are ever more relevant. For instance, nanoindentation is a commonly used technique to obtain the mechanical properties with micron-scale spatial resolution [123,133]. Grid nanoindentation extends this technique to high spatial resolution, to determine the mechanical properties of microstructural features over two-dimensions allowing for evaluation of corresponding phase fractions, as evidenced for a wide range of materials systems [134–136], where reliable hardness and indentation modulus values of individual phases can be determined. In such tests it is shown that the hardness parameter separates more clearly for each constituent phase compared to the elastic modulus, due to the larger interaction volume of the elastic zones compared to the plastic zones underneath the indents [136].

Grid nanoindentation analyzed through fitting the resulting distributions with a statistical function (e.g. Gaussian or Lorentzian) to reveal quantitative information have been performed to deconvolute the data [135,137,138]. However, the main drawback of this approach is the need to assume a certain distribution to fit the data, while eliminating a direct correlation of each classified indent with its spatial position and tested microstructure [64]. As such, K-means clustering has been successfully applied as a deconvolution technique to spatially link the obtained clustering result with the microstructural constituents, as recently demonstrated for a thermal barrier coating [64]. A similar approach has been utilized for ferrite-pearlite banded cold rolled high strength steels which were systematically annealed [139]. In this study, through microstructure correlation, clustering was able to separate the different phases and transition zones at the first annealing steps. However, with progressive annealing and the associated development of a complex recrystallized and recovered microstructure, a comparison between the clustering result and the microstructure was reported to become less clear, likely impacted by grain boundaries and various substructures which may develop during heat treatment. In both studies, the number of underlying clusters representing the microstructural constituents was decided manually.

A more frequently used methodology to determine the number of clusters in the data is the empirical elbow method [73,127,140,141]. In applying the elbow method on nanoindentation results obtained on a carbon fiber reinforced polymer, it has been shown that the optimal number of clusters could be determined by a clear inflection point [141]. However, a common feature of all represented studies is that clustering revealed a strong correlation to the actual microstructure only when the constituent phases have significant differences in strength level.

Since dual phase (DP) [66,142,143] and high-strength low-alloy (HSLA) [6,9,144] steels are used in numerous applications, such characterization and classification methods are of key interest to advance their development, e.g. by identifying single phase properties for advanced microstructural modelling. A DP steel contains a softer (ferrite) and harder (martensite) phase and nanoindentation tests reveal a clear bimodal hardness distribution representative of their individual mechanical properties [58–61]. However, it has been observed through the use of grid nanoindentation experiments that multiple indents within the same grain can yield a wide hardness distribution [60,61]. The observed continuous hardness increase from the grain interior to the grain boundary is coupled to a higher density of geometrically necessary dislocations [65,66] and hindered dislocation movement close to the grain boundary [67–69], or heterogeneous solute distributions [70]. HSLA steels have been also tested by nanoindentation to characterize the mechanical behavior of each constituent [62,63]. Both studies revealed different strength levels for selected indents placed in the center of a ferrite or bainite grain. The investigated bainite phase was subdivided by lath ferrite and cementite or martensite/retained austenite constituents which could be responsible for the clear difference in strength. However, certain HSLA steels are produced and designed to contain bainite types where the carbon rich second phase (cementite or martensite/retained austenite constituents) is eliminated or reduced in the bainitic ferrite matrix to improve the mechanical properties [3,13]. Therefore, it remains a significant challenge to distinguish between polygonal ferrite and granular bainite, as the morphology of both phases appear similar in light optical microscopy and the bainitic substructure is only separated by low angle grain boundaries whose nature varies depending on the applied cooling rate [7,18]. Due to the onset of a displacive transformation during the continuous cooling process, the granular bainite has a higher dislocation density compared to the polygonal ferrite, and it has been found that if the crystal misorientation within the selected grain exceeds 3° the grain will count as granular bainite [18]. As such, differentiation between polygonal ferrite and granular bainite has only been reasonably achieved using electron back scatter diffraction (EBSD) [3,18,21,37], although significant challenges exist in applying this technique over a large microstructural area. Unsupervised clustering of large nanoindentation data sets has enormous potential for high-throughput microstructural analysis; however, the physical limitations of such processes are not well understood.

Consequently, the present work used grid nanoindentation for phase separation on a DP and HSLA steel to point out the challenges of this technique when the phase constituents have similar mechanical

properties. Once the results were achieved by nanoindentation, the elbow method and K-means clustering were used to separate and quantify the constituents. Subsequently, each cluster was compared to EBSD measurements to identify if a clear microstructure correlation including the corresponding phase fractions was accomplished. In addition, it will be discussed how the strength of the individual phases, the impact of grain boundaries, and the substructure can affect the final clustering result. To achieve this, the HSLA steel was additionally heat-treated to produce large polygonal ferrite grains, so that the role of high angle grain boundaries (HAGBs) on the clustering can be determined.

## 4.2 Results

### 4.2.1 Nanoindentation tests and determination of the optimal cluster number

A representative area of both microstructures is illustrated by the LOM images in Figure 9A,B. Figure 9A shows that M1 consists of polygonal ferrite (bright etched grains) and martensite islands (dark etched grains). M2 is composed of polygonal ferrite and granular bainite which cannot easily be distinguished according to the LOM image (Figure 9B). The grains are in both cases elongated along the rolling direction. Figure 9C shows distinctive load and depth curves for M1 and M2 and its constituents. The curves of both samples show a typical experimental scatter which can be related to surface roughness or electronical drift [59]. From grid nanoindentation on both samples, the obtained hardness and indentation modulus values for M1 and M2 are compared as histograms in Figure 9C,D. Since material M1 consists of polygonal ferrite and martensite with distinct mechanical properties, in Figure 9C M1 shows a bimodal distribution with a dominant peak at $(2.0 \pm 0.4)$ GPa and a second shallow peak at $(4.5 \pm 0.9)$ GPa. In contrast, M2 shows a peak at $(3.1 \pm 0.4)$ GPa from fitting the hardness distribution with a Gaussian function. It can be concluded that the results of the components of M1 [59,145,146] and M2 [62,147] are consistent with previous investigations. The hardness distribution of material M2 also indicates that the hardness of both phases is almost identical, impeding separation of the Gaussian distribution of each constituent. The indentation modulus reveals for M1 and M2 a peak at $(177 \pm 28)$ GPa and $(204 \pm 23)$ GPa, respectively, when using a Gaussian distribution to describe the indentation modulus values (Figure 9D). This is consistent with previous investigations where a similar indentation modulus was determined for different body-centered cubic constituents [61,62]. A maximum indentation depth of $(193 \pm 32)$ nm was reached in case of M1, and $(189 \pm 9)$ nm in the case of M2. Further, it has been shown that for reasonable analysis of single grains the ratio between maximum indentation depth and grain size should be <0.1 to prevent an interaction of the elastic zone with the material underneath [136]. As M1 and M2 have an average grain size of $(3.0 \pm 0.3)$ µm and $(4.2 \pm 0.6)$ µm, respectively, this criterion is fulfilled and statistically representative nanoindentation data can be determined for the individual phases.
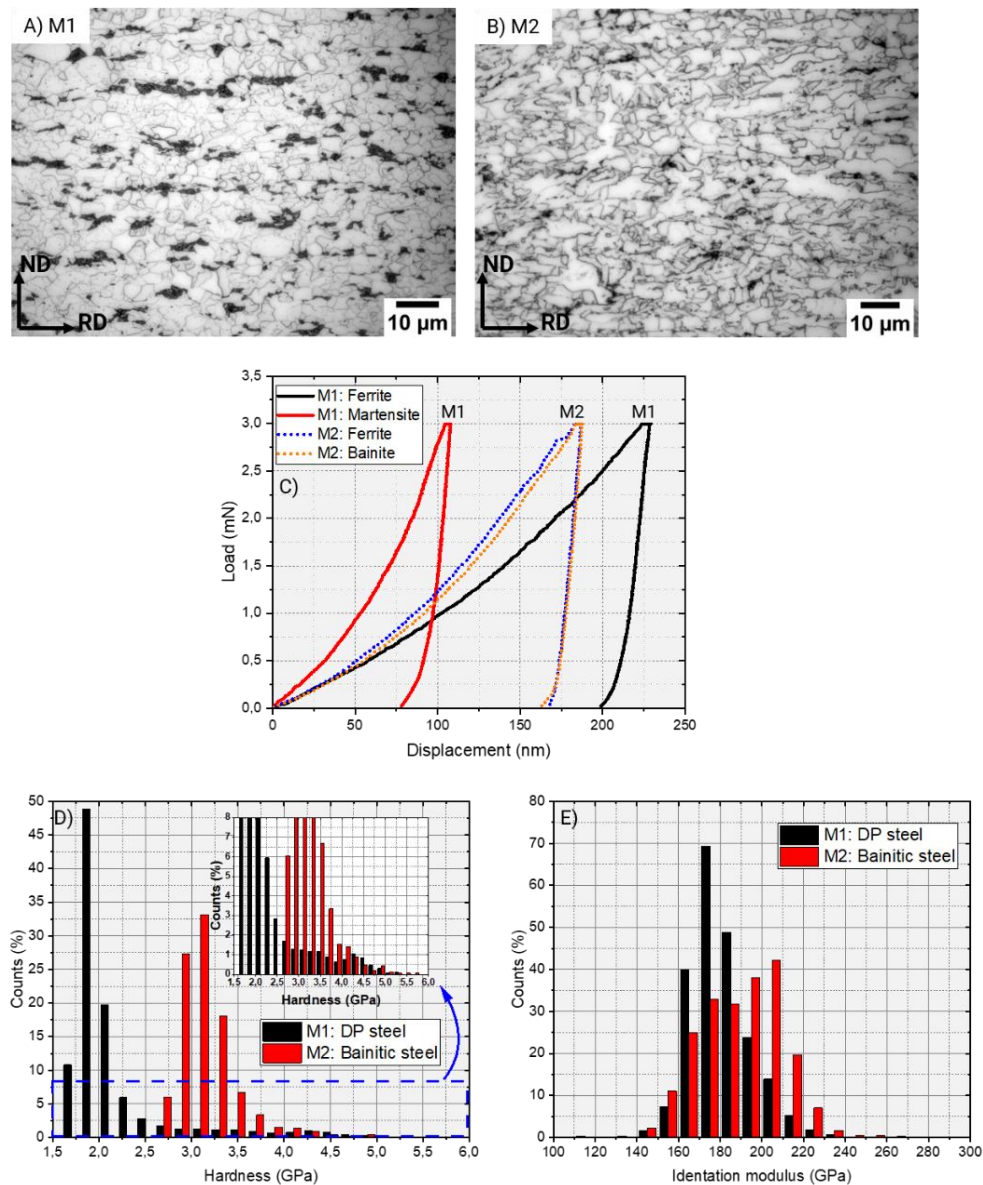
Figure 9: The LOM image shows a representative area of the A) M1 and B) M2 microstructure. C) The load and depth curve for each constituent is shown in C). The distribution shows the hardness D) and indentation modulus E) results for M1 and M2 from nanoindentation testing.

As is typical the elbow method was next applied to determine the inflection point as a good indicator of optimal number of clusters for each sample from both data sets. The calculated SSE values of both M1 and M2 were normalized and the results are shown in Figure 10. A clear inflection-point at $k_{optimal} = 3$ is indicated by the two linear fitted curves in the case of material M1. From this result, K-means clustering can be applied on M1 to identify three clusters. However, for M2 the inflection point is not as clear as for M1, rendering it necessary to vary $k$ and compare the clustering result for M2 with the microstructure to verify the optimal cluster number. Finally, the average and standard deviation for hardness and indentation modulus values of M1 are summarized in Table 3. The calculated values

of M2 are listed in Table 7 in the appendix. To obtain the average and standard deviation of both parameters, the values were separated according to its corresponding $k$-parameter and the distribution fitted by a Gaussian function. The calculated average hardness of all three clusters in the case of material M1 represents well the hardness distribution shown in Figure 9D. Thus, cluster 3 can be allocated to the dominant peak at $(2.0 \pm 0.5)$ GPa and thus to the softer ferrite phase. Furthermore, the shallow distribution for M1 is divided into two clusters, where cluster 1 captures the average hardness of the martensite phase and cluster 2 represents a transition between ferrite and martensite. This was shown to correlate directly to microstructural observations of indents locations in the DP steel (Figure 11).
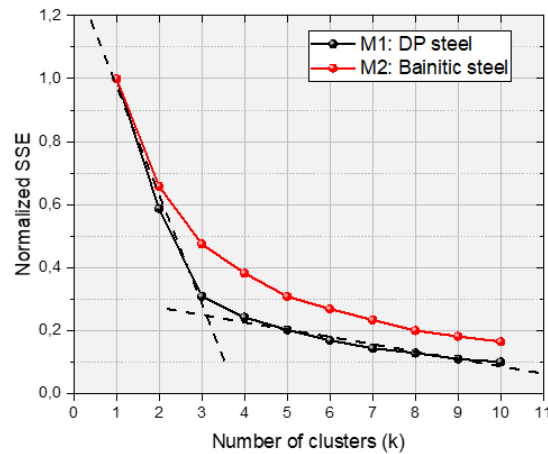


Figure 10: Determination of the optimal number of clusters by the elbow method for M1 and M2.

Table 3: Summary of the average hardness and indentation modulus, and their standard deviation, for M1 at optimal cluster number $k = 3$.

| Material | $k$ | Cluster | $H$ (GPa) | $E_r$ (GPa) | Datapoints |
|---|---|---|---|---|---|
| | | 1 | $4.0 \pm 0.6$ | $187 \pm 15$ | 127 |
| M1 | 3 | 2 | $2.2 \pm 0.3$ | $197 \pm 12$ | 651 |
| | | 3 | $2.0 \pm 0.2$ | $172 \pm 9$ | 841 |

Spatially-represented results for the two input parameters, $H$ and $E_r$, are shown in Figure 11A,B as well as the clustering result in Figure 11C for $k = 3$. The calculated cluster heatmap was directly compared to the obtained microstructural information within the image quality (IQ) map from the EBSD measurement, and consistently showed that the clustering algorithm is able to accurately classify indents located within the martensite islands (cluster ID = 1, Figure 11D). A clear identification and separation of the soft ferrite phase was also achieved (cluster ID = 3, Figure 11G). On the other hand, the correlative method here identified that cluster 2 contains not only indents located in ferrite grains close

to the ferrite-martensite interface but also indents placed on grain boundaries or triple junctions between ferrite grains (Figure 11E,F).
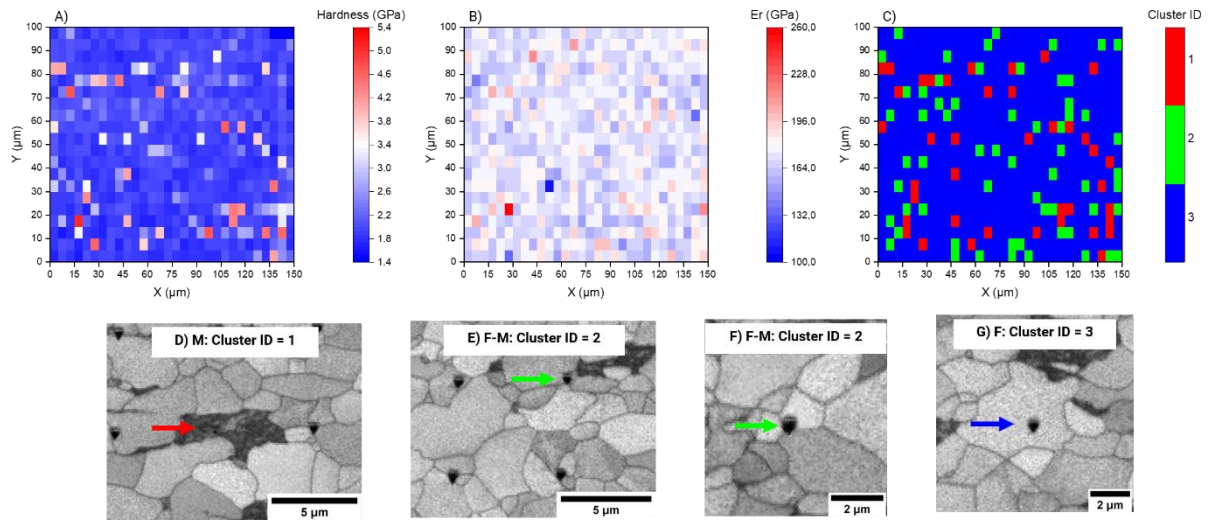


Figure 11: Hardness A) and indentation modulus B) heatmap of M1 as well as the K-means clustering result C). The IQ images in Figure D) – G) illustrate a representative indent (marked by color-coded arrow) for each cluster. The pixels of the heatmap are spatially distributed by 5x5 µm².

As the elbow method did not show a clear inflection point for M2, and the calculated clusters strongly overlap, the clustering result of k = 2, 3 and 4 were compared with the microstructure to check the correlation. Due the displacive transformation during formation of bainite, the misorientation gradually increases within the granular bainite grain. Therefore, point to origin measurements on the EBSD scans were applied to distinguish the granular bainite from the polygonal ferrite phase according to a misorientation threshold of 3° [18]. It has been shown that deformed steels can contain polygonal ferrite grains which are subdivided by sub-grain boundaries [50]. Therefore, the 3° criterion was used to distinguish between both phases, without measuring across sub-grain boundaries with a misorientation angle between 3 – 5°. This means a grain will be classified as granular bainite if the point to origin measurement exceeds 3° within the grain area otherwise it counts as polygonal ferrite. The EBSD IQ image in Figure 12A shows a representative example of grain A (grain boundary outlined in black) and grain B (grain boundary outlined in red) with misorientation profile vector displayed by the blue arrow. Consequently, grain A and grain B were classified as granular bainite and polygonal ferrite, respectively, based on the point-to-origin misorientation shown in Figure 12B. It is also necessary to note that the hardness values of grain A ($H$ = 3.0 GPa) and grain B ($H$ = 2.8 GPa) is also similar despite the misorientation differences. Another possible influencing variable for the comparable hardness of the two grains could be the proximity of the indent to a HAGB and thus leading to a constrained dislocation movement. The increasing hardness in the vicinity of a HAGB has already been observed in previous investigations [148,149]. Only the indentation modulus shows a difference of 206 GPa to 183 GPa for the selected granular bainite polygonal ferrite grain. Subsequently, a number of other grains where the indent was located in the grain interior were classified as shown in Figure 12 and compared

with the clustering result of $k = 2$, 3 and 4. An average granular bainite and polygonal ferrite hardness and indentation modulus of $(3.2 \pm 0.2)$ GPa and $(3.0 \pm 0.1)$ GPa as well as $(181 \pm 10)$ GPa and $(201 \pm 7)$ GPa was calculated based on the classified grains, respectively. This correlation revealed a significant number of incorrectly indexed grains for both phases. Hence, K-means clustering was not able to adequately classify the nanoindentation results on material M2 to separate both constituents to its individual cluster as for the case of M1. Therefore, the role of HAGBs and the impact of similar mechanical properties between the tested constituents on the clustering result was further investigated on the heat-treated sample S3.
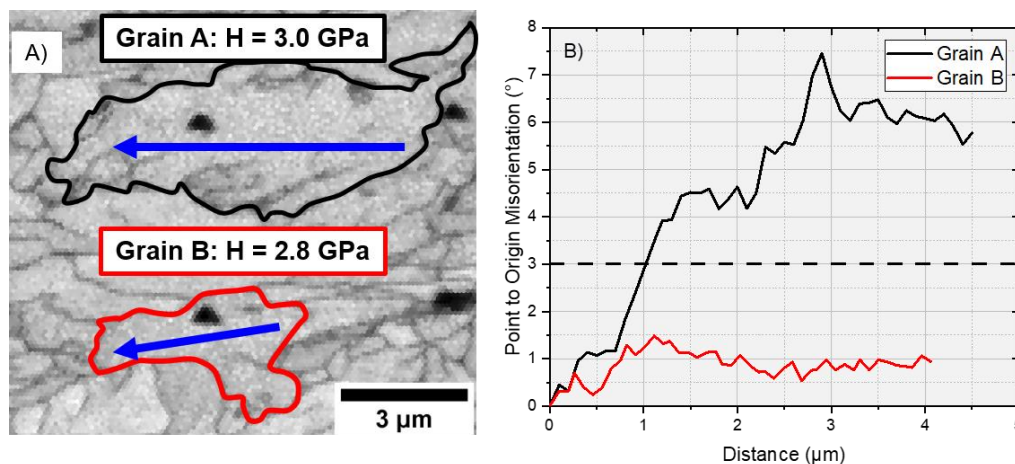


Figure 12: The IQ image shows two representative grains of the granular bainite (grain boundary outlined in black) and polygonal ferrite (grain boundary outlined in red) A). Identification was performed by measuring the point to origin misorientation (blue vector) in each grain which is shown in B). The 3° threshold to separate both phases is displayed as the dashed horizontal line.

### 4.2.2 Testing grain pairs on a heat-treated ferritic steel

Heat treatment was used to obtain polygonal ferrite grains with a diameter of 50-100 µm, allowing the selection of four grain pairs divided by a HAGB and to perform several nanoindentation tests over each grain boundary. EBSD and nanoindentation measurements were also carried out over four FIB-marked polygonal ferrite grain pairs (GP-1 to GP-4) separated by a HAGB. The results of hardness versus indentation length of GP-1 to GP-4 and the KAM map of the corresponding grain boundary region with the inverse pole figure (IPF) for each grain are given in Figure 13A-D. The KAM map of all four tested grains pairs shows that the KAM value is homogeneously distributed and varies between $0 - 1°$; HAGB and LAGB are displayed as black and blue lines, respectively. Misorientations are accumulated only in few regions and form LAGBs that do not lead to a change in the hardness value. The grain boundary position was set as zero in all four grain pairs and thus, the x-axis represents the distance between the indent and grain boundary. An increase of hardness is observed in the vicinity of the grain boundary for three grain pairs GP-1, GP-3 and GP-4. The hardness-affected zone reaches a length of up to 20 µm. Only GP-2 exhibits a constant hardness level over the tested length. Moreover, the average hardness of

each grain was calculated to compare it with the corresponding IPF, neglecting the 20 µm affected zone adjacent to the HAGB. It follows that the average hardness level of each grain depends on the crystallographic loading axes. In addition, the closer the crystallographic orientations are to each other, the smaller the differences in hardness across the HAGB. How this affects the clustering is discussed in the Discussion section.
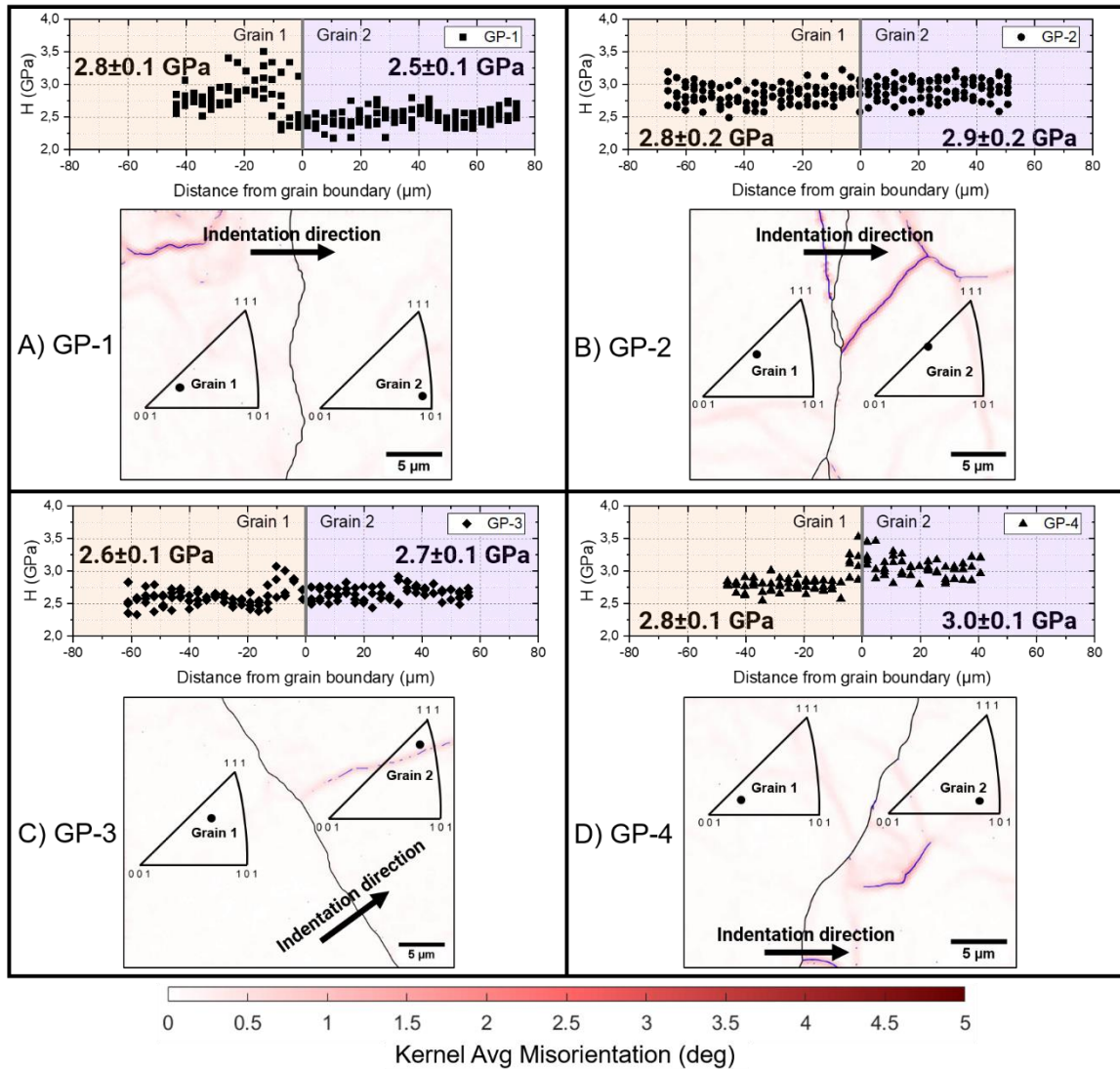


Figure 13: The hardness over the distance from the grain boundary, the average hardness of each grain neglecting the 20 µm zone next to the grain boundary and the KAM map with the IPF of the corresponding grain is shown for GP-1 A), GP-2 B), GP-3 C) and GP-4 D). The position of the HAGB was set as zero in all cases. Grain boundaries (>5°) are displayed as black lines and sub grain boundaries (2-5°) as blue lines.

The elbow method was then applied on the data sets obtained for the heat-treated sample S3. As for M1 and M2, $H$ and $E_r$ were used as input parameters and the SSE results were normalized (Figure 14). The histogram in Figure 14 highlights that an average $H$ and $E_r$ of $(2.7 \pm 0.5)$ GPa and $(193 \pm 34)$ GPa were determined, respectively, by applying a Gaussian function to describe both distributions. Similar to the result for M2, the elbow curve of S3 shows a continuous progression without a clear inflection point.

To investigate how K-means clustering deals with the different hardness levels between the grains and the possibility of separating outliers from the average grain hardness, the number of clusters was increased.
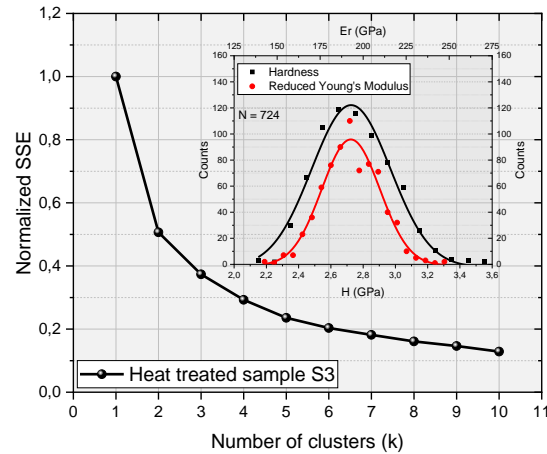


Figure 14: Result of the elbow analysis for heat-treated sample S3 consisting of GP-1 to GP-4. The subfigure additionally shows the distribution of the input variables $H$ and $E_r$.

As such, analyzing the clustering result was concentrated on $k = 2$ and $k = 3$ to reveal how K-means separated the outliers and different hardness levels from each other. Figure 15 gives two representative examples for the hardness; grain pair GP-1 (Figure 15A,B) and GP-2 (Figure 15C,D), after applying K-means on the whole dataset of the heat-treated sample; each color represents one cluster. Thus, it is an advantage to simulate a grid nanoindentation test and to compare the clustering result between the grain pairs by applying K-means on the whole dataset. The grain boundary position was again set to zero as in Figure 13. In the case of grain pair GP-1 (Figure 15A), K-means was able to separate the average hardness level from the outliers next to the HAGB. With $k = 2$ in the case of GP-2 with a higher average hardness level (Figure 15C), almost all data points were arranged into the same cluster as for the outliers in GP-1. By further increasing to $k = 3$, the clustering shows in the case of grain pair GP-1 (Figure 15B) a refined result. K-means was not only able to separate the outliers next to the HAGB from the average hardness level, but could also split the different hardness levels of grain 1 and grain 2 into two clusters. In comparison, K-means distinguishes in the case of GP-2 $k = 3$ the constant hardness values over the tested length into two parts (Figure 15D). Since all datapoints were clustered together, the assignments allow for comparison of the cluster ID between GP-1 and GP-2. It shows that K-means could separate the grains from the outliers in case of GP-1 but assigned most of the datapoints of GP-2 to the same cluster ID as the outliers of GP-1 in case of $k = 2$ and $k = 3$. Consequently, the optimal number of clusters is not equal for all tested grain pairs and needs to be validated separately.
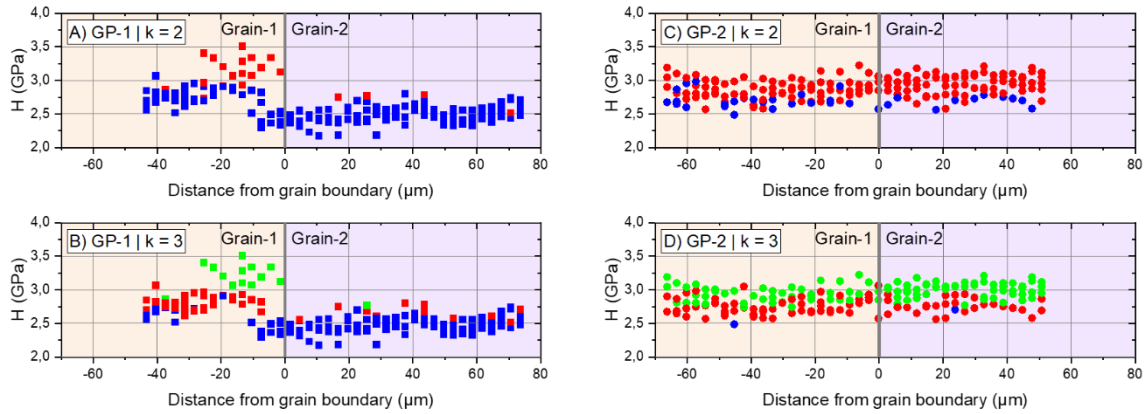
Figure 15: Hardness values over the distance from the grain boundary position for GP-1 A) and B) and GP-2 C) and D) illustrate the K-means clustering result by using $k = 2$ and $k = 3$. Each color represents one cluster. The shown examples are extracted after K-means was applied to whole dataset from the heat-treated sample.

## 4.3 Discussion

Nanoindentation tests were performed on material M1, containing martensite and polygonal ferrite, and material M2 with granular bainite and polygonal ferrite microstructural constituents. The hardness distribution of both selected materials in Figure 9D shows that the ferrite of M2 has a higher hardness compared to the ferrite of M1. It has been shown that an increasing density of geometrically necessary dislocations (GNDs) leads to an increase of hardness [111]. It might be reasonable that due to the different production route of both materials, that the GND density within the polygonal ferrite of material M2 is higher and thus offers more obstacles for dislocation glide; however, this was not within the scope of this study. On the other hand, previous investigations showed that the carbon concentration does not affect the ferrite hardness since the ferrite constituent has in both investigated materials the same carbon solubility [150]. The experiments revealed for M1 a bimodal hardness distribution whereas the elbow method indicates $k_{optimal} = 3$ as the optimal number of clusters. It was shown that K-means was able to accurately assign the $k = 1$ and $k = 3$ clusters to those indents located within a ferrite or martensite grain, respectively. Indents located within ferrite grains but next to a martensite island were separated into the second cluster. This result can be rationalized by higher near-interface carbon concentrations [70], and a higher local density of geometrically necessary dislocations [32,35,65,66]. However, K-means assigned not only the indents near a martensite island into the second cluster, but also indents on ferrite-ferrite grain boundaries or on ferrite grain triple junction. Both Soer et al. [148] and Britton et al. [149] performed nanoindentation tests over a HAGB and detected an increasing hardness in the vicinity of the grain boundary. Both concluded that a HAGB acts as an obstacle to the activated dislocations during the indentation testing where they pile-up until the applied force is high enough to initiate dislocation nucleation within the neighboring grain. Moreover, small topography differences at the grain boundary were observed under the SEM. The impact of mechanical polishing on the surface topography has been observed [151] and may affect the contact area of the indenter in

the vicinity of a grain boundary used for evaluating the nanoindentation measurements. Subsequently, M1 contains a martensite phase fraction of 8% according to K-means clustering and agrees with the LOM images. This agrees well with material supplier's result, which was determined by LOM investigations.

In comparison to the M1 dual phase steel with the distinct hardness levels of each phase, K-means clustering did not reveal an accurate microstructural separation of the polygonal ferrite and granular bainite phases. It is rationalized that K-means clustering is not able to separate polygonal ferrite and granular bainite (M2) into two clusters as: (i) the similar mechanical properties of both phases; (ii) the impact of the HAGBs during nanoindentation testing, in combination with the substructure variety in the bainite phase, leads to a broad spread of hardness values. Indeed, from our EBSD investigations we also observed granular bainite grains with a hardness level within the polygonal ferrite range. A variation in substructure size is well known and can result from different cooling rates [7]. Since, it has been found that the bainitic sub-microstructure size is strength-determining [89], electron channeling contrast imaging (ECCI) investigations were performed on grains identified as granular bainite to reveal the substructure of M2. ECCI is able to resolve the sub-microstructure details due to a high angular resolution of $0.28 - 0.57°$[152]. More detailed information on the method used can be found elsewhere [152]. Two representative granular bainite grains are provided in Figure 16, where the grain boundary of grain C and grain D is outlined in yellow and red, respectively. Depending on the crystallographic direction, the blocks of the substructure appear with differing contrast. The misorientation between the different blocks is also related to the accumulated misorientation profile (Figure 12) which was used to distinguish between polygonal ferrite and granular bainite. A changing block size is observed between, and even within, grains C and D. An average contact radius of $(21 \pm 1)$ nm of the nanoindentation tip within the selected granular bainite grains was reached and leads to an average radius of the plastic zone of $(213 \pm 3)$ nm [67]. This indicates that depending on the location of the indent within a grain, the hardness values can be further influenced by the different substructure sizes; the nanoindentation method is particularly sensitive to spatial heterogeneity within grains of the microstructural components.
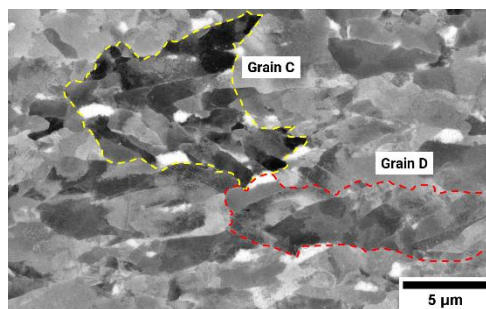


Figure 16: Backscatter electron image of the two-representative granular bainite grains C and D (the grain boundary (>5°) is outlined in yellow and red, respectively) illustrates the variation of the substructure between different grains and within the same grain.

Furthermore, the selected granular bainite and polygonal ferrite grains have a hardness difference of only 6% compared to M1 with at least 10% between cluster 1 and cluster 2. This indicates that the quantifying input parameter (e.g. hardness) has to have a minimum difference of 10% between both phases, to obtain a reliable K-means classification. However, this threshold may depend on the standard deviation and the number of data points of each cluster. Table 7 in the appendix indicates that K-means will subdivide data points with similar hardness values according to the indentation modulus. However, this parameter did not reveal a good correlation between the clustering result and the EBSD classification. It was found that residual stresses can increase the error of estimating the true contact area of the indenter since constituents under a higher compressive stress state often exhibit a stronger indentation pile-up [153,154]. Consequently, the hardness and indentation modulus can both be affected, with modulus values varying up to 10% [153]. Vlassak et al. [155] measured that the obtained indentation modulus of an elastically anisotropic material such as Cu varied between $10 - 25\%$ depending on the crystallographic orientation. This effect should be similar for Fe and subsequently, could cause a larger scatter for each constituent. Furthermore, plastic deformation may cause a pile-up or sink-in behavior of the tested material and thus, increases the contact area of the indenter [156]. McElhaney et al. [157] presented a technique to consider the sink-in and pile-up effect on the contact area by using SEM images and measurements of the contact stiffness. Our data (Table 7) shows an unexpected separation of phases due to differences in the measured indentation modulus, which should be comparable for both constituents. Atomic force microscopy investigations on selected granular bainite and polygonal ferrite grains revealed that granular bainite is characterized by a 10% higher pile-up behavior. The differences in pile-up behavior can for instance be caused by residual stresses or strain hardening, which is known to differ for the constituents of our microstructure [23]. Subsequently, the systematic formation of a larger indentation pile-up and / or sink-in for granular bainite grains caused a systematic error. However, the pile-up behavior may vary depending on the substructure formation within each granular bainite grain as mentioned above (see Figure 16). Thus, the pile-up and sink-in behavior was not additionally corrected for both constituents.

The indentation size effect (ISE) was also considered as an influencing factor on phase separation by nanoindentation. Several investigations pointed out that a decreasing indentation depth leads to a higher nanohardness [110–112]. These studies showed that a constant hardness can be achieved as the lasting penetration depth is approx. above 1 µm. Due to the small grain size of M1 and M2, it was necessary to use a maximum load of 3 mN leading to a lasting penetration depth of $115 - 198$ nm and $90 - 213$ nm, respectively. Subsequently, it has to be assumed that the real nanohardness of each constituent was overestimated due to the small penetration depth. Since the distribution for each phase is even smaller than the total range of the lasting penetration depth, the relative error caused by the ISE was neglected.

A further important aspect for analysis of materials containing two phases with similar mechanical properties is the dataset size and the spatial resolution. In this study, a representative area of each

material was tested. The dataset size utilized in the case of M1 was large enough to separate both phases. But for samples with similar mechanical properties of the individual phases, such as M2, it could be necessary to significantly increase the indent number per grain and the tested area. In addressing this, phase mapping using high-speed nanoindentation could allow for mechanical property characterization over much larger areas with higher spatial resolution [72]. However, to perform high-speed nanoindentation with high spatial resolution, the load must be reduced to avoid the interaction of the elastic-plastic zone of the adjacent indents [158]. Therefore, the impact on shallow indents will increase with the material's complexity, e.g. different substructure sizes and grain boundaries. Thus, it will remain a challenging task to use nanoindentation results as input variables for K-means clustering.

In order to investigate the impact of HAGBs between two ferrite grain pairs on the nanoindentation and K-means clustering result, we extended the investigation to the heat-treated sample S3. The goal of this part was to investigate the impact of a HAGB between two identical phases on the nanoindentation tests and how this can affect the K-means clustering result. As shown in Figure 13, single ferrite grains own a different hardness level depending on the crystallographic plane perpendicular to the loading direction. Another noticeable feature is the fact that the HAGB did not led to an increase in hardness for all grain pairs tested (GP-2); this may be due to surface topology for grain pairs with equivalent crystallographic orientations caused by the OPA polishing step (grain pairs with a similar orientation will show a smaller difference in height across the grain boundary) [151]. In contrast, GP-1 shows that the affected area may extend over several micrometers. This might be caused by a combination of differences in height between the two grains with differing orientations, a disabled dislocation movement in the immediate vicinity of the grain boundary introduced by nanoindentation measurement itself, or a shallow grain boundary underneath the tested surface which acts again as a barrier to the activated dislocations [148,149,151]. The indentation modulus varied up to 13% depending on the crystallographic loading axes of the tested grain pairs and could be related to the elastic anisotropy [155]. The elbow method did also not indicate the optimal number of clusters for sample S3. In comparison to previous investigations where the optimal number of clusters were user-defined or the constituents possessed distinct hardness levels, the grains of S3 own similar mechanical properties as the polygonal ferrite and granular bainite of material M2 [64,139,141]. It is indicated by the clustering result in Figure 15 that in optimal number of clusters $k$ is not identical for all grain pairs. This is caused by the fact that the hardness and indentation modulus level of individual grains and outliers overlap and K-means cannot distinguish between them. It might be possible that the constituents of material M2 contain also different hardness and indentation modulus levels depending on the crystallographic orientation which will contribute to a broader distribution of both parameters and thus, causing a larger overlap between the different constituents. The higher chance to test the vicinity of a grain boundary and the reduced datapoints for each phase will further contribute to the challenging goal revealing a reliable phase quantification.

Thus, the investigations showed that the elbow method was able to indicate the right optimal number of clusters and K-means to separate them from outliers depending on the strength level of the individual constituents. Once the individual phases possessed similar mechanical properties, both methods will be constrained due to the influence of grain boundaries, substructure and hardness values depending on the presenting crystallographic plane.

## 4.4 Conclusion

The present study utilized hardness and indentation modulus values, derived from nanoindentation of dual phase (M1) and bainitic steels (M2), as input parameters for the elbow method to determine the optimal cluster number and K means classification of both data sets. The elbow method could clearly determine the optimal number of clusters in the case of the ferrite-martensite dual phase steel. Correlating the microstructure with the clustering result revealed that the ferrite and martensite were separated into clusters together with indents located at a ferrite-martensite or on a ferrite-ferrite boundary. However, K means could not clearly separate the granular bainite from the polygonal ferrite. Selected grains were classified as granular bainite and polygonal ferrite by the introduced 3° EBSD threshold. Based on the classified grains, both constituents had a different hardness level of 6% compared to M1 with a minimum hardness difference of 10% between cluster 1 and cluster 2. This indicates that the K means input variables have to differ by at least 10% for the current microstructure to achieve a reliable classification; depending on the hardness and indentation modulus distribution width of each constituent. Furthermore, a sample from the bainitic material was heat treated to investigate the impact on the optimal number of cluster determination with the elbow method and on the clustering result with K means. The further investigations on the heat-treated sample showed different hardness level depending on the crystallographic plane perpendicular to the loading direction. Moreover, not all tested grain pairs showed increased hardness values next to the HAGB. Only grain pairs whose crystallographic orientation with respect to the loading direction was almost identical did not show a pronounced increase in hardness. Since the elbow method did not reveal an inflection point to indicate the optimal number of clusters, we focused on the analysis of two and three clusters. The clustering result revealed that due to the different hardness levels of the ferrite grains and the outliers, the optimal number of clusters is not identical for all tested grain pairs. Therefore, if the constituents have comparable mechanical properties, (i) the influence on the measured hardness in the vicinity of grain boundaries, (ii) the similar mechanical properties of both phases and (iii) the inhomogeneous substructure of granular bainite and resulting mechanical properties between different and even within large grains are the main constraining factors in applying K means clustering for microstructure classification based on nanoindentation input data.

# 5 Automated classification of granular bainite and polygonal ferrite by electron backscatter diffraction verified through local structural and mechanical analyses[2]

## 5.1 Introduction

High-strength low-alloy (HSLA) steels are widely used in several applications, e.g. constructions or pipelines thanks to their mechanical and technical properties (e.g. weldability) [5–8]. This type of steel is commonly composed of a complex mixture of polygonal ferrite, degenerated pearlite, bainite, and residual martensite-austenite constituents. The volume fraction, distribution, and morphologies of these individual phases greatly influence the overall mechanical properties [9,13,45,159]. It is supposed that granular bainite can only form during continuous cooling which is compared to an isothermal heat-treatment widely used in the industrial production process [23]. Granular bainite is defined as a composition of irregular ferrite having irregular grain boundaries and a carbon rich second phase which is distributed between the irregular ferrite grains and commonly composed of degenerated pearlite or martensite/retained austenite [5]. This is caused by the increasing carbon concentration within the austenite during the continuous cooling process which stabilized the austenite and lead to the formation of carbon rich austenite [3]. Moreover, the formation of polygonal and irregular ferrite leads to a decreasing austenite phase fraction and thus, the carbon concentration further increases within the untransformed austenite and forms various carbon rich second phase constituents [3,160]. However, it has been found that the transformation range of the individual constituents partly overlap during the continuous cooling process which aggravates the phase classification [161–163].

---

It is a challenging task to characterize irregular ferrite and polygonal ferrite, since both are characterized by a granular morphology and e.g. light optical microscopy (LOM) does not have a sufficient resolution to reveal the differences [18,23]. It turned out by transmission electron microscopy (TEM) investigations that irregular ferrite is subdivided by small ferrite sheaves or equiaxed grains depending on the applied cooling rate [7,23,37]. In addition, one further characterizing feature is the absence of carbides between irregular ferrite substructure that further impedes the differentiation between irregular a polygonal ferrite [23]. However, TEM investigations do not allow statistical phase analysis due to the limited investigated volumes. As a result, scanning electron microscopy (SEM) has been used to obtain reference images and texture parameters from isothermally produced samples. The images and texture data were implemented into a support vector machine [51]. The ideal structures were well characterized by this approach, but it remains challenging to capture the whole variety of the individual constituents [7,27,162].

In comparison, electron backscatter diffraction (EBSD) has been used as a powerful tool to identify phases and perform orientation analyses. EBSD shows no difficulty in differentiating austenite from ferrite, but it remains a challenge in distinguishing lath bainite from martensite or granular bainite from polygonal ferrite since these phases only exhibit little tetragonality from the body-centered cubic (BCC) phase. As a result, studies show that these phases demonstrate similar microstructural morphologies and misorientation distributions [7,18,56]. Despite the difficulties, previous studies reported that granular bainite grains exhibit a higher misorientation within the grain compared to polygonal ferrite [18,21,37]. This is caused by the onset of a displacive transformation which governs the granular bainite formation and it can only be accommodated plastically by geometrically necessary dislocations. This indeed offers an opportunity for phase identification between granular bainite/polygonal ferrite. In fact, researchers have proposed different methodologies, broadly applying either grain- or pixel-based parameters [56,57,164]. Zaefferer et al. [52] compared in details the pattern quality, grain reference orientation deviation and kernel average misorientation (KAM) to characterize the bainitic and ferritic phases, and concluded that only the pixel-based KAM value gives a reliable separation of the bainitic and ferritic phase [52].

Based on Keehan et al.'s study, an orientation gradient of $3 - 6°$ per 10 µm was first defined by point-to-origin measurements to distinguish between granular bainite and polygonal ferrite [21]. Later, Chen et al. [18] correlated the orientation gradient within the individual grain and the KAM to achieve a reliable phase classification of granular bainite and polygonal ferrite. Moreover, the impact of a different step size and kernel size (kernel size = step size ∗ n-th nearest neighbor) was studied and it was found that the kernel size has to be comparable to the substructure size and in that case further refinement of the step size does not play an import role to reveal the optimal classification of both constituents. In terms of the misorientation threshold, it was further suggested that a grain with an orientation gradient larger than $3°$ counts as granular bainite and is thus independent of the measured

length; this was related to the fact that the correct kernel size covers several bainite subunits and can exceed 3°. Within this study [18], a grain tolerance angle of 10° was used to define the grain boundary. However, it has been shown that polygonal ferrite grains of a deformed material can be also subdivided by boundaries with a misorientation smaller than 10° [50]. Zhu et al. [88] determined that the effective grain size correlates well with the inverse lath size of bainite by using a boundary misorientation angle of $2 - 7°$. This additionally indicates that the application of a smaller grain boundary tolerance angle may better represent the mechanical strength level of the individual constituent. However, a phase separation and quantification based on the KAM-threshold has not been automated and validated by correlative investigations.

Besides using EBSD-based parameters to characterize the selected HSLA steel, nanoindentation and chemical analysis have been employed to assist in differentiation of the constituents. Specifically, nanoindentation tests were utilized to separate bainitic ferrite containing carbon rich precipitates between the substructure and ferrite according to the measured hardness [63]. A phase classification by using nanoindentation remains challenging for both lath bainite and martensite as well as granular bainite and polygonal ferrite due to the comparable mechanical properties [165]. Electron probe microanalysis has been used to differentiate ferrite and martensite according to their carbon concentration [166,167]. However, the carbon concentration caused by the electron beam required extensive experimental effort to minimize carbon contamination and achieve reliable carbon differentiation. Subsequently, the present study considers Time-of-Flight Secondary Ion Mass Spectrometry (ToF-SIMS) analysis as a possible tool to test whether different carbon concentrations between the constituents can be resolved as ToF-SIMS has a sufficient high lateral resolution (approx. 0.1 µm) to resolve individual grains and phases. In addition, the detection limit for light elements is with 6 ppm also high enough, since atom probe tomography experiments showed that irregular ferrite grains contain a carbon concentration of 50 to 750 ppm [22,168,169]. However, ToF-SIMS has not yet been used to distinguish granular bainite from polygonal ferrite.

To the author's best knowledge, it has not been tried to develop an automated phase differentiation and quantification of granular bainite and polygonal ferrite by using EBSD-based KAM mapping. An additional feature of this work is the subsequent correlative electron channeling contrast imaging (ECCI) investigations and point-to-origin measurements of the orientation gradient within the grain interior to validate and adjust the characterization tool. Figure 17 schematically illustrates the classification process from the EBSD measurement until the automated phase identification and the conducted analysis to validate the achieved results. The classification system was tested on a rolled HSLA steel containing granular bainite and polygonal ferrite.

Orange = Granular bainite | blue = Polygonal ferrite
black line = grain boundaries
Blue lines = sub boundaries
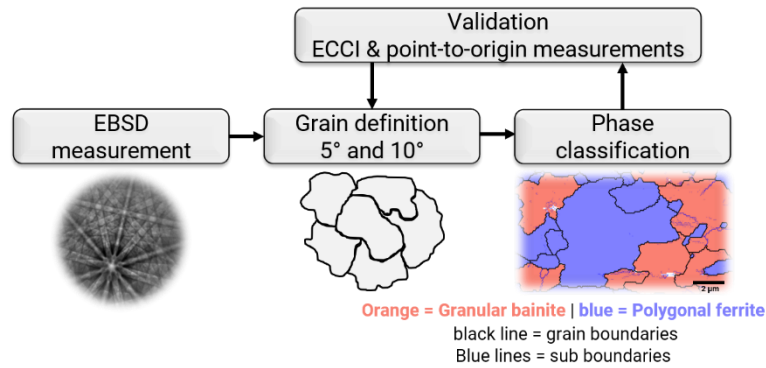
Figure 17: Schematic illustration of the classification process. After performing the EBSD measurement, the grains were defined by a grain tolerance angle of 5° and 10°. Both constituents, polygonal ferrite and globular bainite were separated by using a KAM threshold of 3°. ECCI and point-to-origin measurements were conducted to validate the achieved results.

## 5.2 Results and Discussion

### 5.2.1 Preliminary microstructural characterization

The investigated microstructure is illustrated by a LOM image in Figure 18A and the inverse pole figure (IPF) in Figure 18B. The polygonal and irregular ferrite grains in Figure 18A are white etched whereas the dark etched carbon rich second phase was identified as degenerated pearlite and martensite/retained austenite islands. The microstructural features of degenerated pearlite and martensite/retained austenite were not separately considered within this study due to their size and comparable consistency to irregular ferrite within the EBSD dataset (see Section 5.2.5). Consequently, the phase classification and quantification by EBSD will only distinguish between polygonal ferrite and granular bainite including the carbon rich second phase.

The IPF image within Figure 18B gives a more detailed information regarding the microstructural complexity. The grain boundaries defined by a tolerance angle of 5° are displayed as black lines. The grains are elongated along the rolling direction and fine structured. Two representative $80 \times 80$ µm² scan areas were used to calculate the grain size and misorientation angle distribution, shown in Figure 18C and D. The grain size distribution (Figure 18C) was fitted by using a log-normal function and revealed an average grain size of $(4.2 \pm 0.6)$ µm. It was not possible to separate both constituents by LOM, since the resolution is too low to resolve the sub-sheaves of the irregular ferrite grains.

A further indication that the investigated material consists of polygonal ferrite and granular bainite is given by the misorientation angle distribution shown in Figure 18D. The characteristic misorientation angle distribution of a granular bainite microstructure is described by a minor peak $< 20°$ and a broad distribution around 45° [5]. Since this is in accordance with our observation, it was concluded that the investigated material contains granular bainite. The small peak at 30° is related to mis-indexed pixels (pseudosymmetry) and can have different origins which are explained in detail elsewhere [57]. Hence, the morphology, grain size and misorientation angle distribution did not allow to distinguish between granular bainite and polygonal ferrite grains and further EBSD analysis were conducted.
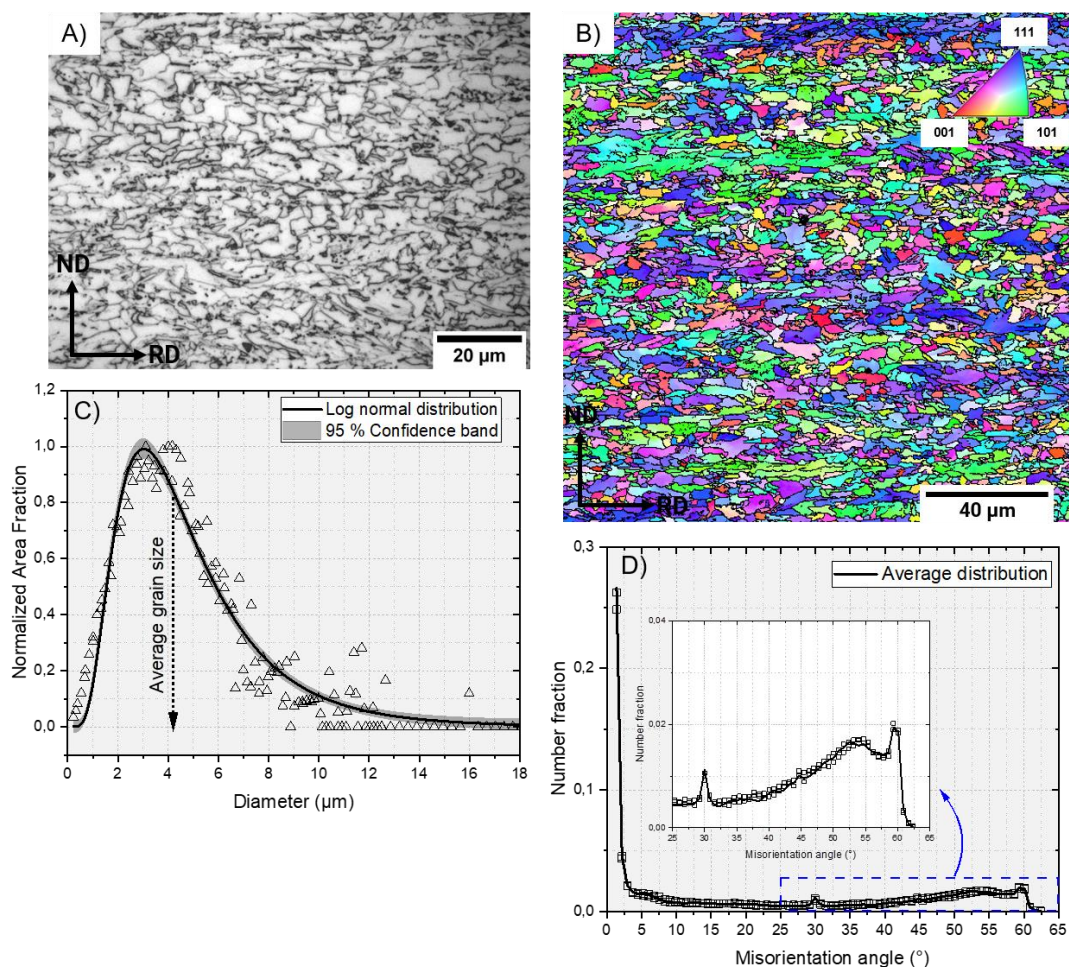
Figure 18: A) Representative LOM image of the investigated microstructure. Both $80 \times 80\ \mu m^2$ scan areas were taken along the transverse direction and is illustrated by the IPF image B). C) and D) show the grain size distribution, fitted by using a log-normal function, and the average misorientation angle distribution of both scan areas.

Point-to-origin measurements have been suggested as a further suitable characterization technique to separate both constituents according to the orientation gradient [3,18,21,37]. Chen et al. [18] utilized those measurements to measure the orientation gradient inside the grains and differentiated both constituents according to a misorientation threshold of 3°. Consequently, point-to-origin measurements were also performed to characterize 22 selected grains. With respect to the 3° threshold, nine grains (PF-1 – PF-9) were classified as polygonal ferrite (see Figure 19A) and 13 grains (GB-1 – GB-13) as granular bainite as the misorientation was below or above the selected 3° threshold, respectively (see Figure 19B). The point-to-origin measurement procedure is shown in Figure 19A-B by two representative grains (PF-5 and GB-2). The formation history of each constituent is responsible for the different orientation gradient inside the grains. Polygonal ferrite grains start to nucleate at the prior austenite grain boundaries and the reconstructive transformation does not typically include large strain gradients inside the grain interior [4,23]. Granular bainite nucleates also at the prior austenite grain boundaries and forms a substructure due to the displacive transformation. This has been proven by TEM investigations [15,16,23]. The continuous cooling process leads to the formation of shear stresses which

are relaxed by geometrically necessary dislocations (GNDs) and the associated formation of sub-grain boundaries [48,49]. Accordingly, the 22 selected grains can be manually categorized by using the point-to-origin measurement method. Subsequently, further nanoindentation tests were utilized to validate these results. In comparison to the distinct classification according to the misorientation, the load and depth curves in Figure 19C illustrate that the nanoindentation tests did not allow a clear phase separation due to the continuous transition of the load and depth curve. Only grain GB-2 shows a higher hardness compared to the other tested grains. Subsequently, an average nanohardness of polygonal ferrite and granular bainite, and reduced Young's modulus were measured according to the classification by the orientation gradient; the results are summarized in Table 4. A previous investigation revealed that the bainitic yield stress is proportional to the inverse lath size of sub-boundaries defined by a boundary misorientation of $2-7°$ [88]. Therefore, a different bainitic substructure could explain different hardness levels but not the similar mechanical response of the polygonal ferrite grains. Further investigations were conducted to clarify this phenomenon and will be presented in Section 5.2.4.
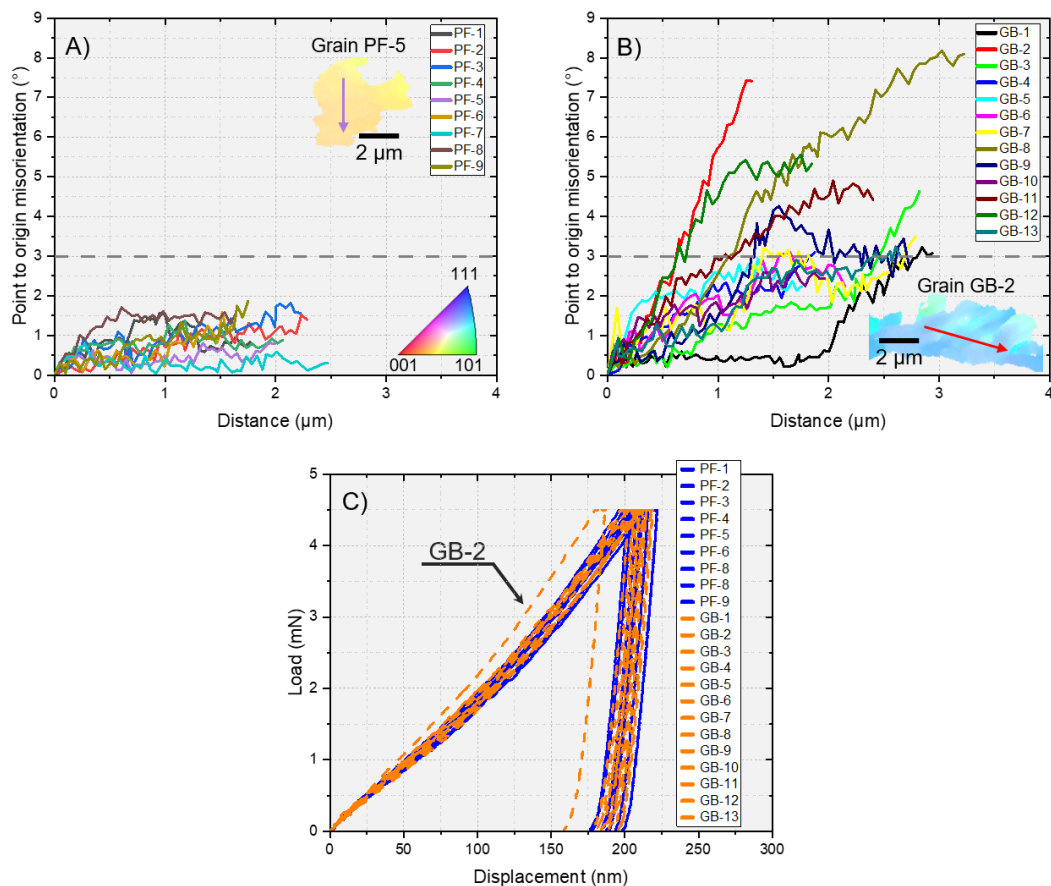


Figure 19: Based on the measured misorientation inside 22 selected grains were nine grains (PF-1 to PF-9) classified as polygonal ferrite A) and thirteen grains classified as granular bainite B). A) and B) additionally contain two representative examples (PF-5 and GB-2) to illustrate the point-to-origin measurement (colored arrow). The 3° threshold to separate both phases is marked as a gray dashed line. The nanoindentation load and depth curves of the 22 tested grains C) did not allow a classification between both constituents; only grain GB-2 showed a distinct separation.

Table 4: Summary of the calculated average hardness and reduced Young's modulus obtained by nanoindentation. The grains were classified as polygonal ferrite and granular bainite according to the EBSD misorientation measurements.

| Phase | Avg. $H$ | Stand. dev. | Avg. $E_r$ | Stand. dev. | # indents |
|---|---|---|---|---|---|
| Polygonal ferrite | 2.6 | 0.1 | 192 | 9 | 9 |
| Granular bainite | 2.7 | 0.1 | 198 | 15 | 13 |

The chemical composition, specifically the carbon content of the steel, was also considered for achieving a separation of both constituents. Since granular bainite is formed by a displacive transformation which hinders carbon diffusion, attempts were made to measure the differences in carbon concentration between polygonal ferrite and granular bainite by ToF-SIMS. Due to air contact of the samples, their topmost layer contains many different air-borne hydrocarbon contaminations. Therefore, the samples were sputter cleaned *in vacuo* directly before imaging using a low energy $Cs^+$ beam. Organic contaminations were removed easily, as observed by the rapidly dropping hydrocarbon signals and increasing signals of iron oxo clusters, but erosion of the material underneath was kept below approx. 1 nm due to the low sputter ion energy and dose. Furthermore, cesium atoms implanted in the sample surface increase the ionization yield of negative secondary ions used for subsequent imaging. Figure 20A shows the lateral distribution of the carbon concentration measured on a representative scan area based secondary ions ($C^-$, $CH^-$, $C_2^-$, $C_2H^-$, $C_3^-$, $C_4^-$) superimposed with the grain boundary structure (grain tolerance angle 5°) which were obtained from the EBSD measurement. Single hydrogen containing species can arise due to adsorption of hydrogen from the residual atmosphere in the spectrometer's recipient. The logarithmic intensity scale of the carbon concentration additionally highlights smaller values and indicates a homogeneous carbon distribution overall the grain areas. Only a few small spots with a higher carbon concentration were detected and assigned to artefacts on the sample surface or to the lasting imprint of a diamond Berkovich indenter. Moreover, two representative grains (PF-5 and GB-8) were marked and characterized by EBSD point-to-origin measurements; the approximate position of the point-to-origin measurement is indicated by the blue arrow within each grain. One can recognize that PF-5 and GB-8 were identified according to the maximum misorientation as polygonal ferrite and granular bainite, respectively (shown in Figure 20B). It has been proven that ToF-SIMS is capable to reach a mass and lateral resolution of 6 ppm and 100 nm for light elements, respectively [168,169]. As a result, ToF-SIMS had originally been thought to be able to resolve the investigated microstructure and different carbon concentrations between the constituents. However, previous studies pointed out that at lower cooling rates the carbon atoms are still able to diffuse away from the ferrite-austenite interface, which leads to a larger carbon gradient within the residual austenite [12]. Hence, the reduced carbon saturation impedes the formation of carbon precipitates between the sub-blocks and only small quantities of retained austenite/martensite or degenerated pearlite are formed

depending on the degree of carbon enrichment [3,12]. Thus, it was not possible to identify individual grains according to their carbon concentration as the representative SIMS measurement shows.

These experiments further illustrate the difficulty to reveal a reliable phase classification of such microstructures with similar properties using either chemical or mechanical approaches. Since, point-to-origin measurements showed a clear separation of the selected grains, the KAM and the 3° threshold were used to create an automated classification workflow. These results in terms of phase separation and quantification on the tested material, as well as the corresponding validation studies, are presented below.
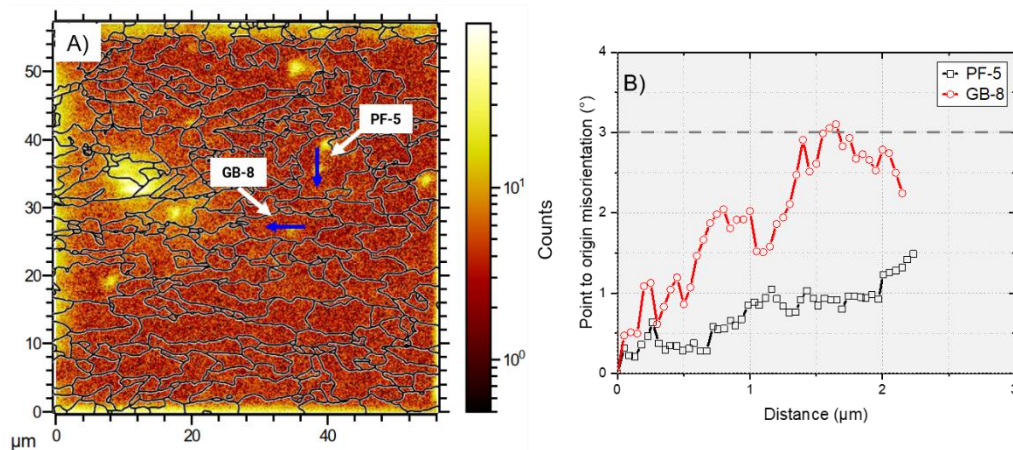


Figure 20: A) shows a representative ToF-SIMS scan area and the lateral intensity distribution of summed signals of $C^-$, $CH^-$, $C_2^-$, $C_2H^-$, $C_3^-$, and $C_4^-$. In addition, the superimposed grain boundary structure (grain tolerance angle 5°) was obtained from the EBSD measurement and illustrated by black bold lines. B) The representative polygonal ferrite (PF-5) and granular bainite (GB-8) grain were characterized by measuring the orientation gradient with point-to-origin measurements.

### 5.2.2 Automated phase classification and quantification

The developed Matlab® code uses the MTEX toolbox [130] to define first the grain boundaries according to the selected grain tolerance angle and afterwards calculate the KAM of each pixel. The program classifies grains as granular bainite if one pixel exceeds a misorientation of 3°; otherwise it is categorized as polygonal ferrite. Subsequently, the classification algorithm color-codes the classified grains according to their determined phase and calculates the measured granular bainite and polygonal fraction. Figure 21A displays the automatically calculated results (from two 80 × 80 µm² scanned areas) by varying the kernel sizes (100 – 600 nm) and additionally compares the differences between the grain tolerance angle of 5° and 10°. The granular bainite fraction continuously increases with increasing the kernel size and shows a transition point at 330 nm and 350 nm by using a grain tolerance angel of 5° and 10°, respectively. The transition point was identified by using a linear equation to fit the datapoints with the best R-squared factor ($R^2 = 0.99$ in all eight cases). Chen et al. [18] manually identified a constant kernel size range of 300 – 600 nm as the optimal kernel size to determine a reliable granular bainite fraction, which fits well to our detected transition points. It is assumed that the optimal kernel size will capture the information from several sub-units if it is in the range of a single sub-unit and

allows an appropriate phase classification. A kernel size being too large will cover the whole area of small ferrite grains and cause an incorrect classification [18]. This is related to a higher dislocation density near the ferrite boundaries which originates from strain accommodation of the bainitic displacive transformation [23]. The detection of a transition point could be related to a different substructure size between the investigated material and the literature results. Subsequently, the transition point was also identified as an indicator to determine the optimal kernel size and defined a kernel size of 350 nm to compare the achieved classification results. Subsequently, a granular bainite fraction of 58% and 66% was determined by applying a grain tolerance angle of 5° and 10°, respectively. A representative classification result (granular bainite = orange and polygonal ferrite = blue) and KAM map is shown for both grain tolerance criteria within Figure 21B-C (5°) and Figure 21D-E (10°). The grain boundaries are highlighted as black bold lines and the sub boundaries (2 to 5°) are displayed as blue lines. It is evident that the 10° criterion leads to a coarser grain structure in comparison to the 5° criterion. The KAM maps illustrate for both tested grain tolerance angle that grains with sub boundaries contain localized misorientations next to the sub grain boundaries and in general a higher, non-uniform misorientation distribution over the residual grain area. Those grains were mainly classified as granular bainite by applying the 5° and 10° criteria. However, applying both grain tolerance angle lead to differences of the granular bainite fraction 8%. In order to clarify the reason which leads to the different classification result, correlative ECCI investigations were conducted.
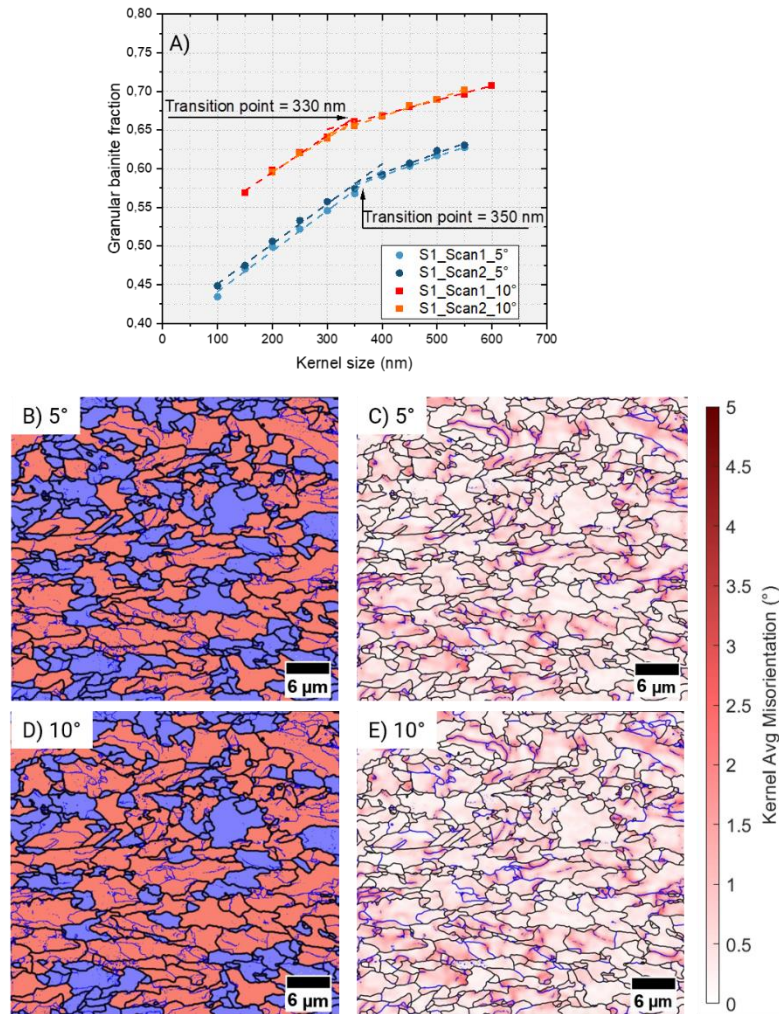
Figure 21: A) Granular bainite fraction vs. kernel size by using a grain tolerance angle of 5° (blue data) and 10° (red data), respectively. A transition point at 350 nm and 330 nm was determined by fitting a linear equation to achieve the best R-squared factor. B) and C) show a representative classification result and KAM map for the 5° criteria and D) and E) represents the result of the 10° criteria. Grain boundaries are highlighted as black bold lines and sub boundaries as blue lines. Granular bainite is colored orange and polygonal ferrite blue.

### 5.2.3    Correlative ECCI investigations

Correlative point-to-origin measurements were conducted to determine the orientation gradient within grains which were differently classified by using the automated Matlab® code and a grain tolerance angle of 5° and 10°. In contrast to Chen et al. [18], the point-to-origin measurements were not performed over sub-grain boundaries to classify both constituents. The reason is that thermomechanical treated steels may contain ferrite grains which are subdivided by sub-grain boundaries [50,170]. A representative result (grain PF-7) of the point-to-origin measurements and its KAM map as well as ECCI image is shown in Figure 22. In this example, the application of a grain tolerance angle of 5° and 10° led to a different classification of polygonal ferrite and granular bainite, respectively. This is related to the different grain shape as a result of the different grain tolerance angle and is illustrated by the KAM map (Figure 22A-B); the small grain boundary part which changes from a sub-boundary (at 10°) to a grain boundary (at 5°) is indicated by the violet arrow in Figure 22B. The three point-to-origin

measurements were carried out within the selected grain as shown by the black, red and green arrow in Figure 22A, and reveals an orientation gradient below 3° for all three measurements (Figure 22D). Additionally, the ECCI image (Figure 22C) shows that PF-7 has a nearly homogeneous contrast overall the grain area (red dashed line according to a 5° grain tolerance angle) and does not contain any substructure. Therefore, the additional investigations indicate that the selected grain belongs to the polygonal ferrite phase and thus, the application of a grain tolerance angle of 5° reveals a refined and more accurate phase fraction compared to the 10° criterion. This is in accordance with a previous study which sustained that the determined grain tolerance angle of 5° leads to a phase classification which correlates with the mechanical properties [88]. Finally, the investigated HSLA steel consists of 56% granular bainite and 44% of polygonal ferrite according to the automated phase classification system by using a grain tolerance angle of 5°. Previous investigations [3,18,37] have been dealing with similar compositions and revealed comparable phase fractions; however, one should note that the phase fraction also strongly depends on the applied cooling rate, the production parameters and chemical composition.

The performed nanoindentation tests (Figure 19C) did not allow a clear separation of both constituents according to the average mechanical properties. This could be related to the impact of the substructure within the granular bainite grains [7,148,149]. Consequently, further ECCI investigations on different polygonal ferrite and granular bainite grains were conducted to reveal the influencing aspects which caused the overlapping mechanical properties, which is presented below.
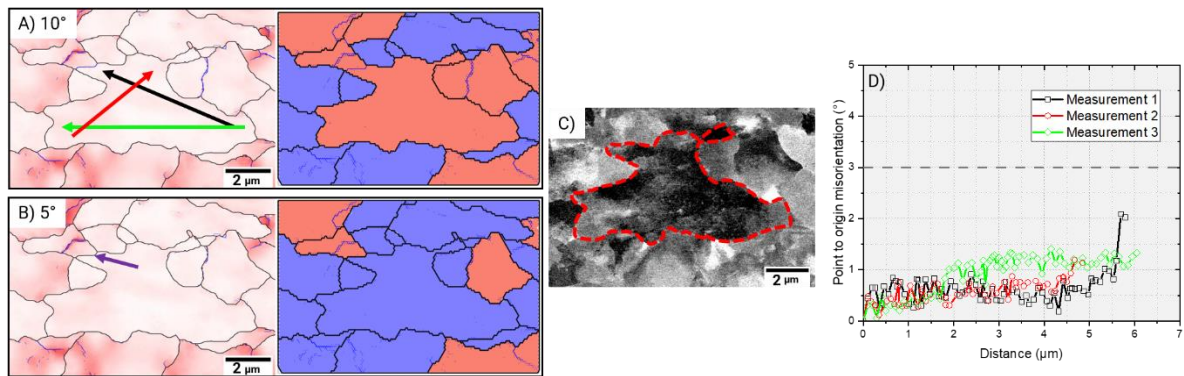


Figure 22: Representative result of the additional point-to-origin measurements. The KAM map illustrates the different grain shape by using a grain tolerance angle of 10° A) and 5° B) which led to a classification as granular bainite (orange) and polygonal ferrite (blue). The violet arrow in B) highlights the small grain boundary part which changes from a sub-boundary (at 10°) to a grain boundary (at 5°); grain boundaries are highlighted as black and sub-boundaries as blues lines. The ECCI image of the representative grain is shown in C) and reveals no substructure inside (the red dashed line shows the grain boundary according to a 5° grain tolerance angle). All three point-to-origin measurements D) (as indicated by the black, red and green arrow in A)) classified the selected grain as polygonal ferrite due to an orientation gradient < 3°.

### 5.2.4 Mechanical properties of four different grain categories

By comparing the substructures in the ECCI images with the classification map, four grain categories can be classified. This is illustrated by four examples shown in Figure 23. The grain boundaries (5°) are displayed as red dashed lines within the ECCI images and the green triangle indicates the approximate position of a nanoindent which was made after imaging. The first category represents grains which were

classified as polygonal ferrite by both grain tolerance angle criteria and does not show any evidence of substructures in the ECCI image (Figure 23A-C). From nanoindentation, a hardness value of 2.4 GPa was determined for this polygonal ferrite grain.

The algorithm, however, assigns different classification results in the second group (Figure 23D-F). Indeed, grain PF-1 contains also an internal strain like the second category and leads to a discontinuous ECCI contrast from the top to the bottom region of the grain. By further tilting of the sample, it is confirmed that the contrast continuously changed and no substructure could be identified. In terms of hardness, PF-1 has a value of 2.6 GPa and is comparable to granular bainite grains with a coarse substructure (third category). Consequently, the second category comprises polygonal ferrite grains which contain a large internal strain which may result in a higher hardness approaching granular bainite. Therefore, the internal strain inside polygonal ferrite leads to a classification failure of 8% by using a grain tolerance angle of 10° (see Figure 21A). The internal strain in such cases can affect the whole grain area but can be also concentrated within a small part of the grain. A possible reason that leads to the strain gradient inside some polygonal ferrite grains could be the onset of a displacive granular bainite transformation or an inhomogeneous deformation during the rolling process [7,23,50].

In contrast to the second category, a subset of ECCI images exhibited grains with a coarser substructure and a smaller internal distortion as shown in Figure 23G-I. Such grains were identified as granular bainite by both grain tolerance angles and represents the third category due to a hardness of 2.7 GPa. Comparable to the third category, the fourth category contains grains which are identified as granular bainite for grain tolerance angles of both 5° and 10° (Figure 23J-L). This category is characterized by a fine substructure separated by sub-boundaries. Additionally, those grains show in the ECCI image (Figure 23J) an inhomogeneous contrast due to a large internal distortion. In contrast to Figure 23G-I, the granular bainite grain GB-2 with the finer substructure reached a hardness of 3.2 GPa.

In general, it has been shown that the displacive transformation subdivides the prior austenite grain into packets which are separated into blocks and again into small bainite laths [23,171]. The lower cooling, which has to be used to form granular bainite instead of upper or lower bainite, forms a substructure with a misorientation distribution of 2 to 15° [48]. Due to the high angular resolution of the backscatter detector (0.28 – 0.57°), it is possible to resolve the granular bainite substructure [152]. As the ECCI images in Figure 23G and J show, the granular bainite substructure size is not equal between the two representative grains and leads to a lower hardness in the case of a coarser substructure. It has been found that the effective lath size is proportional to the mechanical properties of the granular bainite grain [88]. Consequently, the smaller substructure of the fourth category leads to higher hardness values compared to the third category. A changing substructure size partly be caused due to a different prior austenite grain size, whereas smaller austenite grains causing a smaller substructure [172]. In addition, the substructure size also changes during the continuous cooling process; the higher the transformation

temperature, the coarser the substructure size. In contrast to the nanoindentation tests, the automated classification system was able to identify both categories as granular bainite (with the 5° and 10° grain tolerance angle).

Hence, the same average hardness summarized in Table 4 were achieved due to the different categories of each constituent with minor differences in terms of mechanical properties. Thus, it is crucial to consider the different grain categories to achieve an average hardness of each constituent, since the determined categories are not strictly separated. This means that the mechanical properties of the individual categories overlap due to a continuous transition of the granular bainite substructure and orientation gradient within polygonal ferrite grains. Therefore, it is challenging to characterize both constituents by using nanoindentation tests only. Consequently, the correlative investigation between EBSD and ECCI revealed that the application of a grain tolerance angle of 5° is able to more accurately separate grains and achieved the best coincidence.
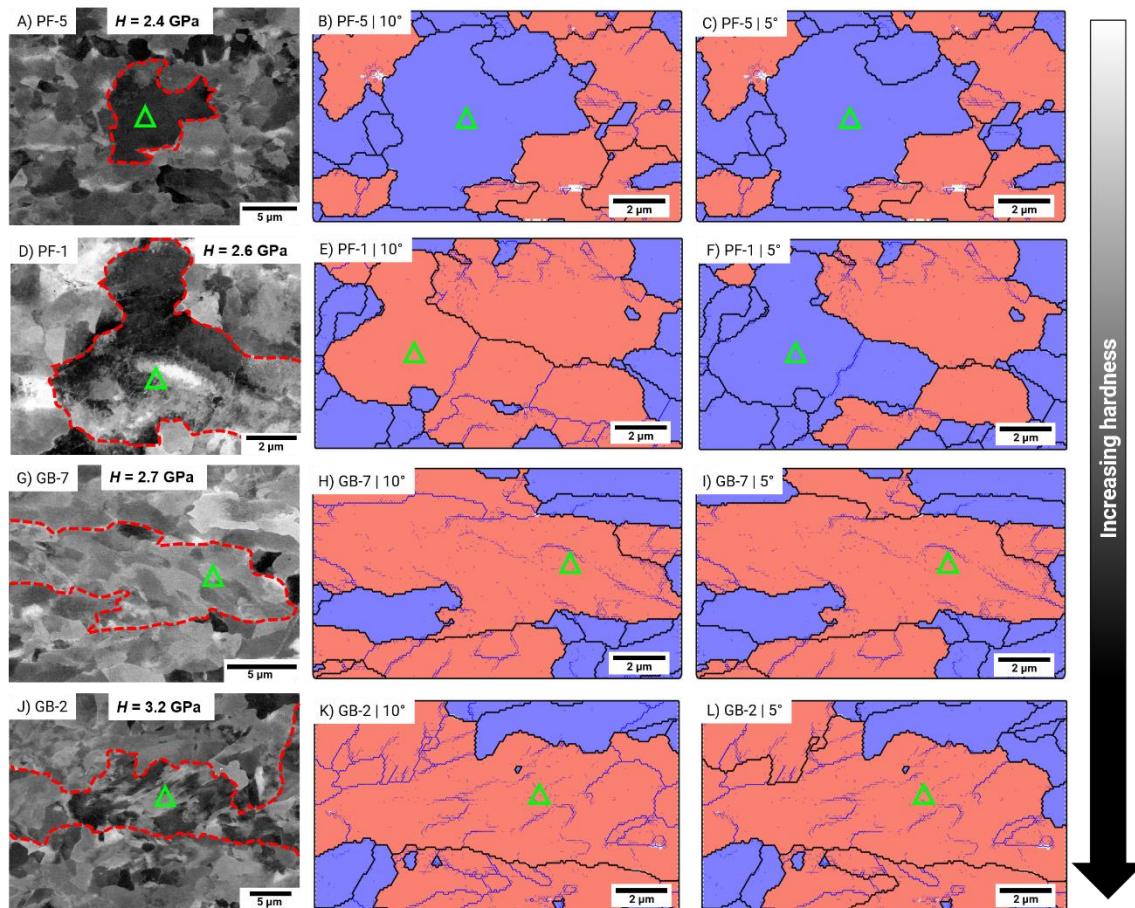


Figure 23: Four representative grains of each category are illustrated by their ECCI image (A, D, G, J). The red dashed line within the ECCI images represent the grain boundary (5°). Those grains were classified by using the automated phase classification system and a grain tolerance angle of 10° (B, E, H, K) and 5° (C, F, I, L). The used grain tolerance angle is given within the EBSD classification result; grain- and sub-boundaries are displayed as black and blue lines, respectively. The green triangle within all images illustrate the approximate indent position.

### 5.2.5 Influencing aspects

It has been observed that the point-to-origin measurement can reveal a misleading identification within grains of the second category. Figure 24A illustrates the position/direction of two point-to-origin measurements within PF-1 (second category) and exhibits a misorientation below 3° according to the first measurement (PF-1 Line 1 in Figure 24C). The second measurement (PF-1 Line 2) contradicts to the first result and reveals an orientation gradient above 3°. According to the ECCI investigations, PF-1 was classified as polygonal ferrite since a substructure was not revealed by continuously tilting of the sample (see Figure 23D). In comparison to the second category, granular bainite grains of the third and fourth categories showed a misorientation above 3° irrespective of the measurement direction/position as displayed by the three measurements in Figure 24B-C. Therefore, the orientation gradient within polygonal ferrite grains aggravates the phase classification and highlights the difficulties to distinguish polygonal ferrite from granular bainite according to point-to-origin measurements. Thus, the automated KAM classification system offers an improved phase classification, since it was shown that an orientation gradient within polygonal ferrite grains can affect the phase differentiation by point-to-origin. Hence, several point-to-origin measurements would be required to reduce this impact if they were to be performed.
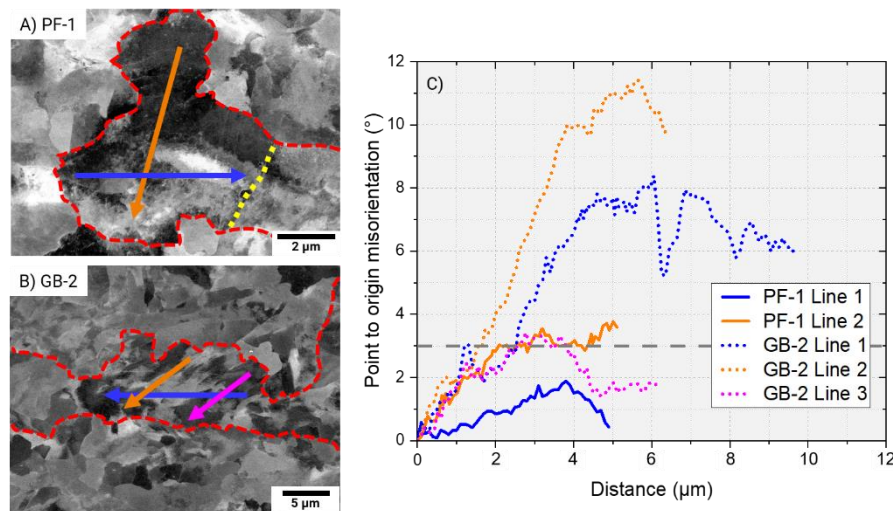


Figure 24: ECCI image of PF-1 A) and GB-2 B) where the arrows indicate the position and direction of the point-to-origin measurement (blue, orange and magenta). The grain boundary (grain tolerance angle 5°) is indicated as red dashed line and the sub-boundary in A) as yellow dotted line. The results of the point-to-origin measurement is shown in C).

As already described, granular bainite consists of irregular ferrite and a carbon rich second phase as degenerated pearlite or martensite retained austenite [5]. The LOM images in Figure 18A revealed that the studied material contained both constituents which were not separately classified by the automated classification system. The carbon rich second phase has not been separately considered, since these particles are located next to grain boundaries and possess a comparable image quality to pixels within granular bainite grains [173]. Thus, grains connected with parts of the carbon rich second phase may be

classified as granular bainite and tend to increase the granular bainite fraction. This is related to the lattice distortion of the carbon rich constituents and can cause a KAM value above 3° [174].

Another aspect that should not be neglected which influences the automated classification is the strain accumulation towards sub-boundaries. It has been frequently observed that deformed materials exhibit a strain localization and consequently higher KAM values in the vicinity of sub-boundaries [175–177]. Wright et al. [178] demonstrated that this has not only be attributed to the pile-up of dislocations but also to a loss of diffraction pattern precision, since the diffraction volume contains the lattice information of both grains when the electron beam is placed near or on the boundary. Therefore, care has to be taken when a strain localization is measured near grain boundaries by EBSD but the ECCI analysis does not resolve a substructure within the residual grain. So far, this aspect has not been considered for the automated classification system and further investigations are needed.

## 5.3   Conclusions

In this study, different techniques were used to qualify and quantify the phase fractions of granular bainite and polygonal ferrite in an HSLA steel and determine their benefits and limitations. More specifically, we adopted all structural (EBSD-KAM), mechanical (nanoindentation) and chemical investigations (ToF-SIMS) approaches correlatively on the same investigated regions. The Matlab® toolbox MTEX has been utilized to develop an automated classification system using a KAM threshold of 3° to separate both constituents. For the first time, the revealed results were validated by electron channeling contrast imaging (ECCI) studies and compared with the performed nanoindentation tests. It has been shown that the automated classification system is able to achieve a reliable classification and agrees with the ECCI investigations. An optimal kernel size of 350 nm and a grain tolerance angle of 5° was determined to achieve the best phase separation. By correlative EBSD and ECCI investigations, the microstructures can be subdivided into two main and four sub categories, which themselves correlate well with nanoindentation responses. The first category is purely polygonal ferrite grains with a homogeneous channeling contrast over the entire grain area, and the nanohardness is about 2.4 GPa. The second category is more ambiguous; although regarded as polygonal ferrite grains (based on in-depth observation using ECCI), an existing internal strain (gradient) and a similar hardness level as granular bainite grains of the third category lead to a mis-classification as bainitic phases. This is further compounded by the inability of ToF-SIMS to resolve the minute chemical differences between phases. The third and fourth categories feature granular bainite grains yet with different substructure sizes, and the detected hardness were 2.7 GPa and 3.2 GPa, respectively. Due to the continuous transition between all four grain categories and the orientation gradient within polygonal ferrite grains of the second category, the phase classification by nanoindentation was impeded. The differences between the four categories are correlated to substructure size and the effective grain size determining the mechanical properties and agrees well with previous investigations. Finally, a phase fraction of 56% granular bainite and 44% polygonal ferrite was calculated according to the automated phase classification system. While

this is a big step forward in discriminating similar phases in steels, complex multiphase steels still need further research on automated phase classification to allow reliable phase discrimination beyond experts' evaluation of LOM and SEM images.

# 6 Local strength of bainitic and ferritic HSLA steel constituents understood using correlative electron microscopy and microcompression testing[3]

## 6.1 Introduction

High-strength low-alloy (HSLA) steels contain a complex microstructure. They are frequently used for pipelines or construction due to their technical and mechanical properties [5,6,8,9]. This type of steel typically consists of various types of body-centered cubic (BCC) structures (polygonal ferrite, bainite) and residual martensite-austenite as well as a carbon rich second phase (cementite or carbide precipitates) [9,13,45,159]. Previous studies frequently proved that the combination between polygonal ferrite and granular bainite eventuates in a good combination of strength and ductility [3,19,89]. Granular bainite is defined as a mixture of irregular ferrite with carbon rich particles distributed between the irregular ferrite grains [5,51]. Irregular ferrite is also referred to as bainitic ferrite and consists of ferrite sheaves according to high resolution transmission electron microscopy (TEM) investigations [12,25]. The sub-grains are separated by low angle boundaries [23,45]. A thin carbide or austenite film can sometimes occur depending on the chemical composition [23,45]. Steel grades with a low carbon concentration are typically associated with a bainite phase transformation with the absence of carbides, retained austenite or martensite between the sub-grains [45]. For a better separation of the two phases[4], in the following, the term granular bainite refers exclusively to the irregular ferrite. In order to adapt the mechanical properties to the desired requirements in the most cost-effective way, crystal plasticity models are becoming increasingly important to investigate the correlation between microstructure and mechanical properties of the bulk material [66,179,180]. The critical resolved shear stress (CRSS) of the activated slip systems is one of the main input variables for crystal plasticity models to simulate the mechanical bulk behavior.

Micropillar compression is a specialized technique allowing for the CRSS of the individual constituents to be ascertained. For instance, the constituents of a dual phase (DP) steel, namely polygonal ferrite and martensite, have been characterized in terms of their CRSS and activated slip systems by previous investigations [32,34,66]. Through these experiments, it was shown that all three possible BCC slip systems – {110}, {112} and {123} – were activated within ferrite grains at the same CRSS while pillars containing martensite islands were characterized by a uniform deformation with a much higher strength level [32,66,181]. The higher strength and the uniform deformation of martensite are both related to the

---

[3] R.M. Jentner, S. Scholl, K. Srivastava, J.P. Best, C. Kirchlechner, G. Dehm, Local Strength of Bainitic and Ferritic HSLA Steel Constituents Understood Using Correlative Electron Microscopy and Micro-compression Testing, SSRN Electronic Journal. (2023). https://doi.org/10.2139/ssrn.4408322.

[4] We are referring to the constituents "polygonal ferrite" and "granular bainite" as phases and define their phase fraction, even though they are consisting of more than one phase each.

hierarchical martensite substructure consisting of packets, blocks, sub-blocks and laths up to a size of several nanometers [181,182]. As a result, the experimental findings from pillar compression tests contributed to the fact that crystal plasticity models are now able to simulate the macroscopic behavior of DP steels [180,183]. Despite the fact that HSLA steels constitute approximately 12% of the world steel production [40], a valid micromechanical characterization of the contributing phases is still missing.

Since the combination between polygonal ferrite and granular bainite offers a good combination of strength and ductility, several constructions as e.g. pipelines contain these constituents [9]. It is supposed that granular bainite can only be formed during the continuous cooling process and is accompanied by the onset of a displacive transformation but the carbon atoms are still able to diffuse [3,23]. TEM investigations revealed that irregular ferrite grains are subdivided by laths or equiaxed-large grains depending on the applied cooling rate due to displacive transformation [3,7,37]. Thus, the reduced effective grain size impedes dislocation movement by sub-grain and grain boundaries [41,88,89]. Beside Hall-Petch strengthening, Taylor hardening and precipitation strengthening are considered as the other mechanisms contributing to the strength [3,9,41,81,184]. Precipitation strengthening usually depends on the volume fraction and size distribution of carbo-nitrides, since they also act as obstacles to the dislocation movement and can be explained by the Orowan-Ashby mechanism [80]. Digital image analyses on TEM images were carried out to ascertain the precipitate size distribution and volume fraction, where correlative mechanical experiments were performed and showed that the nanoparticles contributed significantly to the mechanical strength [81,184]. Beside nanoparticles, retained martensite-austenite constituents have been mentioned to contribute the mechanical strength behavior [185]. The dislocation density strengthening (Taylor hardening) is one further important mechanism having a significant impact on the properties [9,41,81,184]. Depending on the cooling rate and the formation temperature, different dislocation densities can be produced within the constituents [41]. A previous study revealed by TEM investigations that at low cooling rates more dislocation walls are flattened due to cross-slip of screw dislocations [7]. This promoted a high amount of recovered and polygonised dislocations as well as the formation of small sub-grain and grain boundaries. Consequently, the higher dislocation densities contained within the individual constituents, increases the resistance to dislocation glide on the activated slip systems.

Due to the large morphological variety and complexity of low-carbon HSLA steels [5], it still remains an open task to micromechanically characterize the complex constituents of HSLA steels. Micropillar compression is a suitable technique to measure the CRSS and the activated slip system at the meso-scale [32]. Thus, the aim of this study was to identify the microscopic strength differences and their origin caused by varying the cooling rate in two HSLA steels. The carbon rich second phase, retained martensite-austenite particles as well as carbo-nitrides were not separately tested by micromechanically experiments. In total, two bulk samples with the same chemical composition but two different cooling

rates were characterized. The application of a different cooling rate resulted in a different macroscopic strength behavior which could not be explained by traditional microstructural investigations. Moreover, electron backscatter diffraction (EBSD) and electron channeling contrast imaging (ECCI) investigations were conducted to achieve detailed information about the grain and sub-grain size as well as the dislocation density of polygonal and irregular ferrite grains. It was shown that activation of dislocation slip predominantly follows Schmid's law. The CRSS values of both tested constituents were increased by using a higher cooling rate.

## 6.2 Results

### 6.2.1 Characterization of constituents and bulk mechanical properties

First microstructural characterization has been done by LOM as shown in Figure 25A-B. S1 and S2 consist of a complex mixture of polygonal ferrite and granular bainite grains (bright etched) elongated along the rolling direction with small parts of retained austenite/martensite and degenerated perlite (dark etched). EBSD measurements were conducted to assess the grain size of both samples. By fitting the grain size distribution of both samples with a log-normal function, an average grain size of $(4.7 \pm 0.6)$ µm and $(4.2 \pm 0.6)$ µm of S1 and S2 was calculated. Macroscopic tensile tests were performed to obtain the yield strength at 2% strain ($YS_{P2\%}$), ultimate tensile strength (UTS) and ultimate elongation of both samples (see Figure 25C, Table 5). The higher cooling rate of S2 caused a higher YS and UTS but a smaller ultimate elongation.
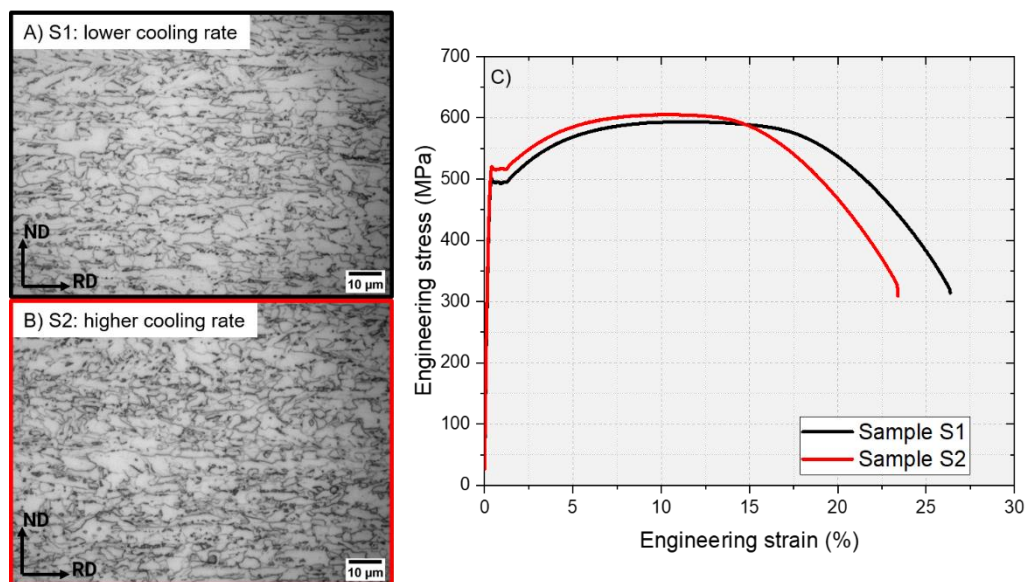
Figure 25: The LOM images A) and B) illustrate the microstructure of S1 (lower cooling rate) and S2 (higher cooling rate), respectively. C) The engineering stress and strain curve of S1 (lower cooling rate) and S2 (higher cooling rate) was received by testing along the transverse direction of the rolled plate (RD: rolling direction).

Table 5: Summary of the tensile test results and grain size of S1 and S2 measured by EBSD. The tensile tests were utilized by the material supplier along the transverse direction at room temperature. (YS$_{P2\%}$ = yield strength at 2% strain, UTS = ultimate tensile strength)

| Sample | YS$_{P2\%}$ | UTS | Ultimate elongation | Grain size (±error) | Cooling rate |
|---|---|---|---|---|---|
| S1 | 524 MPa | 593 MPa | 26% | 4.7 ± 0.6 µm | low |
| S2 | 544 MPa | 605 MPa | 23% | 4.2 ± 0.6 µm | high |

### 6.2.2 Dislocation density analyses of constituent phases

ECCI investigations were conducted to characterize the dislocation density of individual constituents. As described in Section 3.4.2, point-to-origin measurements were used to determine the phase of the selected grains, which were subsequently analyzed. For this purpose, all dislocations intersecting the image surface were counted and divided by the analyzed area ($1 \times 1$ µm²). Figure 26A-D shows the EBSD-KAM map of a polygonal ferrite and granular bainite grain of S1 and S2, respectively. In addition, the green (polygonal ferrite example) and blue (granular bainite example) rectangles within in the KAM map denote the region of the ECCI image. A total of twelve ECCI images of different grains for each phase were analyzed to determine the average dislocation density. The orange square within the ECCI image exemplifies the analyzed $1 \times 1$ µm² region and all the dislocation intersections are highlighted by red dots.
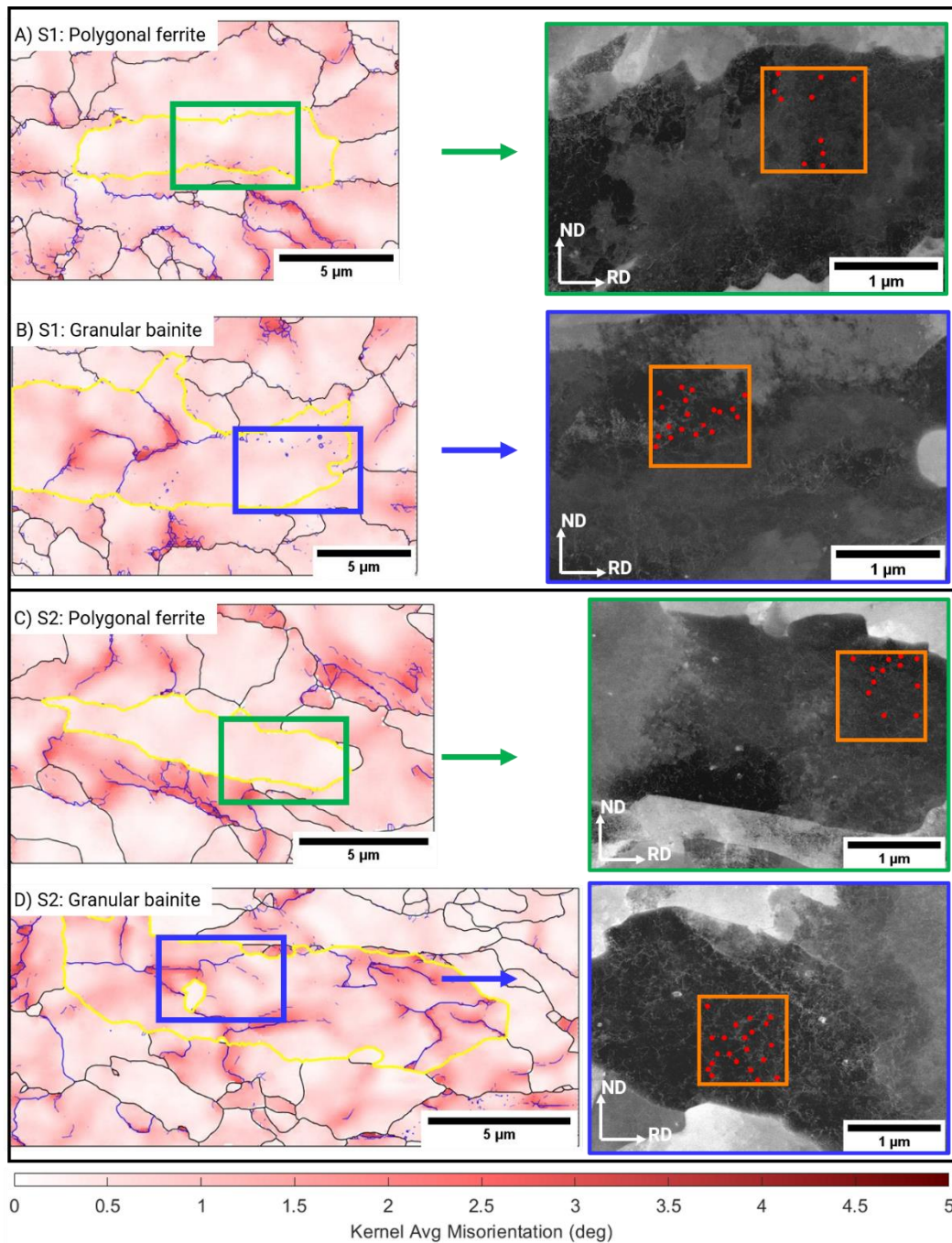
Figure 26: A), B) and C), D) shows the EBSD-KAM map and the ECCI image of a polygonal ferrite and granular bainite grain from S1 (lower cooling rate) and S2 (higher cooling rate), respectively. The orange square within the ECCI image exemplifies the analyzed $1 \times 1$ µm² region and all the dislocation intersections are highlighted by a red dot.

The ECCI images showed in general entanglements and elongated loops which are typical features of a dislocation network within a deformed material [186]. According to the applied method, a granular bainite and polygonal ferrite dislocation density of S1 and S2 was calculated; the achieved results are summarized in Figure 27. The sample S2 with the higher cooling rate revealed a granular bainite and polygonal ferrite dislocation density of $(7.1 \pm 0.7) \times 10^{13}$ m$^{-2}$ and $(2.8 \pm 0.3) \times 10^{13}$ m$^{-2}$. In comparison, S1 with the lower cooling cate utilized a granular bainite and polygonal ferrite dislocation density of $(2.1 \pm 0.9) \times 10^{13}$ m$^{-2}$ and $(0.9 \pm 0.1) \times 10^{13}$ m$^{-2}$. This implies that the constituents of S2 contain a higher

dislocation density compared to S1. Beside the dislocation density, the grain and substructure size contribute to the mechanical properties of a bulk material. Thus, further EBSD and ECCI investigations were conducted to characterize this component.
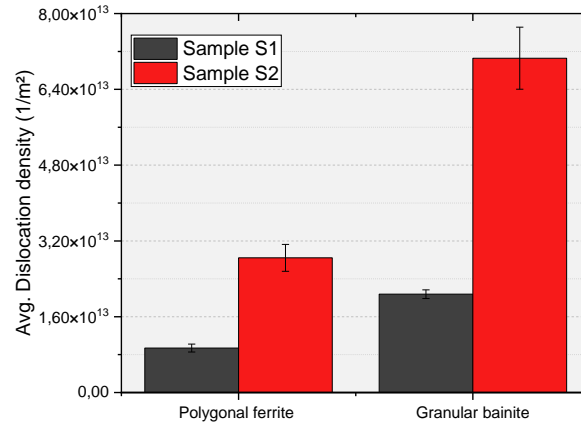


Figure 27: The average dislocation density is shown for S1 and S2 and each constituent. The average value and its corresponding average error was obtained by measuring 12 independent positions with an area of $1 \times 1$ µm².

### 6.2.3    Grain and substructure size

In general, the grain size strengthening by Hall-Petch is well known as an important factor contributing to the mechanical strength of the bulk material [86,87]. The substructure size is another intrinsic component that determines the strength of martensite and bainite [4]. Thus, systematic investigations were conducted to determine the grain size of the granular bainite and polygonal ferrite and to estimate the granular bainite substructure size. Firstly, the grain size of granular bainite and polygonal ferrite was determined by the described EBSD-KAM classification system within Section 3.4.1. Subsequently, several grains identified as granular bainite were analyzed for substructure size by conducting ECCI investigations. To achieve a first estimate about the substructure size, 60 individual measurements on each sample were conducted on several granular bainite grains. Figure 28A shows that the polygonal ferrite grain size is equivalent for S1 $(2.3 \pm 0.03)$ µm and S2 $(2.4 \pm 0.03)$ µm, while the grain size of granular bainite is smaller in case of S1 $(9.5 \pm 0.56)$ µm compared to S2 $(11.2 \pm 0.95)$ µm. In addition, it can be seen that the ECCI investigations revealed a substructure size of $(2.9 \pm 0.15)$ µm and $(1.9 \pm 0.10)$ µm in case of S1 and S2, respectively. Figure 28B-C further illustrates this with two representative images of two granular bainite grains taken from S1 and S2. The grain area of both grains is highlighted by a dashed orange (S1) and blue (S2) line. The changing contrast between the sub-blocks indicates that the higher cooling rate led to a smaller substructure size compared to S1. The result from the ECCI investigations are comparable to the reported results elsewhere [3,187,188]. Consequently, the application of a higher cooling rate led to a constant polygonal ferrite size. The granular bainite

grains were coarser whereas the substructure size decreased by utilizing a higher cooling rate and agrees with the literature.
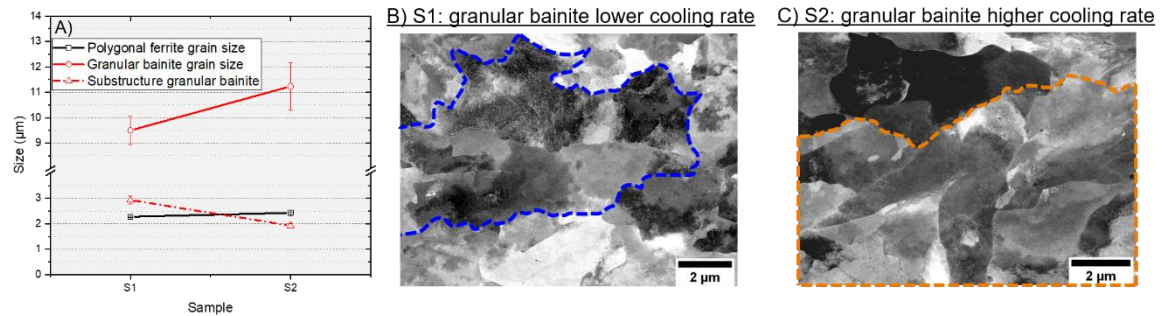


Figure 28: A) The granular bainite and polygonal ferrite grain size was calculated based on EBSD files. ECCI investigations were conducted to reveal the granular bainite substructure size by 60 manual measurements. The error bars indicating the corresponding average error. B) and C) Two representative examples of the granular bainite substructure. The area which belongs to the selected grain is indicated by a blue (S1) and orange (S2) dashed line. The grains were defined by a grain tolerance angle of 5°.

### 6.2.4  Pillar compression tests

Micropillar compression tests were performed to determine the CRSS of granular bainite and polygonal ferrite. Subsequently, the engineering stress and engineering strain was calculated using the center diameter and the height of the pillar. Figure 29A-D illustrates a representative engineering stress and strain curve for each constituent of samples S1 and S2. The polygonal ferrite curves are displayed by bold line whereas the granular bainite is displayed by a dashed line. The color is referred to the activated slip system and shows in all cases a typical intermittent flow which has been commonly observed in the used pillar size regime [31,32]. The pillar compression tests revealed that all three slip systems were activated within the polygonal ferrite grains. Only two of them were activated by performing pillar compression tests in the granular bainite constituent. It is also evident from Figure 29A-D that the granular bainite revealed a higher engineering stress level in both samples compared to the tested polygonal ferrite grains. The CRSS was calculated based on the engineering stress at 2% strain $\sigma_{2\%}$ and the Schmid factor $m$ of the activated slip system.
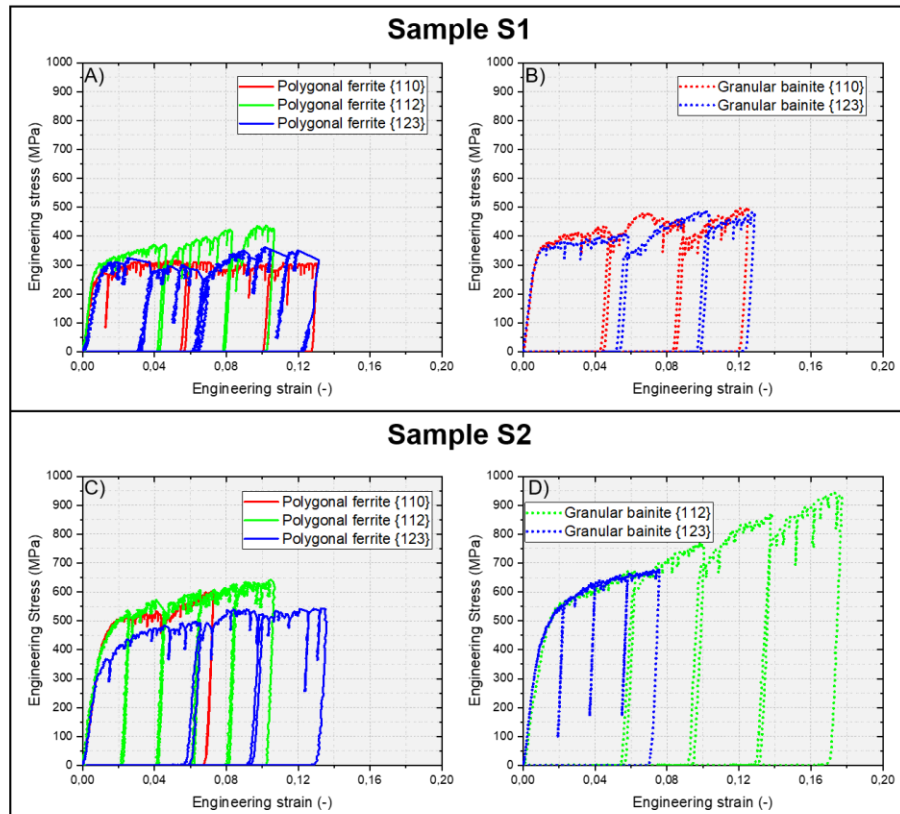
Figure 29: A) and B) shows a representative example for polygonal ferrite and granular bainite of S1. C) and D) indicates the representative example for polygonal ferrite and granular bainite of S2. The engineering stress and engineering strain curves obtained from polygonal ferrite grains are shown by bold lines whereas the granular bainite results are shown by dashed lines. The color indicates the activated slip system: {110} = red, {112} = green, {123} = blue.

Figure 30A-F shows representative pillars of S1 and S2 and the predicted slip systems according to the crystallographic orientation. All six examples illustrate that one slip system was preferentially activated until an engineering strain of 5 – 15% was reached. Subsequently, the activated slip system was identified by superimposing the predicted slip planes having the four highest Schmid factors with the *post mortem* pillar image. The corresponding values regarding the shown activated slip plane, the related Schmid factor and the calculated CRSS are shown on each SEM image. It is worth to note that not necessarily the first activated slip system had the highest Schmid factor.
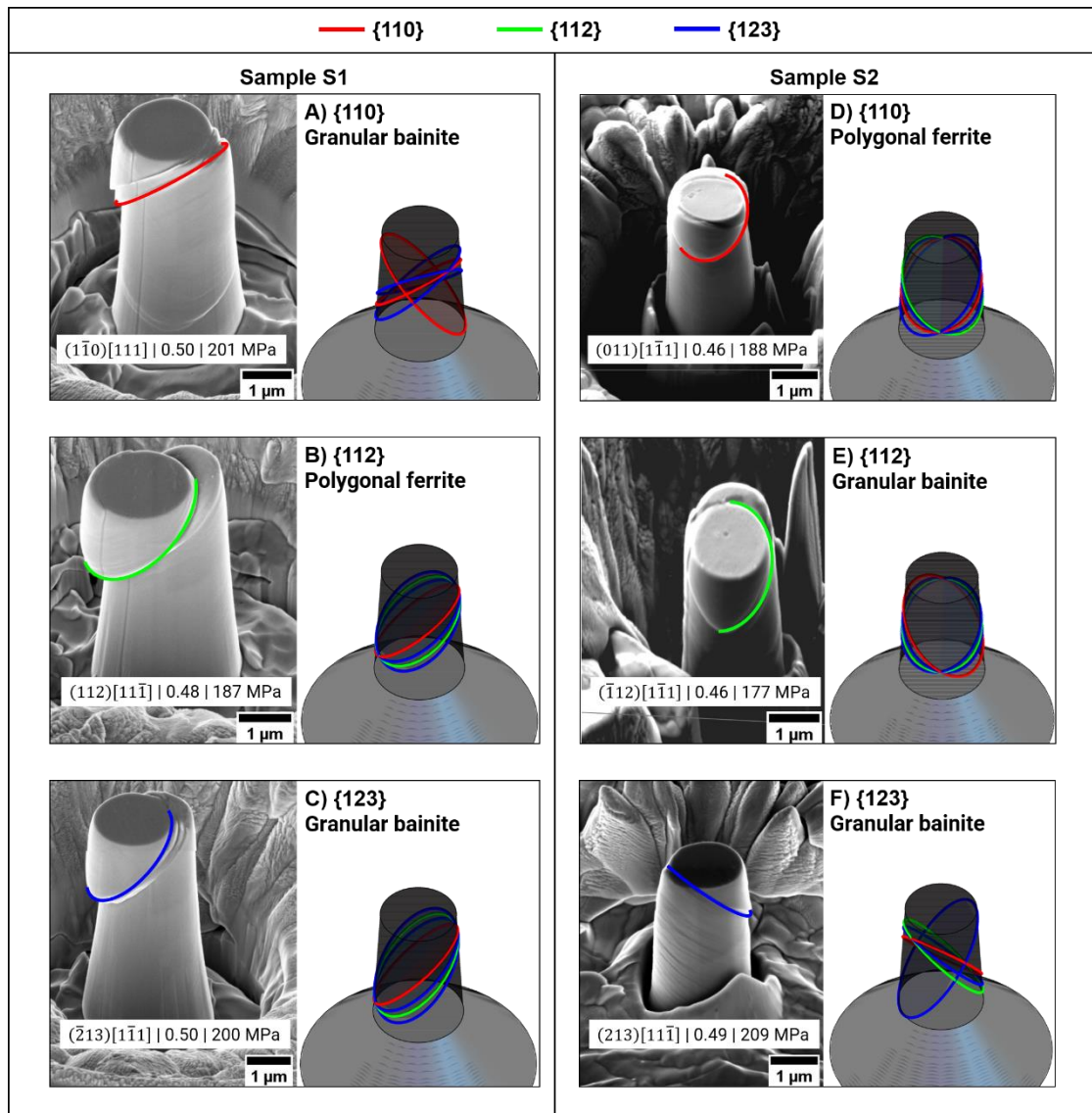
Figure 30: Slip trace analysis shown on three representative *post mortem* pillar images for S1 (column 1 A-C) and S2 (column 2 D-F). The activated slip traces of {110}, {112} and {123} of the *post mortem* images were superimposed with the predicted slip traces as shown in A), B) and C) for S1 and D), E) and F) for S2, respectively. In addition, the activated slip plane, the corresponding Schmid factor and the CRSS (based on the compressive yield strength at 2% strain) are indicated specified on each SEM image.

The average CRSS for S1 and S2 was fitted by a Gaussian distribution and plotted as a cumulative probability function seen in Figure 31A-B. In addition, the 90% and 95% confidence band intervals are displayed for each constituent. Polygonal ferrite and granular bainite of S1 reached a CRSS of $(153 \pm 4)$ MPa and $(194 \pm 6)$ MPa, respectively (see Figure 31A). Due to the higher dislocation content of S2, polygonal ferrite and granular bainite had an average CRSS of $(183 \pm 7)$ MPa and $(221 \pm 7)$ MPa. Consequently, the CRSS of both constituents increased by 16% (polygonal ferrite) and 12% (granular bainite) by applying a higher cooling rate. Moreover, the cumulative probability function of S1 shows a clear separation between both constituents whereas the CRSS of polygonal ferrite and granular bainite of S2 appeared as a smooth transition as displayed in Figure 31B. The performed experiments revealed that the average CRSS of both constituents increased by using a higher cooling rate. It is noticeable that

the difference in average CRSS between polygonal ferrite and granular bainite of the same sample and even the difference in average CRSS of polygonal ferrite and granular bainite between S1 and S2 was almost identical.

Once the CRSS of each constituent and sample was determined, the results were analyzed regarding the activated slip plane family as shown in Figure 31C-F. The pillar compression tests revealed that all three slip systems – {110}, {112} and {123} – were activated regarding polygonal ferrite at S1 and S2. On the other hand, pillar compression tests within granular bainite grains did not activate the {112} and {110} slip system on sample S1 and S2, respectively. One can further conclude that the cumulative probability function and the average CRSS of the distinct slip plane families are comparable.
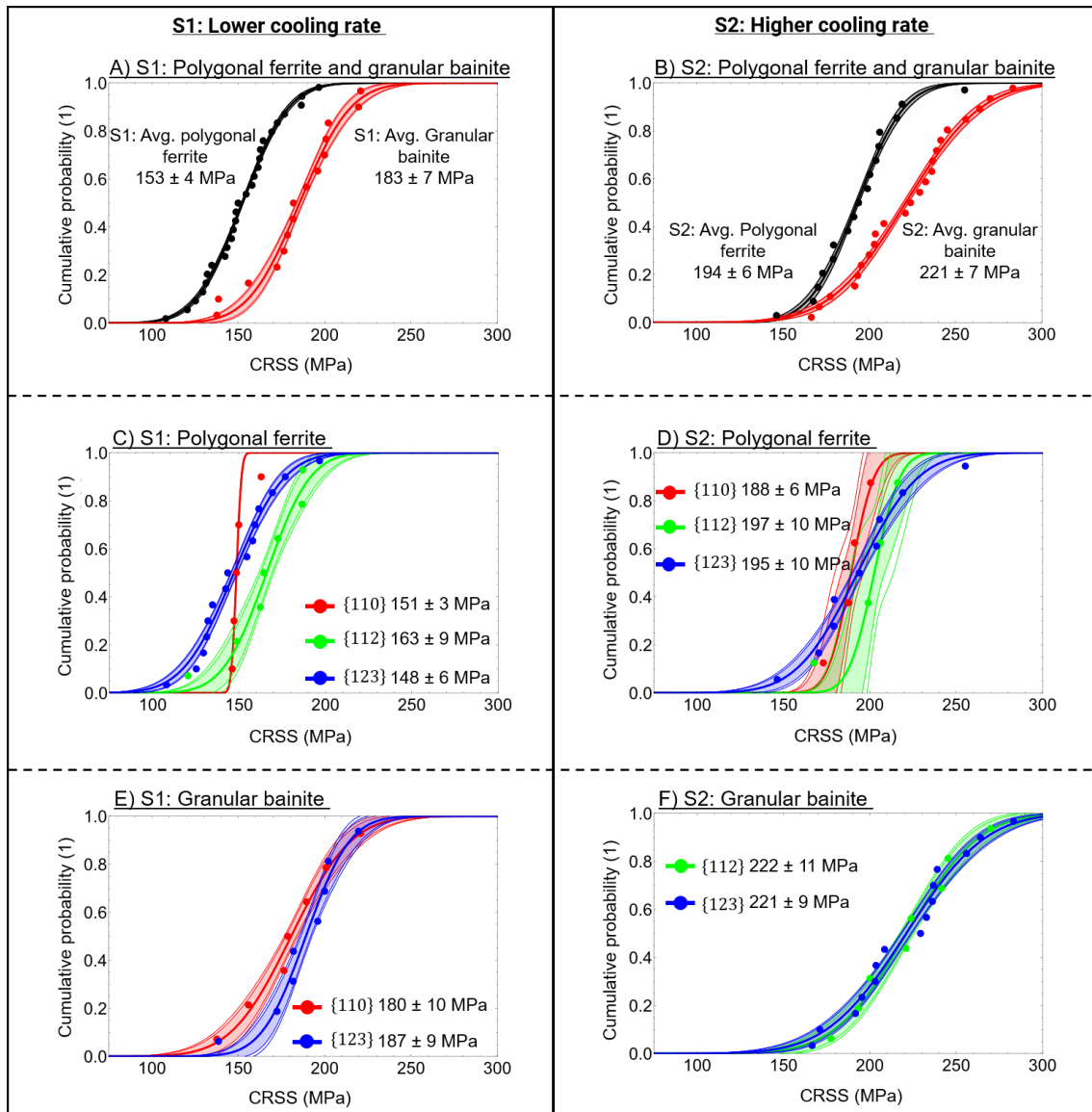


Figure 31: The average CRSS of S1 A) and S2 B) was calculated for each constituent (polygonal ferrite and granular bainite) based on the engineering stress $\sigma_{2\%}$ and plotted with the cumulative probability function. C) and D) shows the CRSS of the activated slip planes for polygonal ferrite and granular bainite of S1. E) and F) also illustrates the CRSS of polygonal ferrite and granular bainite but for S2. A Gaussian function was used to achieve the average CRSS and its error. In addition, the 90% and 95% confidence band intervals are plotted for cumulative probability curves.

In addition, Figure 32 compares the activated slip systems of S1 and S2 with the color-coded regions for each slip system according to Schmid's law assuming an identical CRSS for all slip systems. The inverse pole figure (IPF) illustrates that the majority of the tested pillar follows Schmid's law and the crystallographic orientation of the main outliers are next to the border between two different colored regions. The breakdown of Schmid's law and the stress concentration at the pillar top surface are mainly considered to be responsible for activating slip systems with a lower Schmid factor [102,189]. This will be discussed in the section below.
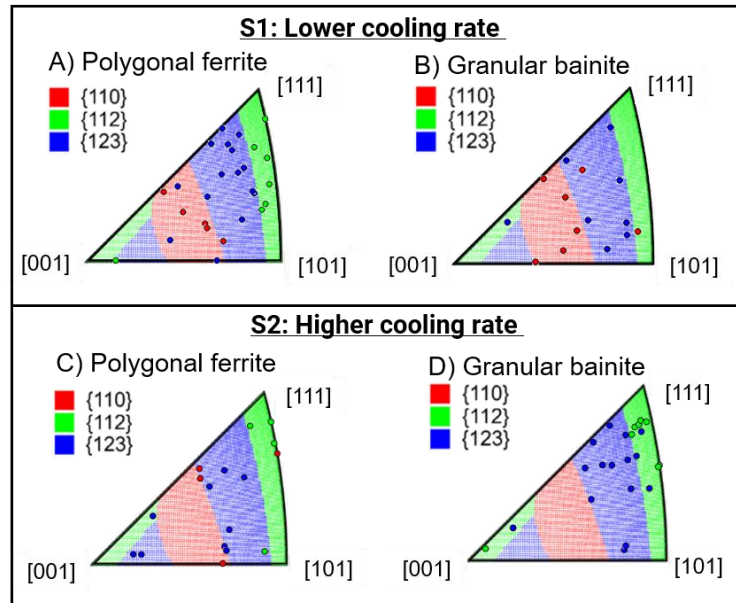


Figure 32: A) and B) represents the activated slip system during the pillar compression tests within polygonal ferrite and granular bainite grains. C) and D) also indicates the orientation of the activated slip system for S1 and its constituent's polygonal ferrite and granular bainite. The color-coded areas within each IPF exhibits the region where the {110}, {112} and {123} slip system has the highest Schmid factor by assuming the same CRSS for all slip systems.

## 6.3   Discussion

The first part of the discussion (Section 6.3.1) addresses the determination of bulk behavior through pillar compression tests within polygonal ferrite and granular bainite grains. Afterwards, Section 6.3.2 deals with the strengthening mechanism which were considered to be responsible for the higher strength level of the bulk material and the individual constituents of S1 and S2. Finally, Section 6.3.3 is dedicated to the activated slip systems by performing pillar compression tests.

### 6.3.1   Micromechanical tests compared to the bulk behavior

Tensile tests on the investigated materials indicated that the higher cooling rate of S2 resulted in a higher $YS_{P2\%}$ and UTS compared to S1 (see Figure 25D and Table 5). The performed microcompression tests revealed that the polygonal ferrite and granular bainite $CRSS$ were affected by the different cooling rate (see Figure 31A-B). In order to compare the micromechanical behavior with the tensile tests of the bulk material, the phase fractions of granular bainite $C_{GB}$ and polygonal ferrite $C_{PF}$ was determined for S1

and S2 by utilizing the EBSD-KAM classification as described in Section 3.4.1. Subsequently, the rule of mixture was used to calculate the *CRSS* of the bulk material (CRSS$_{bulk}$) by using Equation 2:

$$CRSS_{bulk} = CRSS_{PF} * C_{PF} + CRSS_{GB} * C_{GB} \ and \ C_{PF} + C_{GB} = 1 \tag{1}$$

where, CRSS$_{PF}$ and CRSS$_{GB}$ represents the CRSS of granular bainite and polygonal ferrite based on the pillar compression tests. The Taylor factor *M* correlates the YS of the polycrystalline bulk material with the CRSS$_{Bulk}$ which is calculated by Equation 3 [190,191]. Hence, the yield strength YS$_{calc.}$ of the bulk material was calculated by using Equation 4:

$$YS_{calc.} = M * CRSS_{bulk}. \tag{2}$$

A previous computer simulation considered all three possible BCC slip systems along the $\langle 111 \rangle$ direction and revealed an average Taylor factor of $M_{Avg.} = 2.733$ for compression and tension for grains of various orientations [192]. Consequently, a macroscopic yield strength YS$_{calc.}$ of 480 MPa and 572 MPa was calculated for S1 and S2, respectively. To summarize this, all experimental and calculated results are listed in Table 6.

Table 6: All experimental and calculated results are summarized to compare to mechanical behavior of the bulk material and the individual tested phases. The estimated bulk yield strength is given with its standard deviation (PF = Polygonal ferrite / GB = Granular bainite)

| Source | CRSS Pillar compression | | Tensile test bulk material | Literature [192] | EBSD | Calculated bulk yield strength |
|---|---|---|---|---|---|---|
| **Sample** | Polygonal ferrite | Granular bainite | $YS_{P2\%}$ | Taylor factor | Phase fraction | YS$_{calc.}$ |
| **S1** | $(153 \pm 4)$ MPa | $(183 \pm 7)$ MPa | 524 MPa | 2.733 | 26% / 74% PF / GB | 480 MPa $\pm$ 2% |
| **S2** | $(194 \pm 6)$ MPa | $(221 \pm 7)$ MPa | 544 MPa | | 44% / 56% PF / GB | 572 MPa $\pm$ 2% |

It is shown that YS$_{calc.}$ and YS$_{2\%}$ coincide and deviate by only 8% and 5% for S1 and S2, respectively. The deviation between YS$_{calc.}$ and YS$_{2\%}$ may be caused by the fact that single grains were tested by pillar compression tests allowing for free and unconstrained slip. This can explain the underestimation of YS$_{2\%}$ by the CRSS (see S1 in Table 6), but not the overestimation (see S2 in Table 6). A prior work has studied different ratios between wire diameter to grain size by tensile experiments [193]. This study ascertained that the yield stress of a micro-sized wire varies if the ratio is below 10. In addition to the single polygonal ferrite grains, granular bainite grains with a substructure were also tested (see Figure 28B and C). Since the performed ECCI investigations on S1 and S2 determined a granular bainite substructure size of $(2.9 \pm 0.15)$ µm and $(1.9 \pm 0.10)$ µm and a pillar diameter of 2 µm was used, it is evident that a maximum of one to three sub-grains can be contained in the pillar volume. Subsequently, the variation of the number of sub-grains in the pillar volume may contribute to the deviation between YS$_{calc.}$ and YS$_{2\%}$.

Since the pillar position can vary slightly inside the individual grains, an inhomogeneous distribution of dislocations inside the constituents will also result in a variation of dislocations inside the tested pillar volume. Thus, the small overestimation of $YS_{calc.}$ compared to $YS_{2\%}$ can also be related to a dislocation density that is slightly higher in the pillar volume compared to the average dislocation density based on the ECCI investigations.

The arrangement and shape of the individual phases relative to each other also contributes to the overall bulk behavior. It has been shown on ferritic-martensitic steels that the morphology of the constituents had a significant impact on the mechanical behavior [35,143]. Both investigations observed a higher strength and lower ductility at samples with large and equiaxed martensite particles compared to microstructures with elongated martensite islands; these results were achieved from samples with a constant composition and phase fraction. Subsequently, the relative distribution of polygonal ferrite and granular bainite grains to each other may contribute to the differences between $YS_{calc.}$ and $YS_{2\%}$. This aspect has not been considered within the EBSD-KAM classification system [122].

### 6.3.2 Strengthening mechanisms

It can be assumed that the mechanical strength of a complex microstructure can be decomposed into a number of intrinsic components [4,9]. In general, the following mechanisms are responsible for determining the mechanical strength: yield strength of pure iron, solid solution hardening, precipitation hardening, dislocation hardening, grain and sub-grain size (Hall-Petch) and a possible texture contribution [9]. The scope of this work was on characterizing the micromechanical behavior and microstructure and substructure size. Subsequently, the effect of grain and sub-grain size ("smaller is stronger") and dislocation density on the macroscopic strength are discussed.

The tensile tests of the bulk material determined a higher $YS_{P2\%}$ and UTS at material S2 by using a higher cooling rate compared to material S1 (see Figure 25C). In general, granular bainite forms by the onset of a displacive transformation and the substructure size depends on the applied cooling rate [3,23]. Previous TEM investigations demonstrated that the granular bainite substructure changes from a lath/sheaf substructure to equiaxed-large grains by varying the cooling rate from 60 – 5 K/s [7]. This agrees to the achieved results, since the performed ECCI investigations ascertained a granular bainite substructure size of $(2.9 \pm 0.15)\,\mu m$ and $(1.9 \pm 0.10)\,\mu m$ on the investigated material S1 and S2, respectively. Subsequently, the application of a higher cooling rate produced a smaller substructure separated by sub-boundaries.

The phase fraction was determined as described in Section 3.4.1 and revealed that S1 is composed of 74% granular bainite and S2 contained 56% despite the higher cooling rate of S2 (see Table 6). This agrees with the misorientation angle distribution based on the EBSD measurements (see Figure 33). The higher fraction of misorientation angles between 35 – 63° may indicate that more polygonal ferrite grains were formed despite the higher cooling rate of S2. It was recently shown that the application of

a lower cooling rate leads to the formation of a coarser substructure [7,194]. Thus, the lower cooling rate causes within the high-temperature range a flattened dislocation cell structure by pile-up or tangled dislocations and the polygonization process has more time to proceed and a coarser substructure may emerge [7]. In addition, the smaller cooling rate and subsequently higher transformation temperature reduces the density of sub-boundaries [194,195]. Indeed, the coarser granular bainite grains of S1 still include a high fraction of strain gradients which are between $3 - 5°$. This results in a higher granular bainite fraction per area compared to a microstructure which was treated by a faster continuous cooling process.
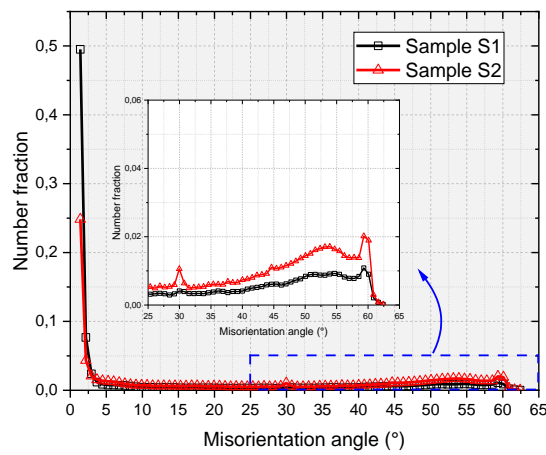


Figure 33: The average misorientation angle distribution of S1 (black data) and S2 (red data) is shown based on EBSD measurements. It is indicated that S2 contains a higher fraction of grain boundaries with a misorientation angle between $35 - 63°$.

The performed pillar compression tests revealed that the application of a higher cooling rate (in case of sample S2) led to a higher CRSS for granular bainite and polygonal ferrite (see Figure 31A and B). A previous study performed pillar compression tests on a dual-phase steel containing polygonal ferrite and martensite [32]. The same pillar size was used as in the present study and the results of both investigations coincide regarding the CRSS of polygonal ferrite. However, to the authors best knowledge, no results have been published on pillar compression associated with granular bainite.

The ECCI investigations revealed that both constituents of S2 contained a higher dislocation density compared to S1 and resulted in a higher CRSS (see Figure 27). It is also interesting to note that the polygonal ferrite of S2 had a higher dislocation density as well as a higher CRSS than the granular bainite phase of S1. A previous study revealed a granular bainite and polygonal ferrite dislocation density of $1.7 \times 10^{14}$ m$^{-2}$ and $0.37 \times 10^{14}$ m$^{-2}$ by TEM investigations, respectively [196]. More recently, Huang et al. [3] also measured a granular bainite dislocation density of $(5.4 \pm 0.9) \times 10^{14}$ m$^{-2}$. Consequently, both aforementioned studies exhibited a slightly higher dislocation density for the investigated constituents. This could be caused by utilizing a lower cooling rate.

The increased strength of S2 can be correlated to the presence of a higher dislocation density inside the activated pillar volume. Subsequently, more dislocations can move on the activated slip system with the highest Schmid factor [83]. Dislocation glide can be impeded by the interaction with other mobile or immobile dislocations and results in a higher CRSS [9]. Moreover, granular bainite grains of S2 contained a smaller substructure size than S1 (see Figure 28A). It is obvious that this contributes to the bulk strengthening as well. A former investigation determined for a low carbon steel with a fully bainitic structure that the yield stress is proportional to the inverse lath size defined with low boundary misorientation (2 – 7°) [88]. It was concluded that lath boundaries and dislocation cell boundaries acting as obstacles to the moving dislocations. This is also consistent with other studies on the strength increase due to the refinement of the granular bainite substructure size [19,81,89].

One can also recognize that the polygonal ferrite of S1 showing a lower CRSS compared to the polygonal ferrite grains of S2. Moreover, the bulk tensile test ascertained that material S1 has a lower YS compared to S2 (see Figure 25C). In a recent study [32], pillar compression tests were performed on two different ferrite-martensite steels. It was found out that the softer ferrite phase determined the onset of yielding of the bulk material [32]. This is in agreement with the current results, since S2 contained a higher $YS_{2\%}$ and polygonal ferrite dislocation density. It is assumed that the higher cooling rate of S2 introduced more dislocations inside the polygonal ferrite during the displacive transformation of the granular bainite phase [7]. Subsequently, the higher dislocation density served as obstacles and increased the CRSS to move the activated dislocations [66,81,83].

The precipitation strengthening by the formation of carbo-nitrides has been identified as a further mechanism contributing to the mechanical strength [41,81]. Since the tested material contained Nb and Ti additions, it is possible that carbo-nitrides were formed during the production process. Previous TEM investigations showed that their size varies within the nanometer range [41,81]. Thus, carbo-nitrides precipitates can be also included within the tested pillar volume. In general, precipitates nucleate and grow during the cooling process and cross different slip planes [83]. Once mobile dislocations are moving along the activated slip plane and precipitates acting as obstacles from sliding further, they must either cut through or bow out between the particles [83,197]. Additional TEM investigations were not conducted to quantify the precipitates and, thus interfere with the dislocation strengthening mechanism within the tested pillar volume.

### 6.3.3 Activated slip systems

The performed pillar compression tests utilized that all three BCC slip systems - namely {110}, {112} and {123} - were activated within polygonal ferrite grains (see Figure 31C and D). This agrees well to the observation from a previous study [32] on pillar compression tests of polygonal ferrite grains in two different DP steels. In contrast, testing granular bainite grains did not show the activation of all three slip systems for each sample. The slip systems {112} and {123} were activated by testing granular

bainite grains on S1 whereas only the {112} and {123} slip system were observed for granular bainite grains on S2 (see Figure 31E and F). It should be noted that all slip planes were identified using SEM images and are therefore limited by the resolution of a field emission microscope. It was concluded by previous TEM experiments and atomistic simulations that the occurrence of {112} and {123} slip system is caused by the cross slip of screw dislocations on {110} planes [102,198,199]. This could also explain why the CRSS for all activated slip systems of granular bainite and polygonal ferrite for each sample was nearly identical. The fact that only two out of three slip systems were activated at the granular bainite could merely be a statistical problem as only 15 and 23 pillars were tested for S1 and S2, respectively.

In addition, it can be concluded that nearly all tested pillars followed Schmid's law according to the IPF indicating the regions with the highest Schmid factor and the experimentally identified slip systems (see Figure 32). The second slip system was activated only for a few outliers when the Schmid factor of the first two was nearly identical. This is related to the limited number of dislocation sources within the confined pillar volume [189,200]. Furthermore, the smallest pillar diameter at the top caused lateral stresses during loading and could further be responsible that not the primary slip system was activated [31].

## 6.4 Summary

In the present work, two samples (S1 and S2) of an HSLA steel grade were tested with the same chemical composition but a different cooling rate was applied during the production process. This led to microstructural changes in the polygonal ferrite and granular bainite phases. Tensile tests of the bulk material revealed a high yield and tensile strength by using a higher cooling rate in case of S2. Thus, the aim of this study was to perform micropillar compression tests to characterize the micromechanical strength of the individual constituents, since it was not clarified which mechanism caused the different mechanical strength of the bulk material. Beside pillar compression tests to quantify the CRSS of the activated slip system, ECCI and EBSD investigations were conducted to elucidate the strengthening mechanism by measuring the grain-, sub-grain size and the dislocation density. The key findings of the present study are summarized by the following points:

- Pillar compression tests revealed that the CRSS of both constituents increased by using a higher cooling rate on S2. It was shown that even the polygonal ferrite of S2 utilized a higher CRSS than the granular bainite of S1. This agrees well with the measured dislocation density by ECCI investigations. Since the tested pillar volume contained only one to three sub-grains of the granular bainite substructure, it is reasonable that the higher dislocation density mainly contributed to the increasing CRSS. Nearly all compression tests followed Schmid's law. All three possible slip systems were confirmed by *post mortem* images in case of polygonal ferrite

grains. Micropillars placed within granular bainite grains showed only the activation of two slip systems.

- Consequently, both phases were strengthened by increasing the cooling rate. It is assumed that the smaller substructure size contributed beside the higher dislocation density to the increasing strength of S2.

- Based on ECCI investigations, an increasing dislocation density was measured for polygonal ferrite and granular bainite grains as well. It was concluded that this was caused by the higher cooling rate.

# 7    Summary and outlook

The present thesis focused on the phase identification and quantification as well as determining the mechanical properties of a HSLA steel which was industrial produced. In total, the experiments were conducted on two samples treated by a cooling rate below 50 K/s and varied by approx. 30%. Both samples contained a microstructure consisting of granular bainite, a mixture of irregular ferrite and a second carbon rich phase, and polygonal ferrite. Subsequently, it was assumed that the different cooling rate led to a different phase fraction and mechanical properties of both phases. Two different approaches were tested to achieve a unique phase identification and quantification. At first, grid-nanoindentation tests were performed and the obtained nanohardness and reduced Young's modulus results served as input variables for K-means clustering. The clustering result was verified by EBSD measurements. The second approach used the different orientation gradient between irregular and polygonal ferrite grains. Additionally, point-to-origin, ECCI and nanoindentation investigations on selected grains were performed to verify the achieved phase identification and quantification system. Furthermore, several micro-pillar compression tests were carried out in order to quantify the impact of the individual phases on the mechanical properties. Utilizing different cooling rates allowed to change also defect content in the phases. The tested micro-pillars were characterized regarding the activated slip system and CRSS. Further ECCI and EBSD investigations were performed with respect to dislocation density and grain- and sub-grain size to clarify where the strength differences originate. All the results obtained are summarized in the following subsections.

## 7.1    Grid-nanoindentation coupled with K-means clustering for phase identification and quantification

Nanoindentation was utilized to derive nanohardness and reduced Young's modulus from one HSLA sample with the higher cooling rate and a DP steel sample. The DP sample served as reference due to the unique mechanical properties between both constituents. Once the nanoindentation experiments were done on both samples, each dataset was pretreated to eliminate outliers. Before treating both datasets by K-means, the elbow method was used to determine the optimal number of clusters. The elbow method was able to define the optimal number of clusters regarding the DP steel with significant differences of mechanical properties between the polygonal ferrite and martensite phases. However, it was not possible to determine the optimal number of clusters in terms of the HSLA steel sample by utilizing the elbow method as the mechanical contrast of $H$ and $E_r$ was too subtle for granular bainite and polygonal ferrite. Therefore, the input variables of both samples were clustered by considering three clusters for the DP sample and two, three and four clusters for the HSLA sample. Subsequently, all clustering results were correlated with the microstructure by correlative EBSD measurements. The correlation for the DP steel showed that one cluster can be assigned to indents which are located within martensite and one for the ferrite grains. The third cluster of the DP sample was assigned to indents

which are located on grain boundaries, triple junctions or close to martensite islands but still inside polygonal ferrite. The correlative investigation between the clustering results and the EBSD measurement showed that a clear separation of the two HSLA steel phases could not be achieved by using K-Means. An average granular bainite and polygonal ferrite nanohardness of $(3.2 \pm 0.2)$ GPa and $(3.0 \pm 0.1)$ GPa was calculated based on the phase identification by EBSD, respectively. The three identified clusters of the DP sample revealed an average nanohardness of $(4.0 \pm 0.6)$ GPa, $(2.2 \pm 0.3)$ GPa and $(2.0 \pm 0.2)$ GPa. Thus, a deviation of at least 10% contained the clusters related to the DP sample, whereas granular bainite and polygonal ferrite deviated only by 6%. Consequently, it was assumed that in this case the input variables characterizing each phase have to differ at least 10% to achieve a clear phase identification by K-means. Moreover, it is concluded that a differentiation between granular bainite and polygonal ferrite by nanoindentation alone was not achieved due to the similar mechanical properties of both constituents, the impact of grain boundaries and the variation of substructure size of granular bainite grains.

## 7.2  Phase identification and quantification by using an automated system based on EBSD measurement

The performed investigations included different techniques to achieve a distinct phase identification and quantification regarding the HSLA steel. The Matlab® toolbox MTEX was used to develop an automated phase identification and quantification system based on the EBSD-KAM value. The automated KAM classification system used a threshold of 3° to differentiate polygonal ferrite and granular bainite. Once a pixel exceeded an misorientation of 3°, the related grain was classified as granular bainite, otherwise it was counted as polygonal ferrite. Only KAM values below 4.9° were considered to reduce the impact of grain boundaries, since polygonal ferrite grains may be separated by sub-grain boundaries. Initially, it was required to test which grain tolerance angle (5° or 10°) and kernel size derives the best phase separation. Therefore, the kernel size was systematically increased for both grain tolerance angle and correlative ECCI investigations performed to validate the achieved results. It has been shown that an optimal kernel size of 350 nm and a grain tolerance angle of 5° revealed the best phase separation. In addition, structural (EBSD), mechanical (nanoindentation) and chemical (ToF-SIMS) information were correlatively utilized and analyzed. The conducted ECCI and nanoindentation experiments indicated that microstructure can be subdivided into two main and four sub-categories. The two main categories were composed of polygonal ferrite and granular bainite. The first sub category included polygonal ferrite grains with a homogeneous ECCI channeling contrast across the whole grain area and a nanohardness of 2.4 GPa. Similar to the first sub-category, the second sub category included also polygonal ferrite grains but with an internal orientation gradient leading to a discontinuous channeling contrast and a nanohardness which is similar to the third category. The third category contained granular bainite grains with a coarser substructure size. Consequently, the internal strain (gradient) and the similar nanohardness between sub category two and three led to a

mis-classification by using a grain tolerance angle of 10°. This was significantly reduced by utilizing a grain tolerance angle of 5° and, thus enhanced the phase identification and quantification. The fourth sub-category also contained granular bainite grains with a smaller substructure size and consequently a higher hardness than sub-category three. The increasing nanohardness was related to the different internal strain gradient and the decreasing substructure size. However, ToF-SIMS analyses were not able to identify the different constituents due to their minute chemical differences. Based on the revealed and verified EBSD-KAM classification system, the HSLA steel is composed of 56% of granular bainite and 46% of polygonal ferrite.

## 7.3 Micromechanical properties of granular bainite and polygonal ferrite

Correlative SEM and micromechanical pillar compression tests were performed on two HSLA steel samples. Both samples were industrial produced and continuously cooled after rolling. The chemical composition was identical in both cases, but the cooling rate was in the range below 50 K/s and varied by approx. 30%. Tensile tests of the bulk material indicated that the higher cooling rate led to a higher yield and tensile strength. Subsequently, micropillar compression tests were performed within polygonal ferrite and granular bainite grains of both cooling rates. Beside analyzing the CRSS and activated slip system, the dislocation density as well as granular bainite substructure size was analyzed based on ECCI and EBSD investigations to draw conclusion on the strengthening mechanism. The pillar compression tested revealed an increased CRSS by utilizing a higher cooling rate at the continuous cooling process. It is shown that the CRSS of both constituents increased due to an increased dislocation density. The higher dislocation density originates from the reduced time within a high temperature range during continuous cooling. Thus, dislocation annihilation and cross-slip was reduced and acting as obstacles for mobile or immobile dislocations during plastic deformation. Since, the lower and higher cooling rate created a granular bainite substructure of $(2.9 \pm 0.15)\,\mu m$ and $(1.9 \pm 0.10)\,\mu m$, respectively, the pillar volume contained only one to three sub-grains and cannot represent the grain size strengthening ("smaller is stronger"). Nevertheless, it is assumed that the smaller granular bainite substructure and the increased dislocation density contributed to the increased strength of the bulk material. Moreover, the *post mortem* pillar analyzes showed that all three possible slip systems – {110}, {112}, {123} – were activated. Micropillars located within granular bainite grains only revealed the activation of two slip systems most likely due to limited statistics.

## 7.4 Outlook

The present work represents a thorough investigation on bainitic an ferritic HSLA constituents regarding phase characterization and their micromechanical properties. Nevertheless, some questions remained unsolved and will be addressed within this section.

The EBSD-KAM phase identification and quantification system has been tested on a HSLA steel containing polygonal ferrite and granular bainite. According to this, extended investigations could be

performed on different HSLA grades which were produced by different cooling rates. This would allow to asses until which cooling rate the 3° threshold identifies the constituents correctly according to correlative ECCI and nanoindentation tests.

Further studies on micromechanical properties could address the detailed dislocation motion in polygonal ferrite and granular bainite. It was shown that the increased dislocation density increased the strength of both constituents. Since only one to three granular bainite sub-grains were contained inside the pillar volume, the substructure strengthening could not be characterized by the performed pillar compression tests. Based on previous investigations, it was assumed that the reduced granular bainite substructure size due to the lower cooling rate contributed to the increased bulk toughness. It might be of interest how effective the substructure boundaries act as obstacles for dislocation motion by subsequent TEM investigations on compressed pillar cross-sections.

Since crystal plasticity contributes more and more to design new steel grades with improved mechanical properties, the achieved results could be implemented into a CP model. By creating a representative volume element for each tested HSLA, it is possible to investigate the contribution of each phase on the bulk strength. Moreover, the impact of texture and phase distribution could be addressed by conducted crystal plasticity simulations.

# 8 Appendix

Table 7: Summary of the average hardness and indentation modulus, and their standard deviation, for M2 and the number of clusters of $k = 2$, $k = 3$ and $k = 4$.

| Material | $k$ | Cluster | $H$ (GPa) | $E_r$ (GPa) | Datapoints |
|---|---|---|---|---|---|
| | 2 | 1 | $3.2 \pm 0.4$ | $204 \pm 12$ | 1514 |
| | | 2 | $2.9 \pm 0.1$ | $183 \pm 11$ | 106 |
| | 3 | 1 | $3.8 \pm 0.5$ | $212 \pm 15$ | 244 |
| | | 2 | $2.9 \pm 0.2$ | $177 \pm 12$ | 57 |
| M2 | | 3 | $3.1 \pm 0.2$ | $205 \pm 11$ | 1319 |
| | 4 | 1 | $3.1 \pm 0.2$ | $209 \pm 11$ | 1069 |
| | | 2 | $2.9 \pm 0.2$ | $160 \pm 10$ | 14 |
| | | 3 | $4.0 \pm 0.5$ | $211 \pm 14$ | 147 |
| | | 4 | $2.9 \pm 0.1$ | $193 \pm 7$ | 390 |

# List of tables

# List of figures

# Literature

[1]     A. Brand, L. Allen, M. Altman, M. Hlava, J. Scott, Beyond authorship: Attribution, contribution, collaboration, and credit, Learned Publishing. 28 (2015) 151–155. https://doi.org/10.1087/20150211.

[2]     C. Barzak, The Closing Window., 2011. https://muse.jhu.edu/pub/131/article/432525/summary (accessed March 23, 2023).

[3]     B.M. Huang, J.R. Yang, H.W. Yen, C.H. Hsu, C.Y. Huang, H. Mohrbacher, Secondary hardened bainite, Materials Science and Technology (United Kingdom). 30 (2014) 1014–1023. https://doi.org/10.1179/1743284714Y.0000000536.

[4]     H. Bhadeshia, R. Honeycombe, Steels: microstructure and properties, Butterworth-Heinemann, 2017.

[5]     S. Zajac, V. Schwinn, K.H. Tacke, Characterisation and Quantification of Complex Bainitic Microstructures in High and Ultra-High Strength Linepipe Steels, Materials Science Forum. 500–501 (2005) 387–394. https://doi.org/10.4028/www.scientific.net/msf.500-501.387.

[6]     Z.J. Xie, X.P. Ma, C.J. Shang, X.M. Wang, S.V. Subramanian, Nano-sized precipitation and properties of a low carbon niobium micro-alloyed bainitic steel, Materials Science and Engineering: A. 641 (2015) 37–44. https://doi.org/10.1016/j.msea.2015.05.101.

[7]     S. jun Jia, B. Li, Q. you Liu, Y. Ren, S. Zhang, H. Gao, Effects of continuous cooling rate on morphology of granular bainite in pipeline steels, Journal of Iron and Steel Research International. 27 (2020) 681–690. https://doi.org/10.1007/s42243-019-00346-3.

[8]     W.B. Lee, S.G. Hong, C.G. Park, S.H. Park, Carbide precipitation and high-temperature strength of hot-rolled high-strength, low-alloy steels containing Nb and Mo, Metall Mater Trans A Phys Metall Mater Sci. 33 (2002) 1689–1698. https://doi.org/10.1007/s11661-002-0178-2.

[9]     T.N. Baker, Microalloyed steels, Ironmaking & Steelmaking. 43 (2016) 264–307. https://doi.org/10.1179/1743281215Y.0000000063.

[10]    Y. OHMORI, H. OHTANI, T. KUNITAKE, The bainite in low carbon low alloy high strength steels, Tetsu-to-Hagane. 57 (1971) 1690–1705.

[11]    U. Lotter, H.P. Hougardy, Kennzeichnung des Gefüges Bainit/The Characterisation of Bainitic Microstructures, Practical Metallography. 29 (1992) 151–156.

[12]    B.L. Bramfitt, J.G. Speer, A perspective on the morphology of bainite, Metallurgical Transactions A. 21 (1990) 817–829. https://doi.org/10.1007/BF02656565.

[13]     G. Krauss, S.W. Thompson, Ferritic Microstructures in Continuously Cooled Low- and Ultralow-carbon Steels, ISIJ International. 35 (1995) 937–945. https://doi.org/10.2355/isijinternational.35.937.

[14]     Z.G. Yang, H.S. Fang, An overview on bainite formation in steels, Curr Opin Solid State Mater Sci. 9 (2005) 277–286. https://doi.org/10.1016/j.cossms.2006.06.005.

[15]     D. De-Castro, A. Eres-Castellanos, J. Vivas, F.G. Caballero, D. San-Martín, C. Capdevila, Morphological and crystallographic features of granular and lath-like bainite in a low carbon microalloyed steel, Mater Charact. 184 (2022) 111703. https://doi.org/10.1016/j.matchar.2021.111703.

[16]     F.G. Caballero, H. Roelofs, S. Hasler, C. Capdevila, J. Chao, J. Cornide, C. Garcia-Mateo, Influence of bainite morphology on impact toughness of continuously cooled cementite free bainitic steels, Materials Science and Technology. 28 (2012) 95–102. https://doi.org/10.1179/1743284710Y.0000000047.

[17]     K. Radwański, Structural characterization of low-carbon multiphase steels merging advanced research methods with light optical microscopy, Archives of Civil and Mechanical Engineering. 16 (2016) 282–293. https://doi.org/10.1016/j.acme.2015.12.001.

[18]     Y.W. Chen, Y.T. Tsai, P.Y. Tung, S.P. Tsai, C.Y. Chen, S.H. Wang, J.R. Yang, Phase quantification in low carbon Nb-Mo bearing steel by electron backscatter diffraction technique coupled with kernel average misorientation, Mater Charact. 139 (2018) 49–58. https://doi.org/10.1016/j.matchar.2018.01.041.

[19]     X.N. Xu, Y. Tian, Q.B. Ye, R.D.K. Misra, Z.D. Wang, The Significant Impact of the Characteristics of Granular Structure and Granular Bainite on the Mechanisms Contributing to Strength–Ductility Combination, J Mater Eng Perform. 30 (2021) 7479–7487. https://doi.org/10.1007/s11665-021-05887-x.

[20]     E. Keehan, L. Karlsson, H.K.D.H. Bhadeshia, M. Thuvander, Three-dimensional analysis of coalesced bainite using focused ion beam tomography, Mater Charact. 59 (2008) 877–882. https://doi.org/10.1016/j.matchar.2007.07.011.

[21]     E. Keehan, L. Karlsson, H.K.D.H. Bhadeshia, M. Thuvander, Electron backscattering diffraction study of coalesced bainite in high strength steel weld metals, Materials Science and Technology. 24 (2008) 1183–1188. https://doi.org/10.1179/174328407X226572.

[22]     B. JOSEFSSON, H.-O. ANDRÉN, MICROSTRUCTURE OF GRANULAR BAINITE, Le Journal de Physique Colloques. 49 (1988) C6-293-C6-298. https://doi.org/10.1051/jphyscol:1988651.

[23]  H.K.D.H. Bhadeshia, Bainite in steels: theory and practice, CRC Press, 2019.

[24]  T. Araki, I. Kozasu, H. Tankechi, K. Shibata, M. Enomoto, H. Tamehiro, others, Atlas for bainitic microstructures, ISIJ, Tokyo, Japan. 1 (1992).

[25]  L.J. Habraken, M. Economopoulos, Bainitic microstructures in low-carbon alloy steels and their mechanical properties, (1967).

[26]  G. Mao, C. Cayron, X. Mao, R. Cao, R. Logé, J. Chen, Morphological and crystallographic characteristics of α structure in a low-carbon iron–nickel alloy, Crystals (Basel). 8 (2018) 1–11. https://doi.org/10.3390/cryst8120468.

[27]  S.C. Wang, J.R. Yang, Effects of chemical composition, rolling and cooling conditions on the amount of martensite/austenite (M/A) constituent formation in low carbon bainitic steels, Materials Science and Engineering A. 154 (1992) 43–49. https://doi.org/10.1016/0921-5093(92)90361-4.

[28]  A.S. Schneider, C.P. Frick, B.G. Clark, P.A. Gruber, E. Arzt, Influence of orientation on the size effect in bcc pillars with different critical temperatures, Materials Science and Engineering A. 528 (2011) 1540–1547. https://doi.org/10.1016/j.msea.2010.10.073.

[29]  C.P. Frick, B.G. Clark, S. Orso, A.S. Schneider, E. Arzt, Size effect on strength and strain hardening of small-scale [1 1 1] nickel compression pillars, Materials Science and Engineering A. 489 (2008) 319–329. https://doi.org/10.1016/j.msea.2007.12.038.

[30]  J.R. Greer, W.D. Nix, Nanoscale gold pillars strengthened through dislocation starvation, Phys Rev B Condens Matter Mater Phys. 73 (2006) 1–6. https://doi.org/10.1103/PhysRevB.73.245410.

[31]  G. Dehm, B.N. Jaya, R. Raghavan, C. Kirchlechner, Overview on micro- and nanomechanical testing: New insights in interface plasticity and fracture at small length scales, Acta Mater. 142 (2018) 248–282. https://doi.org/10.1016/j.actamat.2017.06.019.

[32]  C. Tian, D. Ponge, L. Christiansen, C. Kirchlechner, On the mechanical heterogeneity in dual phase steel grades: Activation of slip systems and deformation of martensite in DP800, Acta Mater. 183 (2020) 274–284. https://doi.org/10.1016/j.actamat.2019.11.002.

[33]  H. Ghassemi-Armaki, R. Maaß, S.P. Bhat, S. Sriram, J.R. Greer, K.S. Kumar, Deformation response of ferrite and martensite in a dual-phase steel, Acta Mater. 62 (2014) 197–211. https://doi.org/10.1016/J.ACTAMAT.2013.10.001.

[34] J.L. Stewart, L. Jiang, J.J. Williams, N. Chawla, Prediction of bulk tensile behavior of dual phase stainless steels using constituent behavior from micropillar compression experiments, Materials Science and Engineering A. 534 (2012) 220–227. https://doi.org/10.1016/j.msea.2011.11.062.

[35] C.C. Tasan, M. Diehl, D. Yan, M. Bechtold, F. Roters, L. Schemmann, C. Zheng, N. Peranio, D. Ponge, M. Koyama, K. Tsuzaki, D. Raabe, An Overview of Dual-Phase Steels: Advances in Microstructure-Oriented Processing and Micromechanically Guided Design, Annu Rev Mater Res. 45 (2015) 391–431. https://doi.org/10.1146/annurev-matsci-070214-021103.

[36] J.H. Pak, H.K.D.H. Bhadeshia, L. Karlsson, Mechanism of misorientation development within coalesced martensite, Materials Science and Technology (United Kingdom). 28 (2012) 918–923. https://doi.org/10.1179/1743284712Y.0000000023.

[37] Y.W. Chen, B.M. Huang, Y.T. Tsai, S.P. Tsai, C.Y. Chen, J.R. Yang, Microstructural evolutions of low carbon Nb/Mo-containing bainitic steels during high-temperature tempering, Mater Charact. 131 (2017) 298–305. https://doi.org/10.1016/j.matchar.2017.07.022.

[38] S. Keeler, M. Kimchi, Advanced high strength steels Application Guidelines, version 5, world auto steel, World Steel Association, Brussels. (2014).

[39] C.A. Beiser, The effect of small columbium additions to semi killed, medium carbon steels, ASM Preprint. (1959).

[40] W.B. Morrison, Overview of microalloying in steel, Report. (2000) 25–35.

[41] C.M. Enloe, F. D'Aiuto, H. Mohrbacher, Maximizing strengthening mechanisms in continuously annealed HSLA steel, Steel Properties and Applications in Conjunction with Materials Science and Technology 2021. (2021) 49–57. https://doi.org/10.33313/280/007.

[42] A.J. DeArdo, Multi-phase Microstructures and Their Properties in High Strength Low Carbon Steels., ISIJ International. 35 (1995) 946–954. https://doi.org/10.2355/isijinternational.35.946.

[43] C.M. Sellars, J.A. Whiteman, Recrystallization and grain growth'in hot rolling, Metal Science. 13 (1979) 187–194. https://doi.org/10.1179/msc.1979.13.3-4.187.

[44] A. Pandit, A. Murugaiyan, A.S. Podder, A. Haldar, D. Bhattacharjee, S. Chandra, R.K. Ray, Strain induced precipitation of complex carbonitrides in Nb-V and Ti-V microalloyed steels, Scr Mater. 53 (2005) 1309–1314. https://doi.org/10.1016/j.scriptamat.2005.07.003.

[45] S.W. Thompson, D.J. Vin Col, G. Krauss, Continuous cooling transformations and microstructures in a low-carbon, high-strength low-alloy plate steel, Metallurgical Transactions A. 21 (1990) 1493–1507. https://doi.org/10.1007/BF02672564.

[46]   P.C.M. Rodrigues, E.V. Pereloma, D.B. Santos, Mechanical properities of an HSLA bainitic steel subjected to controlled rolling with accelerated cooling, Materials Science and Engineering: A. 283 (2000) 136–143. https://doi.org/10.1016/S0921-5093(99)00795-9.

[47]   J.S. Kang, S.S. Ahn, C.Y. Yoo, C.G. Park, FIB and TEM Studies on the Bainitic Microstructure in Low Carbon HSLA Steels, Adv Mat Res. 26–28 (2007) 73–76. https://doi.org/10.4028/www.scientific.net/amr.26-28.73.

[48]   W.C. Jeong, Microstructural aspects of quasi-polygonal and granular bainitic ferrites in an ultra-low-carbon interstitial-free high-strength steel, Metallurgical and Materials Transactions A. 34 (2003) 2025–2026. https://doi.org/10.1007/s11661-003-0167-0.

[49]   S. Zaefferer, J. Ohlert, W. Bleck, A study of microstructure, transformation mechanisms and correlation between microstructure and mechanical properties of a low alloyed TRIP steel, Acta Mater. 52 (2004) 2765–2778. https://doi.org/10.1016/j.actamat.2004.02.044.

[50]   P. Cizek, The microstructure evolution and softening processes during high-temperature deformation of a 21Cr-10Ni-3Mo duplex stainless steel, Acta Mater. 106 (2016) 129–143. https://doi.org/10.1016/j.actamat.2016.01.012.

[51]   M. Müller, D. Britz, L. Ulrich, T. Staudt, F. Mücklich, Classification of bainitic structures using textural parameters and machine learning techniques, Metals (Basel). 10 (2020) 1–19. https://doi.org/10.3390/met10050630.

[52]   S. ZAEFFERER, P. ROMANO, F. FRIEDEL, EBSD as a tool to identify and quantify bainite and ferrite in low-alloyed Al-TRIP steels, J Microsc. 230 (2008) 499–508. https://doi.org/10.1111/j.1365-2818.2008.02010.x.

[53]   J.F. Nye, Some geometrical relations in dislocated crystals, Acta Metallurgica. 1 (1953) 153–162. https://doi.org/10.1016/0001-6160(53)90054-6.

[54]   R. Petrov, L. Kestens, A. Wasilkowska, Y. Houbaert, Microstructure and texture of a lightly deformed TRIP-assisted steel characterized by means of the EBSD technique, Materials Science and Engineering A. 447 (2007) 285–297. https://doi.org/10.1016/j.msea.2006.10.023.

[55]   B. Hutchinson, L. Ryde, E. Lindh, K. Tagashira, Texture in hot rolled austenite and resulting transformation products, Materials Science and Engineering A. 257 (1998) 9–17. https://doi.org/10.1016/S0921-5093(98)00820-X.

[56]   J. Wu, P.J. Wray, C.I. Garcia, M. Hua, A.J. Deardo, Image quality analysis: A new method of characterizing microstructures, ISIJ International. 45 (2005) 254–262. https://doi.org/10.2355/isijinternational.45.254.

[57] L. Ryde, Application of EBSD to analysis of microstructures in commercial steels, Materials Science and Technology. 22 (2006) 1297–1306. https://doi.org/10.1179/174328406X130948.

[58] G. Cheng, F. Zhang, A. Ruimi, D.P. Field, X. Sun, Quantifying the effects of tempering on individual phase properties of DP980 steel with nanoindentation, Materials Science and Engineering A. 667 (2016) 240–249. https://doi.org/10.1016/j.msea.2016.05.011.

[59] M. Delincé, P.J. Jacques, T. Pardoen, Separation of size-dependent strengthening contributions in fine-grained Dual Phase steels by nanoindentation, Acta Mater. 54 (2006) 3395–3404. https://doi.org/10.1016/j.actamat.2006.03.031.

[60] G. Cheng, K.S. Choi, X. Hu, X. Sun, Determining individual phase properties in a multi-phase Q&P steel using multi-scale indentation tests, Materials Science and Engineering A. 652 (2016) 384–395. https://doi.org/10.1016/j.msea.2015.11.072.

[61] F. Zhang, A. Ruimi, D.P. Field, Phase Identification of Dual-Phase (DP980) Steels by Electron Backscatter Diffraction and Nanoindentation Techniques, Microscopy and Microanalysis. 22 (2016) 99–107. https://doi.org/10.1017/S1431927615015779.

[62] B.-W. Choi, D.-H. Seo, J.-Y. Yoo, J. Jang, Predicting macroscopic plastic flow of high-performance, dual-phase steel through spherical nanoindentation on each microphase, J Mater Res. 24 (2009) 816–822. https://doi.org/10.1557/jmr.2009.0109.

[63] B.-W. Choi, D.-H. Seo, J. Jang, A nanoindentation study on the micromechanical characteristics of API X100 pipeline steel, Metals and Materials International. 15 (2009) 373–378. https://doi.org/10.1007/s12540-009-0373-4.

[64] B. Vignesh, W.C. Oliver, G.S. Kumar, P.S. Phani, Critical assessment of high speed nanoindentation mapping technique and data deconvolution on thermal barrier coatings, Mater Des. 181 (2019) 108084. https://doi.org/10.1016/j.matdes.2019.108084.

[65] J. Kadkhodapour, S. Schmauder, D. Raabe, S. Ziaei-Rad, U. Weber, M. Calcagnotto, Experimental and numerical study on geometrically necessary dislocations and non-homogeneous mechanical properties of the ferrite phase in dual phase steels, Acta Mater. 59 (2011) 4387–4394. https://doi.org/10.1016/j.actamat.2011.03.062.

[66] H. Ghassemi-Armaki, R. Maaß, S.P. Bhat, S. Sriram, J.R. Greer, K.S. Kumar, Deformation response of ferrite and martensite in a dual-phase steel, Acta Mater. 62 (2014) 197–211. https://doi.org/10.1016/j.actamat.2013.10.001.

[67]    B. Yang, H. Vehoff, Dependence of nanohardness upon indentation size and grain size - A local examination of the interaction between dislocations and grain boundaries, Acta Mater. 55 (2007) 849–856. https://doi.org/10.1016/j.actamat.2006.09.004.

[68]    T. Eliash, M. Kazakevich, V.N. Semenov, E. Rabkin, Nanohardness of molybdenum in the vicinity of grain boundaries and triple junctions, Acta Mater. 56 (2008) 5640–5652. https://doi.org/10.1016/j.actamat.2008.07.036.

[69]    W.A. Soer, J.T.M. De Hosson, Detection of grain-boundary resistance to slip transfer using nanoindentation, Mater Lett. 59 (2005) 3192–3195. https://doi.org/10.1016/j.matlet.2005.03.075.

[70]    E. Fereiduni, S.S. Ghasemi Banadkouki, Ferrite hardening response in a low alloy ferrite-martensite dual phase steel, J Alloys Compd. 589 (2014) 288–294. https://doi.org/10.1016/j.jallcom.2013.11.183.

[71]    H. Besharatloo, M. Carpio, J.-M. Cabrera, A.M. Mateo, G. Fargas, J.M. Wheeler, J.J. Roa, L. Llanes, Novel Mechanical Characterization of Austenite and Ferrite Phases within Duplex Stainless Steel, Metals (Basel). 10 (2020) 1352. https://doi.org/10.3390/met10101352.

[72]    J.M. Wheeler, Mechanical phase mapping of the Taza meteorite using correlated high-speed nanoindentation and EDX, J Mater Res. 36 (2021) 94–104. https://doi.org/10.1557/s43578-020-00056-7.

[73]    P. Bholowalia, A. Kumar, EBK-Means: A Clustering Technique based on Elbow Method and K-Means in WSN, Int J Comput Appl. 105 (2014) 975–8887.

[74]    D. Caillard, A TEM in situ study of alloying effects in iron. II - Solid solution hardening caused by high concentrations of Si and Cr, Acta Mater. 61 (2013) 2808–2827. https://doi.org/10.1016/j.actamat.2013.01.049.

[75]    Y. Nakada, A.S. Keh, Solid solution strengthening in Fe-N single crystals, Acta Metallurgica. 16 (1968) 903–914. https://doi.org/10.1016/0001-6160(68)90057-6.

[76]    J.R. Stephens, W.R. Witzke, Alloy softening in binary iron solid solutions, Journal of The Less-Common Metals. 48 (1976) 285–308. https://doi.org/10.1016/0022-5088(76)90009-6.

[77]    T. Gladman, The physical metallurgy of microalloyed steels, Maney Pub, 1997.

[78]    A.H. Cottrell, B.A. Bilby, Dislocation theory of yielding and strain ageing of iron, Proceedings of the Physical Society. Section A. 62 (1949) 49–62. https://doi.org/10.1088/0370-1298/62/1/308.

[79]  Q. Furnémont, M. Kempf, P.J. Jacques, M. Göken, F. Delannay, On the measurement of the nanohardness of the constitutive phases of TRIP-assisted multiphase steels, Materials Science and Engineering A. 328 (2002) 26–32. https://doi.org/10.1016/S0921-5093(01)01689-6.

[80]  T. Gladman, Precipitation hardening in metals, Materials Science and Technology. 15 (1999) 30–36. https://doi.org/10.1179/026708399773002782.

[81]  E.V. Morales, R.A. Silva, I.S. Bott, S. Paciornik, Strengthening mechanisms in a pipeline microalloyed steel with a complex microstructure, Materials Science and Engineering: A. 585 (2013) 253–260. https://doi.org/10.1016/j.msea.2013.07.060.

[82]  J.G. Speer, J.R. Michael, S.S. Hansen, Carbonitride precipitation in niobium/vanadium microalloyed steels, Metallurgical Transactions A. 18 (1987) 211–222. https://doi.org/10.1007/BF02646155.

[83]  D. Hull, D.J. Bacon, Introduction to dislocations, Elsevier, 2011.

[84]  G.I. Taylor, The mechanism of plastic deformation of crystals. Part I.—Theoretical, Proceedings of the Royal Society of London. Series A, Containing Papers of a Mathematical and Physical Character. 145 (1934) 362–387.

[85]  S.H. He, B.B. He, K.Y. Zhu, M.X. Huang, On the correlation among dislocation density, lath thickness and yield stress of bainite, Acta Mater. 135 (2017) 382–389. https://doi.org/10.1016/j.actamat.2017.06.050.

[86]  E.O. Hall, The Deformation and Ageing of Mild Steel: III Discussion of Results, Proceedings of the Physical Society. Section B. 64 (1951) 747–753. https://doi.org/10.1088/0370-1301/64/9/303.

[87]  N.J. Petch, The cleavage strength of polycrystals, Journal of the Iron and Steel Institute. 174 (1953) 25–28.

[88]  K. Zhu, O. Bouaziz, C. Oberbillig, M. Huang, An approach to define the effective lath size controlling yield strength of bainite, Materials Science and Engineering A. 527 (2010) 6614–6619. https://doi.org/10.1016/j.msea.2010.06.061.

[89]  H. sheng FANG, C. FENG, Y. kang ZHENG, Z. gang YANG, B. zhe BAI, Creation of Air-Cooled Mn Series Bainitic Steels, Journal of Iron and Steel Research International. 15 (2008) 1–9. https://doi.org/10.1016/S1006-706X(08)60257-5.

[90]  W. Cai, W.D. Nix, Imperfections in crystalline solids, Cambridge University Press, 2016.

[91]  G. Gottstein, Physical foundations of materials science, Springer, 2004.

[92]  M.N. Shetty, Dislocations and mechanical behaviour of materials, PHI Learning Pvt. Ltd., 2013.

[93]  E. Schmid, W. Boas, Plasticity of crystals, (1950).

[94]  O. Torrents Abad, J.M. Wheeler, J. Michler, A.S. Schneider, E. Arzt, Temperature-dependent size effects on the strength of Ta and W micropillars, Acta Mater. 103 (2016) 483–494. https://doi.org/10.1016/j.actamat.2015.10.016.

[95]  I. Ryu, W.D. Nix, W. Cai, Plasticity of bcc micropillars controlled by competition between dislocation multiplication and depletion, Acta Mater. 61 (2013) 3233–3241. https://doi.org/10.1016/j.actamat.2013.02.011.

[96]  C.R. Weinberger, B.L. Boyce, C.C. Battaile, Slip planes in bcc transition metals, International Materials Reviews. 58 (2013) 296–314. https://doi.org/10.1179/1743280412Y.0000000015.

[97]  D. Veselý, The Study of Deformation of Thin Foils of Mo under the Electron Microscope, Physica Status Solidi (B). 29 (1968) 675–683. https://doi.org/10.1002/pssb.19680290217.

[98]  S. Naka, A. Lasalmonie, P. Costa, L.P. Kubin, L.P. Kubin, The low-temperature plastic deformation of α-titanium and the core structure of a-type screw dislocations, Philosophical Magazine A: Physics of Condensed Matter, Structure, Defects and Mechanical Properties. 57 (1988) 717–740. https://doi.org/10.1080/01418618808209916.

[99]  D. Veselý, The Study of Slip Bands on the Surface of Mo Single Crystals, Physica Status Solidi (B). 29 (1968) 685–696. https://doi.org/10.1002/pssb.19680290218.

[100] C. Domain, G. Monnet, Simulation of screw dislocation motion in tron by molecular dynamics simulations, Phys Rev Lett. 95 (2005) 16–19. https://doi.org/10.1103/PhysRevLett.95.215506.

[101] J.R. Greer, C.R. Weinberger, W. Cai, Comparing the strength of f.c.c. and b.c.c. sub-micrometer pillars: Compression experiments and dislocation dynamics simulations, Materials Science and Engineering A. 493 (2008) 21–25. https://doi.org/10.1016/j.msea.2007.08.093.

[102] M.R. Gilbert, S. Queyreau, J. Marian, Stress and temperature dependence of screw dislocation mobility in α-Fe by molecular dynamics, Phys Rev B Condens Matter Mater Phys. 84 (2011) 1–11. https://doi.org/10.1103/PhysRevB.84.174103.

[103] W. Cai, V. V. Bulatov, J. Chang, J. Li, S. Yip, Chapter 64 Dislocation core effects on mobility, 2004. https://doi.org/10.1016/S1572-4859(05)80003-8.

[104] A. Kraych, P. Carrez, P. Cordier, On dislocation glide in MgSiO3 bridgmanite at high-pressure and high-temperature, Earth Planet Sci Lett. 452 (2016) 60–68. https://doi.org/10.1016/j.epsl.2016.07.035.

[105] R. Peierls, The size of a dislocation, Proceedings of the Physical Society. 52 (1940) 34–37. https://doi.org/10.1088/0959-5309/52/1/305.

[106] F.R.N. Nabarro, Dislocations in a simple cubic lattice, Proceedings of the Physical Society. 59 (1947) 256–272. https://doi.org/10.1088/0959-5309/59/2/309.

[107] A. Seeger, Peierls barriers, kinks, and flow stress: Recent progress, Zeitschrift Fuer Metallkunde/Materials Research and Advanced Techniques. 93 (2002) 760–777. https://doi.org/10.3139/146.020760.

[108] A. Seeger, The temperature and strain-rate dependence of the flow stress of body-centred cubic metals: a theory based on kink-kink interactions, International Journal of Materials Research. 72 (1981) 369–380.

[109] M.D. Uchic, D.M. Dimiduk, J.N. Florando, Sample Dimensions Influence Strength and Crystal Plasticity, 305 (2004) 986–989.

[110] G.M. Pharr, E.G. Herbert, Y. Gao, The Indentation Size Effect: A Critical Examination of Experimental Observations and Mechanistic Interpretations, Annu Rev Mater Res. 40 (2010) 271–292. https://doi.org/10.1146/annurev-matsci-070909-104456.

[111] W.D. Nix, H. Gao, Indentation size effects in crystalline materials: A law for strain gradient plasticity, J Mech Phys Solids. 46 (1998) 411–425. https://doi.org/10.1016/S0022-5096(97)00086-0.

[112] K. Durst, B. Backes, M. Göken, Indentation size effect in metallic materials: Correcting for the size of the plastic zone, Scr Mater. 52 (2005) 1093–1097. https://doi.org/10.1016/j.scriptamat.2005.02.009.

[113] N. V. Malyar, H. Springer, J. Wichert, G. Dehm, C. Kirchlechner, Synthesis and mechanical testing of grain boundaries at the micro and sub-micro scale, Materialpruefung/Materials Testing. 61 (2019) 5–18. https://doi.org/10.3139/120.111286.

[114] D. Kiener, C. Motz, M. Rester, M. Jenko, G. Dehm, FIB damage of Cu and possible consequences for miniaturized mechanical tests, Materials Science and Engineering A. 459 (2007) 262–272. https://doi.org/10.1016/j.msea.2007.01.046.

[115] D. Kiener, C. Motz, G. Dehm, Micro-compression testing: A critical discussion of experimental constraints, Materials Science and Engineering A. 505 (2009) 79–87. https://doi.org/10.1016/j.msea.2009.01.005.

[116] C.A. Volkert, E.T. Lilleodden, Size effects in the deformation of sub-micron Au columns, Philosophical Magazine. 86 (2006) 5567–5579. https://doi.org/10.1080/14786430600567739.

[117]  O. Kraft, P.A. Gruber, R. Mönig, D. Weygand, Plasticity in confined dimensions, Annu Rev Mater Res. 40 (2010) 293–317. https://doi.org/10.1146/annurev-matsci-082908-145409.

[118]  A.S. Schneider, B.G. Clark, C.P. Frick, E. Arzt, Correlation between activation volume and pillar diameter for Mo and Nb BCC pillars, Materials Research Society Symposium Proceedings. 1185 (2009) 75–79. https://doi.org/10.1557/proc-1185-ii07-04.

[119]  G. Richter, K. Hillerich, D.S. Gianola, R. Mönig, O. Kraft, C.A. Volkert, Ultrahigh strength single crystalline nanowhiskers grown by physical vapor deposition, Nano Lett. 9 (2009) 3048–3052. https://doi.org/10.1021/nl9015107.

[120]  S. Brinckmann, J.Y. Kim, J.R. Greer, Fundamental differences in mechanical behavior between two types of crystals at the nanoscale, Phys Rev Lett. 100 (2008). https://doi.org/10.1103/PhysRevLett.100.155502.

[121]  A.S. Schneider, B.G. Clark, C.P. Frick, P.A. Gruber, E. Arzt, Effect of orientation and loading rate on compression behavior of small-scale Mo pillars, Materials Science and Engineering A. 508 (2009) 241–246. https://doi.org/10.1016/j.msea.2009.01.011.

[122]  R.M. Jentner, S.-P. Tsai, A. Welle, K. Srivastava, S. Scholl, J.P. Best, C. Kirchlechner, G. Dehm, Automated Classification of Granular Bainite and Polygonal Ferrite by Electron Backscatter Diffraction Verified through Local Structural and Mechanical Analyses, SSRN Electronic Journal. (2023). https://doi.org/10.2139/ssrn.4324505.

[123]  W.C. Oliver, G.M. Pharr, An improved technique for determining hardness and elastic modulus using load and displacement sensing indentation experiments, J Mater Res. 7 (1992) 1564–1583. https://doi.org/10.1557/JMR.1992.1564.

[124]  D.J. Ketchen, C.L. Shook, The application of cluster analysis in strategic management research: An analysis and critique, Strategic Management Journal. 17 (1996) 441–458. https://doi.org/10.1002/(sici)1097-0266(199606)17:6<441::aid-smj819>3.0.co;2-g.

[125]  F. Liu, Y. Deng, Determine the Number of Unknown Targets in Open World Based on Elbow Method, IEEE Transactions on Fuzzy Systems. 29 (2021) 986–995. https://doi.org/10.1109/TFUZZ.2020.2966182.

[126]  C. Goutte, P. Toft, E. Rostrup, F.Å. Nielsen, L.K. Hansen, On clustering fMRI time series, Neuroimage. 9 (1999) 298–310. https://doi.org/10.1006/nimg.1998.0391.

[127]  M.A. Syakur, B.K. Khotimah, E.M.S. Rochman, B.D. Satoto, Integration K-Means Clustering Method and Elbow Method For Identification of The Best Customer Profile Cluster, IOP Conf Ser Mater Sci Eng. 336 (2018) 012017. https://doi.org/10.1088/1757-899X/336/1/012017.

[128] J. MacQueen, others, Some methods for classification and analysis of multivariate observations, in: Proceedings of the Fifth Berkeley Symposium on Mathematical Statistics and Probability, 1967: pp. 281–297.

[129] J.A. Hartigan, M.A. Wong, Algorithm AS 136: A K-Means Clustering Algorithm, Appl Stat. 28 (1979) 100. https://doi.org/10.2307/2346830.

[130] F. Bachmann, R. Hielscher, H. Schaeben, Texture Analysis with MTEX – Free and Open Source Software Toolbox, Solid State Phenomena. 160 (2010) 63–68. https://doi.org/10.4028/www.scientific.net/SSP.160.63.

[131] J.R. Greer, W.C. Oliver, W.D. Nix, Size dependence of mechanical properties of gold at the micron scale in the absence of strain gradients, Acta Mater. 53 (2005) 1821–1830. https://doi.org/10.1016/j.actamat.2004.12.031.

[132] R. Hosseinabadi, H. Riesch-Oppermann, J.P. Best, G. Dehm, C. Kirchlechner, Size scaling in bi-crystalline Cu micropillars containing a coherent twin boundary, Acta Mater. 230 (2022) 117841. https://doi.org/10.1016/j.actamat.2022.117841.

[133] A.C. Fischer-Cripps, Critical review of analysis and interpretation of nanoindentation test data, Surf Coat Technol. 200 (2006) 4153–4165. https://doi.org/10.1016/j.surfcoat.2005.03.018.

[134] G. Constantinides, F.J. Ulm, K. Van Vliet, On the use of nanoindentation for cementitious materials, Materials and Structures/Materiaux et Constructions. 36 (2003) 191–196. https://doi.org/10.1617/14020.

[135] G. Constantinides, K.S. Ravi Chandran, F.J. Ulm, K.J. Van Vliet, Grid indentation analysis of composite microstructure and mechanics: Principles and validation, Materials Science and Engineering A. 430 (2006) 189–202. https://doi.org/10.1016/j.msea.2006.05.125.

[136] N.X. Randall, M. Vandamme, F.J. Ulm, Nanoindentation analysis as a two-dimensional tool for mapping the mechanical properties of complex surfaces, J Mater Res. 24 (2009) 679–690. https://doi.org/10.1557/jmr.2009.0149.

[137] F.-J. Ulm, M. Vandamme, C. Bobko, J. Alberto Ortega, K. Tai, C. Ortiz, Statistical Indentation Techniques for Hydrated Nanocomposites: Concrete, Bone, and Shale, Journal of the American Ceramic Society. 90 (2007) 2677–2692. https://doi.org/10.1111/j.1551-2916.2007.02012.x.

[138] Y.B. Veytskin, V.K. Tammina, C.P. Bobko, P.G. Hartley, M.B. Clennell, D.N. Dewhurst, R.R. Dagastine, Micromechanical characterization of shales through nanoindentation and energy dispersive x-ray spectrometry, Geomechanics for Energy and the Environment. 9 (2017) 21–35. https://doi.org/10.1016/j.gete.2016.10.004.

[139] S. Janakiram, P.S. Phani, G. Ummethala, S.K. Malladi, J. Gautam, L.A.I. Kestens, New insights on recovery and early recrystallization of ferrite-pearlite banded cold rolled high strength steels by high speed nanoindentation mapping, Scr Mater. 194 (2021) 113676. https://doi.org/10.1016/j.scriptamat.2020.113676.

[140] D. Marutho, S. Hendra Handaka, E. Wijaya, Muljono, The Determination of Cluster Number at k-Mean Using Elbow Method and Purity Evaluation on Headline News, in: 2018 International Seminar on Application for Technology of Information and Communication, IEEE, 2018: pp. 533–538. https://doi.org/10.1109/ISEMANTIC.2018.8549751.

[141] E. Koumoulos, G. Konstantopoulos, C. Charitidis, Applying machine learning to nanoindentation data of (nano-) enhanced composites, Fibers. 8 (2020) 1–13. https://doi.org/10.3390/fib8010003.

[142] M. Sarwar, R. Priestner, Influence of ferrite-martensite microstructural morphology on tensile properties of dual-phase steel, J Mater Sci. 31 (1996) 2091–2095. https://doi.org/10.1007/BF00356631.

[143] A.-P. Pierman, O. Bouaziz, T. Pardoen, P.J. Jacques, L. Brassart, The influence of microstructure and composition on the plastic behaviour of dual-phase steels, Acta Mater. 73 (2014) 298–311. https://doi.org/10.1016/j.actamat.2014.04.015.

[144] N. Ishikawa, K. Yasuda, H. Sueyoshi, S. Endo, H. Ikeda, T. Morikawa, K. Higashida, Microscopic deformation and strain hardening analysis of ferrite–bainite dual-phase steels using micro-grid method, Acta Mater. 97 (2015) 257–268. https://doi.org/10.1016/j.actamat.2015.06.037.

[145] M.D. Taylor, K.S. Choi, X. Sun, D.K. Matlock, C.E. Packard, L. Xu, F. Barlat, Correlations between nanoindentation hardness and macroscopic mechanical properties in DP980 steels, Materials Science and Engineering A. 597 (2014) 431–439. https://doi.org/10.1016/j.msea.2013.12.084.

[146] T. Ohmura, K. Tsuzaki, Plasticity initiation and subsequent deformation behavior in the vicinity of single grain boundary investigated through nanoindentation technique, J Mater Sci. 42 (2007) 1728–1732. https://doi.org/10.1007/s10853-006-0885-y.

[147] B.B. He, K. Zhu, M.X. Huang, On the nanoindentation behaviour of complex ferritic phases, Philos Mag Lett. 94 (2014) 439–446. https://doi.org/10.1080/09500839.2014.921348.

[148] W.A. Soer, K.E. Aifantis, J.T.M. De Hosson, Incipient plasticity during nanoindentation at grain boundaries in body-centered cubic metals, Acta Mater. 53 (2005) 4665–4676. https://doi.org/10.1016/j.actamat.2005.07.001.

[149] T.B. Britton, D. Randman, A.J. Wilkinson, Nanoindentation study of slip transfer phenomenon at grain boundaries, J Mater Res. 24 (2009) 607–615. https://doi.org/10.1557/jmr.2009.0088.

[150] J. Moon, S. Kim, J. il Jang, J. Lee, C. Lee, Orowan strengthening effect on the nanoindentation hardness of the ferrite matrix in microalloyed steels, Materials Science and Engineering A. 487 (2008) 552–557. https://doi.org/10.1016/j.msea.2007.10.046.

[151] H. Zhu, L.A. Tessaroto, R. Sabia, V.A. Greenhut, M. Smith, D.E. Niesz, Chemical mechanical polishing (CMP) anisotropy in sapphire, Appl Surf Sci. 236 (2004) 120–130. https://doi.org/10.1016/j.apsusc.2004.04.027.

[152] S. Zaefferer, N.N. Elhami, Theory and application of electron channelling contrast imaging under controlled diffraction conditions, Acta Mater. 75 (2014) 20–50. https://doi.org/10.1016/j.actamat.2014.04.018.

[153] T.Y. Tsui, W.C. Oliver, G.M. Pharr, Influences of stress on the measurement of mechanical properties using nanoindentation: Part I. Experimental studies in an aluminum alloy, J Mater Res. 11 (1996) 752–759. https://doi.org/10.1557/JMR.1996.0091.

[154] A. Bolshakov, W.C. Oliver, G.M. Pharr, Influences of stress on the measurement of mechanical properties using nanoindentation: Part II. Finite element simulations, J Mater Res. 11 (1996) 760–768. https://doi.org/10.1557/JMR.1996.0092.

[155] J.J. Vlassak, W.D. Nix, Measuring the elastic properties of anisotropic materials by means of indentation experiments, J Mech Phys Solids. 42 (1994) 1223–1245. https://doi.org/10.1016/0022-5096(94)90033-7.

[156] A.C. Fischer-Cripps, Nanoindentation, Springer New York, New York, NY, 2011. https://doi.org/10.1007/978-1-4419-9872-9.

[157] K.W. McElhaney, J.J. Vlassak, W.D. Nix, Determination of indenter tip geometry and indentation contact area for depth-sensing indentation experiments, J Mater Res. 13 (1998) 1300–1306. https://doi.org/10.1557/JMR.1998.0185.

[158] E.D. Hintsala, U. Hangen, D.D. Stauffer, High-Throughput Nanoindentation for Statistical and Spatial Property Determination, Jom. 70 (2018) 494–503. https://doi.org/10.1007/s11837-018-2752-0.

[159] B.X. Wang, X.H. Liu, G.D. Wang, Correlation of microstructures and low temperature toughness in low carbon Mn–Mo–Nb pipeline steel, Materials Science and Technology. 29 (2013) 1522–1528. https://doi.org/10.1179/1743284713Y.0000000326.

[160] C.N. Hulme-Smith, I. Lonardelli, M.J. Peet, A.C. Dippel, H.K.D.H. Bhadeshia, Enhanced thermal stability in nanostructured bainitic steel, Scr Mater. 69 (2013) 191–194. https://doi.org/10.1016/j.scriptamat.2013.03.029.

[161] R.Y. Zhang, J.D. Boyd, Bainite transformation in deformed austenite, Metall Mater Trans A Phys Metall Mater Sci. 41 (2010) 1448–1459. https://doi.org/10.1007/s11661-010-0190-x.

[162] M.C. Zhao, K. Yang, F.R. Xiao, Y.Y. Shan, Continuous cooling transformation of undeformed and deformed low carbon pipeline steels, Materials Science and Engineering A. 355 (2003) 126–136. https://doi.org/10.1016/S0921-5093(03)00074-1.

[163] H.J. Jun, J.S. Kang, D.H. Seo, K.B. Kang, C.G. Park, Effects of deformation and boron on microstructure and continuous cooling transformation in low carbon HSLA steels, Materials Science and Engineering A. 422 (2006) 157–162. https://doi.org/10.1016/j.msea.2005.05.008.

[164] S.I. Wright, M.M. Nowell, D.P. Field, A review of strain analysis using electron backscatter diffraction, Microscopy and Microanalysis. 17 (2011) 316–329. https://doi.org/10.1017/S1431927611000055.

[165] R.M. Jentner, K. Srivastava, S. Scholl, F.J. Gallardo-Basile, J.P. Best, C. Kirchlechner, G. Dehm, Unsupervised clustering of nanoindentation data for microstructural reconstruction: Challenges in phase discrimination, Materialia (Oxf). 28 (2023) 101750. https://doi.org/10.1016/j.mtla.2023.101750.

[166] T. Yamashita, Y. Tanaka, M. Nagoshi, K. Ishida, Novel technique to suppress hydrocarbon contamination for high accuracy determination of carbon content in steel by FE-EPMA, Sci Rep. 6 (2016) 29825. https://doi.org/10.1038/srep29825.

[167] P.T. Pinard, A. Schwedt, A. Ramazani, U. Prahl, S. Richter, Characterization of Dual-Phase Steel Microstructure by Combined Submicrometer EBSD and EPMA Carbon Measurements, Microscopy and Microanalysis. 19 (2013) 996–1006. https://doi.org/10.1017/S1431927613001554.

[168] S. Eswara, A. Pshenova, E. Lentzen, G. Nogay, M. Lehmann, A. Ingenito, Q. Jeangros, F.-J. Haug, N. Valle, P. Philipp, A. Hessler-Wyser, T. Wirtz, A method for quantitative nanoscale imaging of dopant distributions using secondary ion mass spectrometry: an application example in silicon photovoltaics, MRS Commun. 9 (2019) 916–923. https://doi.org/10.1557/mrc.2019.89.

[169] M. Kubicek, G. Holzlechner, A.K. Opitz, S. Larisegger, H. Hutter, J. Fleig, A novel ToF-SIMS operation mode for sub 100nm lateral resolution: Application and performance, Appl Surf Sci. 289 (2014) 407–416. https://doi.org/10.1016/j.apsusc.2013.10.177.

[170] B. Eghbali, A. Abdollah-Zadeh, H. Beladi, P.D. Hodgson, Characterization on ferrite microstructure evolution during large strain warm torsion testing of plain low carbon steel, Materials Science and Engineering A. 435–436 (2006) 499–503. https://doi.org/10.1016/j.msea.2006.07.026.

[171] T. Furuhara, H. Kawata, S. Morito, T. Maki, Crystallography of upper bainite in Fe-Ni-C alloys, Materials Science and Engineering A. 431 (2006) 228–236. https://doi.org/10.1016/j.msea.2006.06.032.

[172] S. MORITO, H. SAITO, T. OGAWA, T. FURUHARA, T. MAKI, Effect of Austenite Grain Size on the Morphology and Crystallography of Lath Martensite in Low Carbon Steels, ISIJ International. 45 (2005) 91–94. https://doi.org/10.2355/isijinternational.45.91.

[173] J.M. Reichert, W.J. Poole, M. Militzer, L. Collins, A New Approach Using Ebsd To Quantitatively Distinguish Complex, Ipc 2014. (2014) 1–7.

[174] H. Terasaki, Y.I. Komizo, Morphology and crystallography of bainite transformation in a single prior-austenite grain of low-carbon steel, Metall Mater Trans A Phys Metall Mater Sci. 44 (2013) 2683–2689. https://doi.org/10.1007/s11661-013-1610-5.

[175] S.K. Mishra, P. Pant, K. Narasimhan, A.D. Rollett, I. Samajdar, On the widths of orientation gradient zones adjacent to grain boundaries, Scr Mater. 61 (2009) 273–276. https://doi.org/10.1016/j.scriptamat.2009.03.062.

[176] C. Perrin, S. Berbenni, H. Vehoff, M. Berveiller, Role of discrete intragranular slip on lattice rotations in polycrystalline Ni: Experimental and micromechanical studies, Acta Mater. 58 (2010) 4639–4649. https://doi.org/10.1016/j.actamat.2010.04.033.

[177] A.D. Rollett, F. Wagner, N. Allain-Bonasso, D.P. Field, R.A. Lebensohn, Comparison of Gradients in Orientation and Stress between Experiment and Simulation, Materials Science Forum. 702–703 (2011) 463–468. https://doi.org/10.4028/www.scientific.net/MSF.702-703.463.

[178] S.I. Wright, M.M. Nowell, R. De Kloe, L. Chan, Orientation precision of electron backscatter diffraction measurements near grain boundaries, Microscopy and Microanalysis. 20 (2014) 852–863. https://doi.org/10.1017/S143192761400035X.

[179] H. Ghassemi-Armaki, P. Chen, S. Bhat, S. Sadagopan, S. Kumar, A. Bower, Microscale-calibrated modeling of the deformation response of low-carbon martensite, Acta Mater. 61 (2013) 3640–3652. https://doi.org/10.1016/j.actamat.2013.02.051.

[180] F. Roters, M. Diehl, P. Shanthraj, P. Eisenlohr, C. Reuber, S.L. Wong, T. Maiti, A. Ebrahimi, T. Hochrainer, H.O. Fabritius, S. Nikolov, M. Friák, N. Fujita, N. Grilli, K.G.F. Janssens, N. Jia, P.J.J. Kok, D. Ma, F. Meier, E. Werner, M. Stricker, D. Weygand, D. Raabe, DAMASK – The Düsseldorf Advanced Material Simulation Kit for modeling multi-physics crystal plasticity, thermal, and damage phenomena from the single crystal up to the component scale, Comput Mater Sci. 158 (2019) 420–478. https://doi.org/10.1016/j.commatsci.2018.04.030.

[181] M. Pozuelo, J.W. Stremfel, J.M. Yang, J. Marian, Strengthening to softening transition in lath martensite, Materialia (Oxf). 5 (2019) 100254. https://doi.org/10.1016/j.mtla.2019.100254.

[182] S. Morito, H. Tanaka, R. Konishi, T. Furuhara, T. Maki, The morphology and crystallography of lath martensite in Fe-C alloys, Acta Mater. 51 (2003) 1789–1799. https://doi.org/10.1016/S1359-6454(02)00577-3.

[183] P. Chen, H. Ghassemi-Armaki, S. Kumar, A. Bower, S. Bhat, S. Sadagopan, Microscale-calibrated modeling of the deformation response of dual-phase steels, Acta Mater. 65 (2014) 133–149. https://doi.org/10.1016/j.actamat.2013.11.036.

[184] N. Kamikawa, K. Sato, G. Miyamoto, M. Murayama, N. Sekido, K. Tsuzaki, T. Furuhara, Stress-strain behavior of ferrite and bainite with nano-precipitation in low carbon steels, Acta Mater. 83 (2015) 383–396. https://doi.org/10.1016/j.actamat.2014.10.010.

[185] P. Xu, B. Bai, F. Yin, H. Fang, K. Nagai, Microstructure control and wear resistance of grain boundary allotriomorphic ferrite/granular bainite duplex steel, Materials Science and Engineering A. 385 (2004) 65–73. https://doi.org/10.1016/j.msea.2004.04.073.

[186] E. Breitbarth, S. Zaefferer, F. Archie, M. Besel, D. Raabe, G. Requena, Evolution of dislocation patterns inside the plastic zone introduced by fatigue in an aged aluminium alloy AA2024-T3, Materials Science and Engineering A. 718 (2018) 345–349. https://doi.org/10.1016/j.msea.2018.01.068.

[187] J.R. Yang, C.Y. Huang, S.C. Wang, The development of ultra-low-carbon bainitic steels, Mater Des. 13 (1992) 335–338. https://doi.org/10.1016/0261-3069(92)90003-Z.

[188] S.C. Wang, R.I. Hsieh, H.Y. Liou, J.R. Yang, The effects of rolling processes on the microstructure and mechanical properties of ultralow carbon bainitic steels, Materials Science and Engineering A. 157 (1992) 29–36. https://doi.org/10.1016/0921-5093(92)90095-I.

[189] K.S. Ng, A.H.W. Ngan, Breakdown of Schmid's law in micropillars, Scr Mater. 59 (2008) 796–799. https://doi.org/10.1016/j.scriptamat.2008.06.019.

[190] G.I. Taylor, Plastic strain in metals, J. Inst. Metals. 62 (1938) 307–324.

[191]   A. Sarkar, S. Sanyal, T.K. Bandyopadhyay, S. Mandal, Implications of microstructure, Taylor factor distribution and texture on tensile properties in a Ti-added Fe-Mn-Al-Si-C steel, Materials Science and Engineering: A. 767 (2019) 138402. https://doi.org/10.1016/j.msea.2019.138402.

[192]   J.M. Rosenberg, H.R. Piehler, Calculation of the taylor factor and lattice rotations for bcc metals deforming by pencil glide, Metallurgical Transactions. 2 (1971) 257–259. https://doi.org/10.1007/BF02662666.

[193]   B. Yang, C. Motz, M. Rester, G. Dehm, Yield stress influenced by the ratio of wire diameter to grain size - A competition between the effects of specimen microstructure and dimension in micro-sized polycrystalline copper wires, Philosophical Magazine. 92 (2012) 3243–3256. https://doi.org/10.1080/14786435.2012.693215.

[194]   H. Zhao, E.J. Palmiere, Influence of cooling rate on the grain-refining effect of austenite deformation in a HSLA steel, Mater Charact. 158 (2019). https://doi.org/10.1016/j.matchar.2019.109990.

[195]   H. Zhao, B.P. Wynne, E.J. Palmiere, Effect of austenite grain size on the bainitic ferrite morphology and grain refinement of a pipeline steel after continuous cooling, Mater Charact. 123 (2017) 128–136. https://doi.org/10.1016/j.matchar.2016.11.025.

[196]   M.K. Graf, H.-G. Hillenbrand, P. Peters, Accelerated cooling of plate for high-strength large-diameter pipe, The Metallurgical Society/AIME,. (1986) 165–179.

[197]   E. Orowan, Problems of plastic gliding, Proceedings of the Physical Society. 52 (1940) 8–22. https://doi.org/10.1088/0959-5309/52/1/303.

[198]   D. Caillard, Kinetics of dislocations in pure Fe. Part I. In situ straining experiments at room temperature, Acta Mater. 58 (2010) 3493–3503. https://doi.org/10.1016/j.actamat.2010.02.023.

[199]   D. Caillard, Kinetics of dislocations in pure Fe. Part II. In situ straining experiments at low temperature, Acta Mater. 58 (2010) 3504–3515. https://doi.org/10.1016/j.actamat.2010.02.024.

[200]   R. Gröger, V. Vitek, Breakdown of the schmid law in bcc molybdenum related to the effect of shear stress perpendicular to the slip direction, Materials Science Forum. 482 (2005) 123–126. https://doi.org/10.4028/0-87849-964-4.123.

# Curriculum vitae

## Personal data

| | |
|---|---|
| Name | Robin Marc Jentner |
| Date of birth | 04.10.1990 |
| Place of birth | Wittlich, Germany |
| Nationality | German |

## Education

| | |
|---|---|
| 10/2016 – 12/2018 | Master of Science Universität des Saarlandes, Germany und Luleå University of Technology, Sweden |
| 09/2013 – 09/2016 | Bachelor of Engineering, Ernst-Abbe Hochschule Jena im Bereich Werkstofftechnik, Germany |
| 08/2010 – 05/2013 | Apprenticeship as Material Tester, AG der Dillinger Hüttenwerke |
| 08/2007 – 06/2009 | Fachoberschule Technik |

## Research Activity

| | |
|---|---|
| 2019 – 2023 | PhD thesis "Phase identification and micromechanical characterization of an advanced high strength low alloy steel", Prof. Dehm, Prof. Kirchlechner, Max-Planck-Institut für Eisenforschung in Düsseldorf, Germany |
| 2018 | Master thesis, "Charakterisierung des Einflusses einer Vorverformung auf das Entfestigungsverhalten eines mikrolegierten HSLA Stahls", Prof. Motz, Prof. Mücklich, Universität des Saarlandes, Germany, |

| | |
|---|---|
| 2017 | Student project, "Hot ductility loss determination of a HSLA during continuous casting process", Dr. Pineda Huitron, Dr. Vuorinen, Luleå University of Technology, Sweden |
| 2016 | Bachelor thesis, "Gefügecharakterisierung an hochfesten Stählen", Prof. Kunert, Ernst-Abbe Hochschule Jena, Germany |
| 11/2014 – 12/2015 | Research assistant, Scanning Electron Microscopy Laboratory, Ernst-Abbe Hochschule Jena, Germany |

## Publications

| | |
|---|---|
| 2023 | R.M. Jentner, S. Scholl, K. Srivastava, J.P. Best, C. Kirchlechner, G. Dehm, Local Strength of Bainitic and Ferritic HSLA Steel Constituents Understood Using Correlative Electron Microscopy and Micro-compression Testing, SSRN Electronic Journal. (2023). https://doi.org/10.2139/ssrn.4408322. |
| 2023 | R.M. Jentner, S.-P. Tsai, A. Welle, K. Srivastava, S. Scholl, J.P. Best, C. Kirchlechner, G. Dehm, Automated Classification of Granular Bainite and Polygonal Ferrite by Electron Backscatter Diffraction Verified through Local Structural and Mechanical Analyses, SSRN Electron. J. (2023). https://doi.org/10.2139/ssrn.4324505. |
| 2023 | R.M. Jentner, K. Srivastava, S. Scholl, F.J. Gallardo-Basile, J.P. Best, C. Kirchlechner, G. Dehm, Unsupervised clustering of nanoindentation data for microstructural reconstruction: Challenges in phase discrimination, Materialia (Oxf). 28 (2023) 101750. https://doi.org/10.1016/j.mtla.2023.101750. |
| | F.-J. Gallardo-Basile, F. Roters, R.M. Jentner, K. Srivastava, S. Scholl, M. Diehl, Modeling Bainite Dual-Phase Steels: A High-Resolution Crystal Plasticity Simulation Study, Crystals (Basel). 13 (2023) 673. https://doi.org/10.3390/cryst13040673. |
| 2020 | R.M. Pineda Huitron, P.E. Ramirez Lopez, E. Vuorinen, R. Jentner, M.E. Kärkkäinen, Converging criteria to characterize crack susceptibility in a |

micro-alloyed steel during continuous casting, Mater. Sci. Eng. A. 772 (2020). https://doi.org/10.1016/j.msea.2019.138691.